Title
Illuminating the background : topics in cosmic microwave background polarization research

Author
Miller, Nathan James

Publication Date
2012

UNIVERSITY OF CALIFORNIA, SAN DIEGO

Illuminating the Background: Topics in Cosmic Microwave Background Polarization Research

A dissertation submitted in partial satisfaction of the
requirements for the degree
Doctor of Philosophy

in

Physics

by

Nathan J. Miller

Committee in charge:

Professor Brian Keating, Chair
Professor Samuel Buss
Professor George Fuller
Professor Hans Paar
Professor Mark Thiemens

2012

The dissertation of Nathan J. Miller is approved, and it is acceptable in quality and form for publication on microfilm and electronically:

Chair

University of California, San Diego

2012

TABLE OF CONTENTS

LIST OF FIGURES

LIST OF TABLES

ACKNOWLEDGEMENTS

There are many people I want to thank during my time in graduate school. First, I want to thank my advisor, Brian Keating, for allowing me to join his research group and work with him as graduate student. I also want to thank all the people who have helped me learn about cosmology and the cosmic microwave background. This includes Meir Shimon, for being a mentor from whom I learned a lot about the CMB, and Alexander Polnarev, who collaborated with me on several papers. I want to thank the POLARBEAR collaboration. They are a great group of people to collaborate with on a CMB experiment. I want to thank the BICEP collaboration for allowing me access to their data at the different frequencies.

To all of the graduate students in the Keating/Paar Cosmology Lab, life in the lab was much more lively with people around. I want to thank everyone in CASS who made life as a graduate student more enjoyable. This includes the people I have grilled with every week for the past several years and everyone who has come to CASS tea time.

I want to finish by thanking my family. I would not have been able to do this without all the support they have given me throughout my time as a graduate student.

Chapter 2 is a reprint of the material as it appears in Physical Review D, Vol. 79, 063008, 2009, Miller, N.J., Shimon, M., and Keating, B.G., "CMB Beam Systematics: Impact on Lensing Parameter Estimation". The dissertation author was the primary investigator and author of this paper.

Chapter 3 is a reprint of the material as it appears in Physical Review D, Vol. 79, 103002, 2009, Miller, N.J., Shimon, M., and Keating B.G. "CMB Polarization Systematics due to Beam Asymmetry: Impact on Cosmological Birefringence". The dissertation author was the primary investigator and author of this paper.

Chapter 4 is a reprint of the material that appears in Monthly Notices of the Royal Astronomical Society, Volume 386, Issue 2, pp 1053-1063, 2008, Polnarev, A.G, Miller, N.J., and Keating, B.G "CMB Temperature Polarization Correlation and Primordial Gravitational Waves" and Advances in Astronomy, 309024, 2009,

Miller, N.J. Keating, B.G., and Polnarev, A.G., ”CMB Temperature Polarization Correlation and Primordial Gravitational Waves: WMAP5”. The dissertation author was the primary investigator and author of these papers.

VITA

2004	A.B. in Mathematics, Princeton University
2008	M.S. in Physics, University of California, San Diego
2012	Ph.D. in Physics, University of California, San Diego

PUBLICATIONS

Keating, B.G., and Miller, N.J., "CMB Optical Depth Measurements: Past, Present, Future", New Astronomy Reviews, 50, 184-190, 2006

Polnarev, A.G., Miller, N.J., and Keating, B.G., "CMB Temperature Polarization Correlation and Primordial Gravitational Waves", Monthly Notices of the Royal Astronomical Society, 386, 1053-1063, 2008

Miller, N.J., Shimon, M., and Keating, B.G, "CMB Beam Systematics: Impact on Lensing Parameter Estimation", Phys. Rev. D, 79, 063008, 2009

Miller, N.J., Keating, B.G., and Polnarev, A.G., "CMB Temperature Polarization Correlation and Primordial Gravitational Waves: WMAP5", Advances in Astronomy, 309024, 2009

Miller, N.J., Shimon, M., and Keating, B.G., "CMB Polarization Systematics due to Beam Asymmetry: Impact on Cosmological Birefringence", Phys. Rev. D, 79, 103002, 2009

Shimon, M., Miller, N.J., Kishimoto, C.T., Smith, C.J., Fuller, G.M., and Keating, B.G. "Using Big Bang Nucleosynthesis to Extend CMB Probes of Neutrino Physics", JCAP, 05 037, 2010

Bierman, E.M., Matsumura, T., Dowell, C.D., Keating, B.G., Ade, P., Barkats, D., Barron, D., Battle, J.O., Bock, J.J., Chiang, H.C., Culverhouse., T.L., Duband, L., Hivon, E.F., Holzapfel, W.L., Hristov, V.V., Kaufman, J.P., Kovac, J.M., Kuo, C.L., Lange, A.E., Leitch, E.M., Mason, P.V., Miller, N.J., Nguyen, H.T., Pryke, C., Richter, S., Rocha, G.M., Sheehy, C., Takahashi, Y.D., Yoon, K.W. "A Millimeter-wave Galactic Plane Survey with the BICEP Polarimeter", Astrophysical Journal, 741, 81, 2011

ABSTRACT OF THE DISSERTATION

Illuminating the Background: Topics in Cosmic Microwave Background Polarization Research

by

Nathan J. Miller

Doctor of Philosophy in Physics

University of California, San Diego, 2012

Professor Brian Keating, Chair

The cosmic microwave background provides a wealth of information about the origin and history of the universe. The statistics of the anisotropy and the polarization of the cosmic microwave background, among other things, can tell us about the distribution of matter, the redshift of reionization, and the nature of the primordial fluctuations. From the lensing of cosmic microwave background due to intervening matter, we can extract information about neutrinos and the equation of state of dark energy. A measurement of the large angular scale B-mode polarization has been called the “smoking gun” of inflation, a theory that describes a possible early rapid expansion of the universe. The focus of current experiments is to measure this B-mode polarization, while several experiments, such

as POLARBEAR, are also looking to measure the lensing of the cosmic microwave background.

This dissertation will discuss several different topics in cosmic microwave background polarization research. I will make predictions for future experiments and I will also show analysis for two current experiments, POLARBEAR and BICEP. I will show how beam systematics affect the measurement of cosmological parameters and how well we must limit these systematics in order to get unbiased constraints on cosmological parameters for future experiments. I will discuss a novel way of using the temperature-polarization cross correlation to constrain the amount of inflationary gravitational waves. Through Markov Chain Monte Carlo methods, I will determine how well future experiments will be able to constrain the neutrino masses and their degeneracy parameters. I will show results from current data analysis and calibration being done on the Cedar Flat deployment for the POLARBEAR experiment which is currently being constructed in the Atacama desert in Chile. Finally, I will analyze the claim of detection of cosmological birefringence in the BICEP data and show that there is reason to believe it is due to systematic effects in the data.

Chapter 1

Introduction to the Cosmic Microwave Background

This chapter is a brief introduction to the cosmic microwave background (CMB), lensing, and cosmological birefringence. In the standard theory of cosmology, the CMB is the radiation left over from the Big Bang. After the Big Bang, but before recombination, photons had enough energy to keep protons and electrons from combining to form neutral hydrogen atoms. The universe was a plasma of photons, electrons, and protons that was opaque to radiation. As the universe expanded and cooled, the photons eventually stopped having enough energy to ionize an electron/proton pair. Around a redshift of 1100, the photons decoupled from the photon-baryon fluid. The universe became transparent to these photons which make up the CMB. They have been freestreaming from recombination until we detect them today in our experiments. The CMB is an almost perfect black body. It is the most precisely known black body that we have measured. The Far Infrared Absolute Spectrophotometer (FIRAS) instrument on the Cosmic Background Explorer (COBE) measured the black body spectrum of the CMB to exquisite precision [4]. A plot of FIRAS's measurements and the best fit Planck spectrum is shown in Fig. 1.1. The measurements are so good that they are contained with the width of the curve.

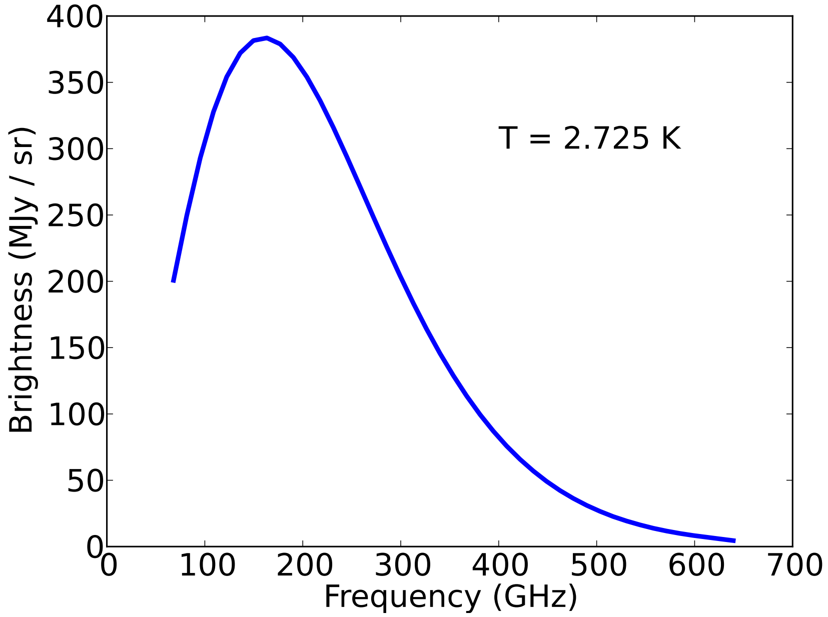

Figure 1.1: A plot of the best fit CMB blackbody spectrum with a temperature of 2.725 K measured by the FIRAS experiment on COBE. The error bars are so small that they are indistinguishable from the best fit curve.

1.1 Temperature Anisotropy

The CMB is nearly uniform across the sky, however temperature variations do exist at the 0.001% level. Before recombination, the photons are tightly coupled to the baryons, therefore a variation in the density of baryons leads to a variation in the temperature of the CMB. Slight non-uniformities in density will grow through the gravitational attraction of the matter. Radiation pressure acts as a restoring force on the baryons, counteracting the gravitational collapse. This leads to acoustic oscillations in the primordial photon-baryon fluid and is the cause of the temperature fluctuations in the CMB.

The temperature of the CMB can be modeled as

$$T(\vec{x}, \hat{p}, \eta) = T(\eta)\left[1 + \Theta(\vec{x}, \hat{p}, \eta)\right] \tag{1.1}$$

The temperature only depends on the direction of photon propagation and not the magnitude of its momentum because the momentum is virtually unchanged during Thomson scattering. Since we observe only here, $\vec{x}_0$, and now, η_0, the CMB anisotropy only depends on the direction of observation. A map of the CMB temperature anisotropy as measured by the Wilkinson Microwave Anistropy Probe (WMAP) experiment is shown in Figure 1.2. The data used to make this map is publically available at the Legacy Archive for Microwave Background Data (LAMBDA)[1].

In order to compare measurements to theoretical predictions, we want to look at the statistics of the anisotropy. We do this by expanding over the spherical harmonics, $Y_{\ell m}$, which are a complete basis.

$$\Theta(\vec{x}_0, \hat{p}, \eta_0) = \sum_{\ell=1}^{\infty} \sum_{m=-\ell}^{\ell} a_{\ell m} Y_{\ell m}(\hat{p}) \tag{1.2}$$

We cannot make any predictions about any specific $a_{\ell m}$, but we can make predictions about the distribution from which they are drawn.

$$\begin{aligned} \langle a_{\ell m} \rangle &= 0 \\ \langle a_{\ell m} a^*_{\ell' m'} \rangle &= \delta_{\ell \ell'} \delta_{m m'} C_\ell \end{aligned} \tag{1.3}$$

---

[1] http://lambda.gsfc.nasa.gov

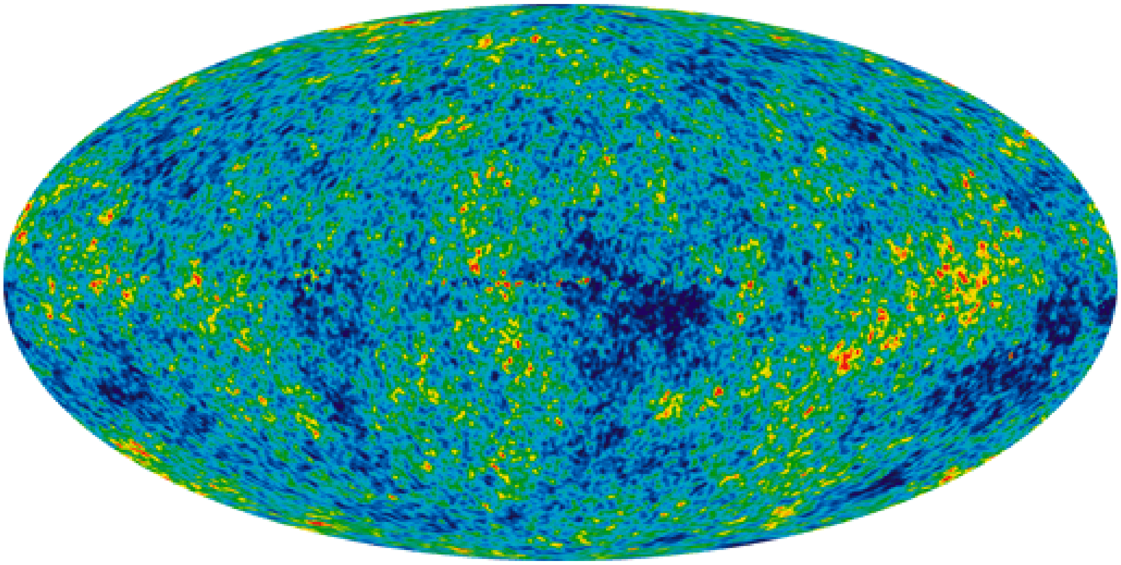

Figure 1.2: A full sky map of the CMB temperature anisotropy from the 7 year WMAP data. The monopole, dipole, and galactic foreground have all been removed.

In summary, the $a_{\ell m}$ are gaussian distributed with mean of zero and a standard deviation of C_ℓ. This C_ℓ is the power spectrum for which we can make predictions given a set of cosmological parameters. We can then compare these predictions to observations. For the temperature anisotropy, we call this the TT power spectrum as we are correlating the temperature anisotropy, T, with itself. A plot of this power spectrum along with the best measurements from the Wilkinson Microwave Anisotropy Probe (WMAP) [5], the South Pole Telescope (SPT) [6], and the Atacama Cosmology Telescope (ACT) [7] is shown in Figure 1.3. As can be seen, this power spectrum has been measured very precisely. In these plots, large angular scales correspond to small ℓ and small angular scales correspond to large ℓ. In fact, $\theta \approx 180^\circ/\ell$.

As can be seen in Figure 1.3, there are many peaks in the CMB TT power spectrum. These are caused by acoustic oscillations in the primordial photon-baryon fluid. Because the perturbations are very small, the equations governing the evolution of the anisotropy are linear and the different Fourier modes evolve independently from one another [8, 9]. The oscillations of the photon-baryon fluid

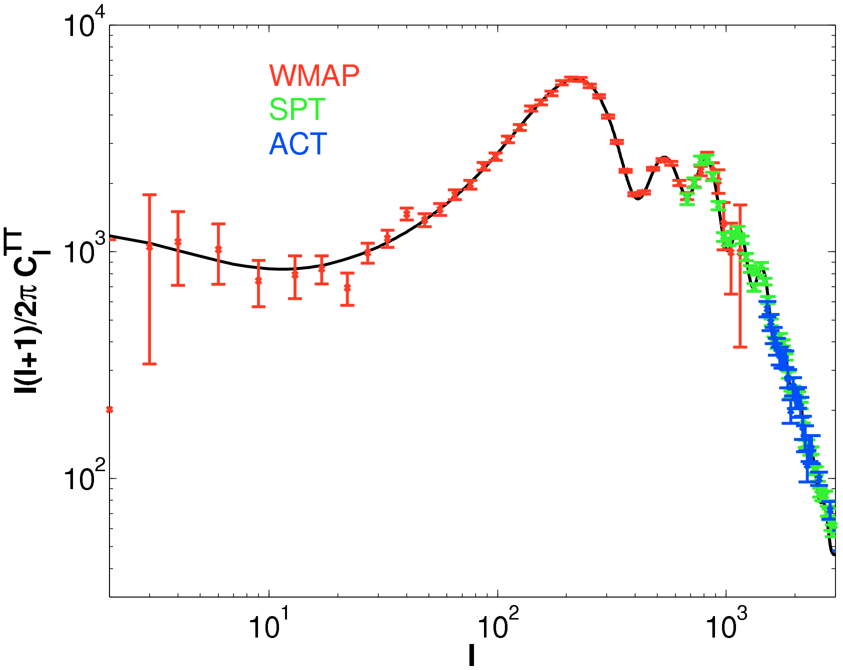

Figure 1.3: A plot of the TT power spectrum along with measurements from WMAP (red), SPT (green), and ACT (blue). The theoretical power spectrum is generated using the WMAP7 best-fit ΛCDM model.

end at recombination. At that point, the phase of each mode is frozen into the CMB. Modes which are at either a maximum compression or maximum rarefaction at recombination are the peaks we see in the CMB TT power spectrum today. The first peak (lowest ℓ) corresponds to the mode that has compressed a single time since the Big Bang, while the second peak corresponds to a mode that has compressed and rarefied once. The higher peaks correspond to modes that have compressed and rarefied more than once. Modes with smaller wavelengths will have compressed and rarefacted more than modes with longer wavelengths. The amplitude and location of the peaks in the CMB give us information about different cosmological parameters. The location of the first peak can tell us whether we have an open, closed, or flat universe. The amplitude of the even numbered peaks relative to the odd numbered peaks provides information about the baryon density. We can also learn about the amount of dark energy, the total matter density, and the redshift of reionization among other cosmological parameters from the measurements of these peaks.

For modes with a wavelengths long enough (small ℓ) such that they are unable to evolve significantly before recombination, their amplitude at recombination corresponds to their initial values. This area is known as the Sachs-Wolfe plateau and the CMB power spectrum on these large angular scales goes as $C_\ell \propto \frac{1}{\ell(\ell+1)}$. At the other end of the CMB angular power spectrum, we have the Silk damping tail. Recombination did not occur instantaneously. It occurred over finite period of time. During this time, photons diffused from the overdense regions to the underdense regions. When they did this, they brought along protons and electrons and damped the anisotropy over those scales. This is known as Silk damping and it is why the CMB power spectrum decays exponentially at small scales (large ℓ).

As mentioned earlier, a requirement for the temperature anisotropy in the CMB is density perturbations in the early universe as the photons are coupled to the baryons, however we did not specify how these early fluctuations are generated. It is usually assumed that inflation generates these early fluctuations, but we will not do this. We will assume that the power spectra of primodial density fluctuations per log interval of k is modeled as $P(k) = A_s(k/k_0)^{n_s-1}$, where A_s

is the amplitude of scalar fluctuations and n_s is the scalar spectral index. The pivot wavenumber k_0 is taken to be 0.05 Mpc^{-1}, except in Chapter 4 where it is taken at 0.002 Mpc^{-1}. The parameters describing this primordial power spectrum, A_s and n_s, are also constrained by measurements of the CMB temperature power spectrum.

1.2 Polarization

In addition to the variations in temperature, the CMB is also slightly polarized. This polarization encodes even more information about the CMB and can break some degeneracies between parameters that occur when only measuring the temperature anisotropy. This polarization will be generated by Thomson scattering off free-electrons if a certain set of requirements are met [1]. Thomson scattering is the elastic scattering of electromagnetic radiation off of a free electron, described by classical electromagnetism. The incident radiation accelerates the electron, which causes it to emit radiation at the same frequency as the incoming radiation. Because the electric field oscillates, the particle will be oscillating in the direction of the electric field, which results in electric dipole radiation. For an unpolarized incident beam of photons, this will accelerate the electron in the plane perpendicular to the propagation direction of the incident wave. The outgoing radiation's wavevector is perpendicular to a direction of oscillation. If we are an observer in the plane of the oscillation, then the observed outgoing radiation must be polarized. However, if there is incident electromagnetic waves coming from all different directions, then this polarization is wiped out. This polarization can be recovered if there is a local temperature anisotropy. This is shown in Figure 1.4, which is taken from [1].

1.2.1 Q/U and E/B

The Stokes parameters describe the polarization state of an electromagnetic field. The parameter I describes the intensity while Q and U describe the linear polarization. The final Stokes parameter, V, is the amount of circular polarization.

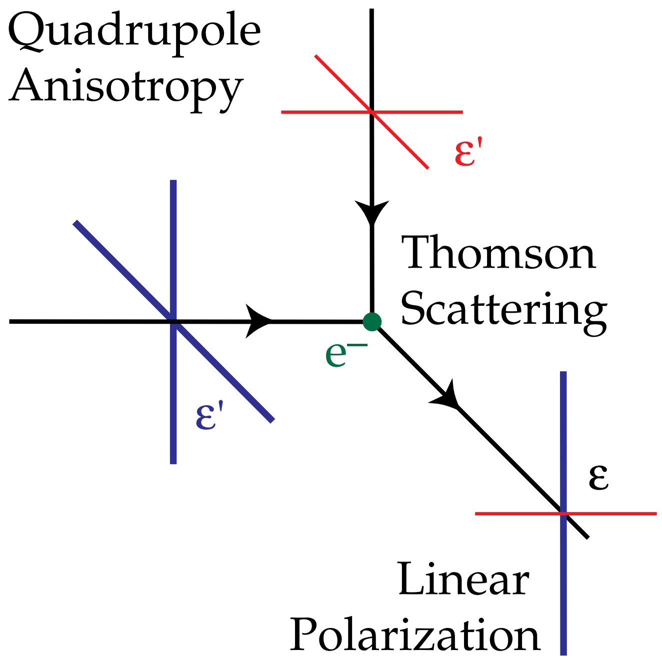

Figure 1.4: Thomson scattering of radiation with a quadrupole anisotropy generates linear polarization. Blue colors (thick lines) represent hot radiation and red colors (thin lines) represent cold radiation. This is Figure 1 of [1]

Since Thomson scattering can only produce linear polarization, V is assumed to be zero for the CMB. For a plane wave propagating along the z-axis, the Stokes parameters are

$$\begin{aligned} I &= |E_x|^2 + |E_y|^2 \\ Q &= |E_x|^2 - |E_y|^2 \\ U &= 2\,\Re\left(E_x^* E_y\right) \\ V &= 2\,\Im\left(E_x^* E_y\right) \end{aligned} \tag{1.4}$$

where E_x and E_y are the amplitudes of the radiation in the x and y directions, respectively. CMB experiments measure the I, Q, and U Stokes parameters. The definition of Q and U depend on your coordinate system. $Q \pm iU$ is a spin ± 2 field. Upon rotation of the coordinate system about the z-axis by an angle θ, they transform as

$$Q^{'} \pm iU^{'} = (Q \pm iU)\exp(\pm 2i\theta). \tag{1.5}$$

In Fourier space, the analogues to Q and U are E and B. We can expand $Q \pm iU$ over spin-2 spherical harmonics. Doing this we get

$$a^E_{\ell m} \pm i a^B_{\ell m} = \int d\Omega (Q \pm iU)_{\pm 2} Y^*_{\ell m}(\hat{n}). \tag{1.6}$$

We can then construct the polarization power spectra

$$\begin{aligned} C_\ell^{TE} &= \left\langle a^{T*}_{\ell m} a^E_{\ell m} \right\rangle \\ C_\ell^{TB} &= \left\langle a^{T*}_{\ell m} a^B_{\ell m} \right\rangle \\ C_\ell^{EE} &= \left\langle a^{E*}_{\ell m} a^E_{\ell m} \right\rangle \\ C_\ell^{BB} &= \left\langle a^{B*}_{\ell m} a^B_{\ell m} \right\rangle \\ C_\ell^{EB} &= \left\langle a^{E*}_{\ell m} a^B_{\ell m} \right\rangle \end{aligned} \tag{1.7}$$

however due to parity symmtery, C_ℓ^{TB} and C_ℓ^{EB} are expected to be zero. In Section 1.4, we will discuss a modification to the standard model that will generate non-zero C_ℓ^{TB} and C_ℓ^{EB}. In addition, density perturbations do not generate any B modes. As such, the BB power spectrum will be zero. A plot of the TE and EE power spectrum along with the best measurements from WMAP, BICEP [10], QUaD [11], and QUIET [12] are shown in Figures 1.5 and 1.6.

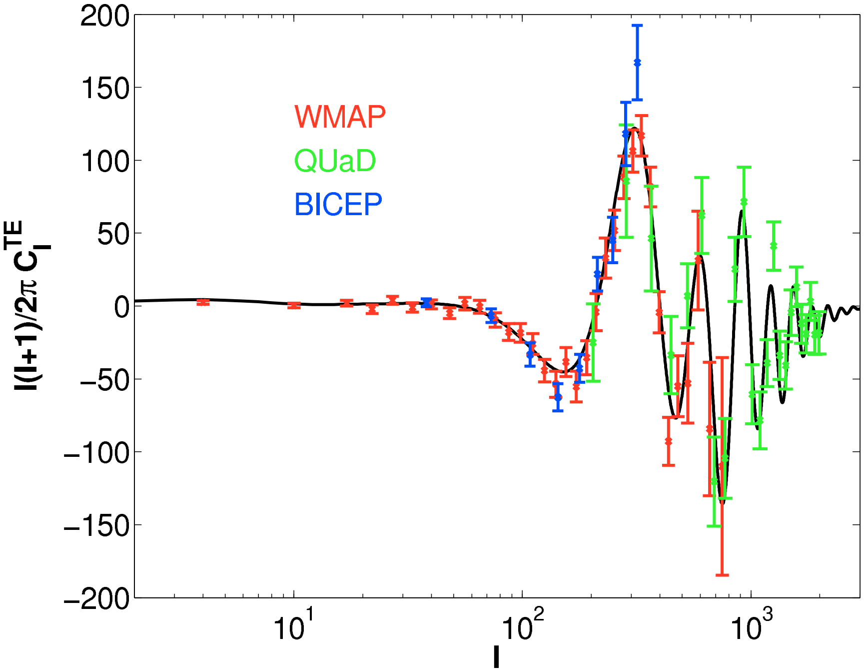

Figure 1.5: A plot of the TE power spectrum along with measurements from WMAP (red), QUaD (green), and BICEP (blue). The power spectrum is generated using the WMAP7 best-fit ΛCDM model.

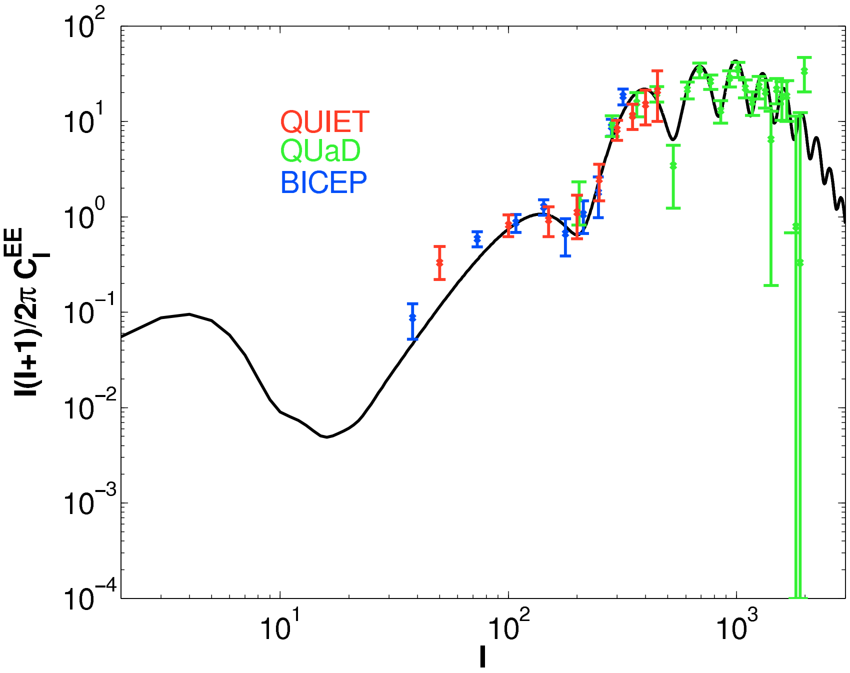

Figure 1.6: A plot of the EE power spectrum along with measurements from QUIET (red), QUaD (green), and BICEP (blue). The power spectrum is generated using the WMAP7 best-fit ΛCDM model.

1.2.2 Primordial Gravitational Waves

Primordial gravitational waves (PGW) can also produce temperature fluctuations and polarize the CMB. A primordial gravitational wave can provide the local quadrupole temperature anisotropy needed to generate polarization. However, unlike density perturbations, PGWs can generate B-mode polarization. Detecting these PGWs through measurements of the BB power spectrum is the main focus of CMB polarization experiments today. The only theory we currently have that can generate enough PGWs to produce a detectable level of the BB power spectrum is inflation. If is therefore why a measurement of a non-zero CMB BB power spectrum has been called the "smoking gun" of inflation. However, as with the density fluctuations, we will not consider any specific model when dealing with PGWs. We will assume that there is a power spectrum of primordial tensor fluctuations per log arithmic interval of k that scales as $P_t(k) = A_t(k/k_0)^{n_t}$. As with density fluctuations, A_t is the amplitude of tensor fluctuations, n_t is the tensor spectral index, and k_0 is the pivot wavenumber. The focus of the CMB experiments is to measure and constrain $r \equiv A_t/A_s$, the tensor-to-scalar ratio. A plot of the CMB BB power spectrum due to PGWs with the WMAP7 ΛCDM model and $r = 0.1$ is shown in Figure 1.7, along with the upper limits from the BICEP, QUaD, and QUIET experiments. The best constraint on r using only measurements of the BB power spectrum is $r < 0.72$ at 95% confidence from BICEP [10].

1.3 Lensing of the CMB

The CMB has been free-streaming since recombination at $z \approx 1100$. While the photons have not scattered off of electrons since last scattering, they have moved through gravitational fields generated by matter which has become increasingly non-uniform. According to general relativity, the path of light is bent in a gravitational field. A non-uniform distribution of matter will produce a non-uniform gravitational field. The CMB photons that we see today have been lensed by the matter in the universe as they have propagated to us from last-scattering. An excellent review of the theory behind the gravitational lensing of the CMB is

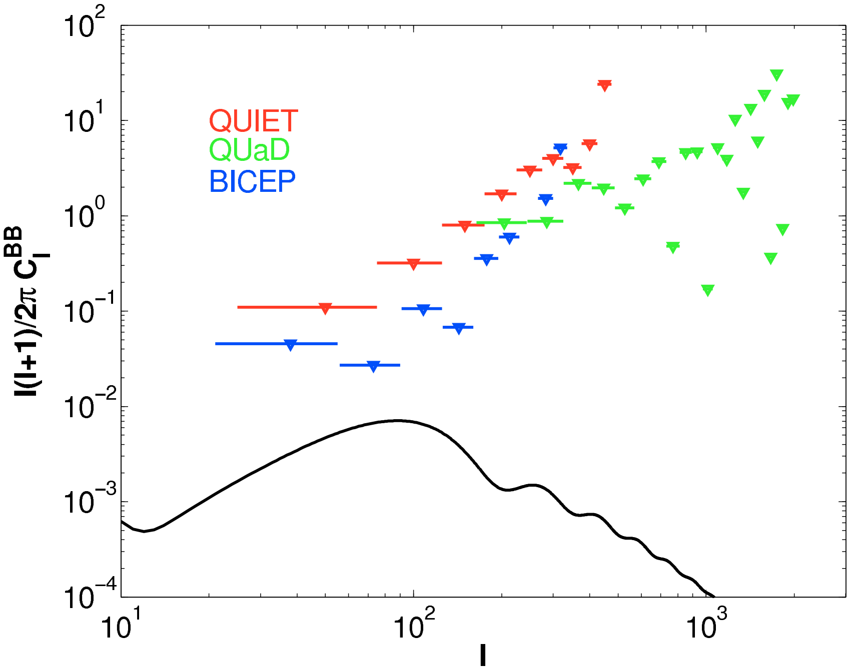

Figure 1.7: A plot of the BB power spectrum with $r = 0.1$ along with 2σ upper limits from QUIET (red), QUaD (green), and BICEP (blue). The power spectrum is generated using the WMAP 7 best-fit ΛCDM model with the additional parameter of $r = 0.1$.

[13].

The lensing potential $\phi(\hat{n})$ will remap the the temperature anisotropy and polarization by

$$\begin{aligned} \Theta(\hat{n}) &= \tilde{\Theta}(\hat{n} + \nabla\phi(\hat{n})) \\ \mathcal{P}_{ij}(\hat{n}) &= \tilde{\mathcal{P}}_{ij}(\hat{n} + \nabla\phi(\hat{n})) \end{aligned} \quad (1.8)$$

where the tildes denote the unlensed fields and the variables without tildes refer to the lensed fields. The lensing potential depends on the distribution of matter from last scattering to today. A plot of the difference between the lensed and unlensed power spectra is shown in Figure 1.8. Lensing has an effect of smoothing the primordial power spectra. In addition, the lensed BB power spectra has a significant amount of extra power on the small scales. Lensing converts some amount of E mode polarization to B mode polarization, so even if $r = 0.0$ there will be some non-zero B mode polarization on small scales. This contaminates measurements of the BB power spectrum and must be dealt with if we want to detect the B modes due to PGWs.

Because lensing introduces non-gaussianities into the CMB, we can delense the CMB power spectra and extract information about the lensing potential. A quadratic estimator of the lensing potential and the uncertainties in this estimator are described in [14, 15]. We usually look at the power spectrum of the deflection angle, $\mathbf{d}(\hat{n}) = \nabla\phi(\hat{n})$. A plot of the deflection angle power spectrum is shown in Figure 1.9. The shape of this power spectrum is determined by cosmological parameters which affect structure formation. We can therefore use measurements of the dd power spectrum, where d is the amplitude of $\mathbf{d}$, to constrain these parameters, such as w, the equation of state of dark energy, or parameters describing mass of the different neutrinos.

1.4 Cosmological Birefringence

In the standard Big Bang cosmology, parity symmetry is respected. The CMB's E and B-modes are pure parity states (even and odd, respectively). Since

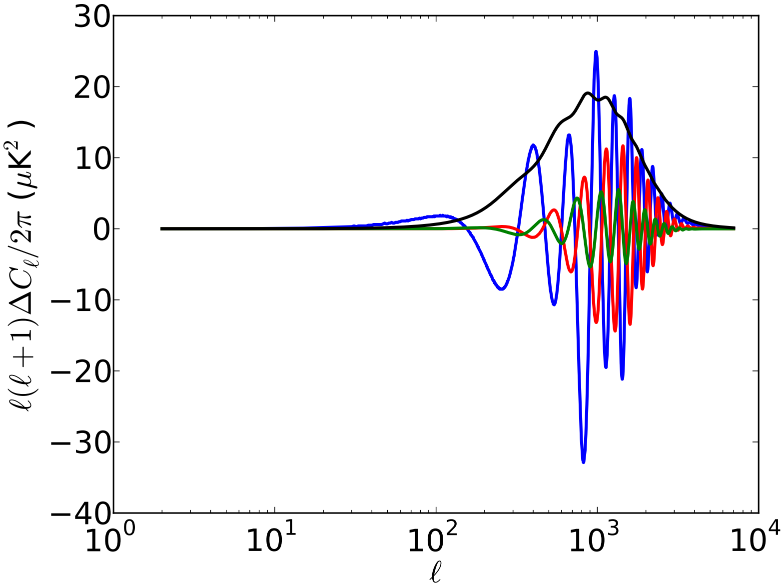

Figure 1.8: A plot of the change in the CMB power spectra due to lensing. The blue line is the change in the TT power spectrum. The green line is the change in the TE power spectrum. The red line is ten times the change in the EE power spectrum. The black line is 300 times the change in the BB power spectrum.

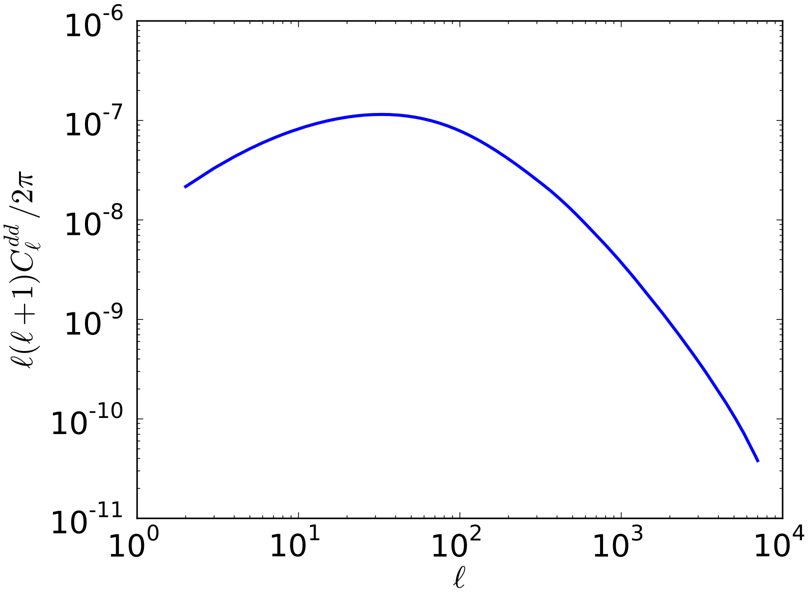

Figure 1.9: A plot of the deflection angle power spectrum of the CMB.

T and E are even parity and B is odd parity, it means that the TB and EB power spectra should vanish. If, for some reason, the direction of linear polarization has been rotated since recombination, then there will be an E-B mixing which introduces the "forbidden" TB and EB power spectra. A rotation of the direction of polarization will leave the temperature unchanged, but will affect the polarization state. As mentioned in Section 1.2.1, $Q \pm iU$ are spin-±2 states. Under a rotation by α, they pick up phases $e^{\pm 2i\alpha}$. From the definition of $a_{\ell m}^{E}$ and $a_{\ell m}^{B}$ in Eq. 1.6, we can see that a rotation of the polarization state results in a mixing of E and B:

$$\begin{aligned} a_{\ell m}^{E'} &= a_{\ell m}^{E}\cos 2\alpha - a_{\ell m}^{B}\sin 2\alpha \\ a_{\ell m}^{B'} &= a_{\ell m}^{E}\sin 2\alpha + a_{\ell m}^{B}\cos 2\alpha, \end{aligned} \tag{1.9}$$

and $a_{\ell m}^{T'} = a_{\ell m}^{T}$ since temperature is unaffected. We can therefore construct the modified power spectra. We get

$$\begin{aligned}
C_\ell^{\prime TE} &= C_\ell^{TE} \cos(2\alpha) \\
C_\ell^{\prime TB} &= C_\ell^{TE} \sin(2\alpha) \\
C_\ell^{\prime EE} &= C_\ell^{EE} \cos^2(2\alpha) + C_\ell^{BB} \sin^2(2\alpha) \\
C_\ell^{\prime BB} &= C_\ell^{EE} \sin^2(2\alpha) + C_\ell^{BB} \cos^2(2\alpha) \\
C_\ell^{\prime EB} &= \frac{1}{2}\left(C_\ell^{EE} - C_\ell^{BB}\right) \sin(4\alpha). \qquad (1.10)
\end{aligned}$$

A cosmological source of this rotation, as described in [16], is dubbed "cosmological birefringence" (CB). The parameter α is dubbed the "cosmological birefringence angle". The main feature of Eq. 1.10 is that the TB and EB power spectra are not identically zero. It is the measurements of these two power spectra that are used to constrain the amount of CB in the universe.

Chapter 2

Beam Systematics and Lensing Parameter Estimation

2.1 Introduction

The standard cosmological model accounts for a multitude of phenomena occurring over orders of magnitude of length and angular scales throughout the entire history of cosmological evolution. Remarkably, doing so only requires about a dozen parameters. Perhaps one of the most useful cosmological probes is cosmic microwave background (CMB) temperature anisotropy whose physics is well understood. Complementary cosmological probes can assist in breaking some of the degeneracies inherent in the CMB and further tighten the constraints on the inferred cosmological parameters. Temperature anisotropy alone cannot capture all the cosmological information in the CMB, and its polarization probes new directions in parameter space. B-mode polarization observations are noise-dominated but the robust secondary signal associated with gravitational lensing, which is known up to an uncertainty factor of two on all relevant scales, is at the threshold of detection by upcoming CMB experiments. The lensing signal may have been detected already through its signature on the CMB anisotropy as reported recently by ACBAR [17]. Lensing by the large scale structure (LS) also converts primordial E-mode to secondary B-mode. When high fidelity B-mode data are available a wealth of information from the inflationary era [18, 19], and cosmological parameters that control the evolution of small scale density perturbations (such as the running of the spectral index of primordial density perturbations, neutrino mass and dark energy equation of state), will be extracted from the CMB. At best, B-mode polarization from lensing is a factor of three times smaller than the primordial E-mode polarization, so it is prone to contamination by both astrophysical foregrounds and instrumental systematics. It is mandatory to account for, and remove when possible, all sources of spurious B-mode in analyzing upcoming CMB data, especially those generated by temperature leakage due to beam mismatch, since temperature anisotropy is several orders of magnitude larger than the expected B-mode level produced by lensing.

Beam systematics have been discussed extensively [20, 21, 22, 2]. All the effects are associated with beam imperfections or beam mismatch in dual beam experiments, i.e. where the polarization is obtained by differencing two signals which are measured simultaneously by two beams with two orthogonal polarization axes. Fortunately, several of these effects (e.g. differential gain, differential beam width and the first order pointing error - 'dipole'; [20, 22, 2]) are reducible with an ideal scanning strategy and otherwise can be cleaned from the data set by virtue of their non-quadrupole nature which distinguishes them from genuine CMB polarization signals. Other spurious polarization signals, such as those due to differential ellipticity of the beam, second order pointing errors and differential rotation, persist even in the case of ideal scanning strategy and perfectly mimic CMB polarization. These represent the minimal spurious B-mode signal, residuals which will plague every polarization experiment. We refer to them in the following as 'irreducible beam systematics'. We assume throughout that beam parameters are spatially constant. Two recent works considered the effect of spatially-dependent systematic beam-rotation and differential gain, respectively [23, 24]. This scale-dependence and the associated new angular scale induce non-trivial higher order correlation functions through non-gaussianities which can be both used to optimally remove the space-dependent component of beam rotation [23] and mimic the CMB lensing signal, thereby biasing the quadratic estimator of the lensing potential [24].

To calculate the effect of beam systematics we invoke the Fisher information matrix formalism as well as Monte Carlo simulations of parameter extraction, the latter for the first time. Our objective is to determine the susceptibility of the above mentioned, and other, cosmological parameters to beam systematics. For the Fisher-matrix-based method and the Monte Carlo simulations we calculate the underlying power spectrum using CAMB[1] [25]. The Monte-Carlo simulations are carried out with CosmoMC[2] [26]. We represent the extra noise due to beam systematics by analytic approximations [2] and include lensing extraction in the parameter inference process, following [27, 28] (see also [29] for the Monte Carlo simulations) for neutrino mass (and other cosmological parameters) reconstruction from CMB data.

This paper illustrates the effect of beam systematics and its propagation to parameter estimation and error forecasts for upcoming experiments. Our main concern is the effect on the following cosmological parameters: the tensor-to-scalar ratio r, the total neutrino mass M_ν (assuming three degenerate species), tilt of the scalar index α, dark energy equation of state w, and the spatial curvature, Ω_k. The lensing-induced B-mode signal is sensitive to all parameters (except the tensor-to-scalar ratio) and peaks at few arcminute scales, while the tensor-to-scalar ratio depends on the energy scale of inflation and the primordial signal peaks at the characteristic horizon size at last scattering, $\approx 2^\circ$. We note that while the LSS-induced and primordial tensor power B-mode spectra are sub-μK the *shape* of the primordial B-mode spectrum is known (only its amplitude is unknown [30]) and the secondary LSS-induced B-mode is guaranteed to exist by virtue of the known existence of LSS and E-mode polarization.

The chapter is organized as follows. We describe the formalism of beam systematics for general non-gaussian beams and provide a cursory description of a critical tool to mitigate polarization systematics -a half wave plate (HWP), in Section 2.2. The effect of lensing on parameter extraction within the standard quadratic-estimators formalism is discussed in Section 2.3 The essentials of the Fisher matrix formalism are given in Section 2.4 as well as some details on the

---

[1] http://camb.info

[2] http://cosmologist.info/cosmomc

Monte Carlo simulations invoked here. Our results are described in Section 2.5 and we conclude with a discussion of our main findings in Section 2.6.

2.2 Beam systematics

Beam systematics due to optical imperfections depend on both the underlying sky, the properties of the polarimeter and on the scanning strategy. Temperature anisotropy leaks to polarization when the output of two slightly different beams with orthogonal polarization-sensitive directions is being differenced. A trivial example is the effect of differential gain. If the two beams have the same shape, width, etc. except for different overall response, i.e. normalization, the difference of the measured intensity will result in a non-vanishing polarization signal. Similarly, if two circular beams slightly differ by their width this will again induce a non-vanishing polarization upon taking the difference (see Fig. 2 of [2]). The spurious polarization will be proportional to temperature fluctuations on scales comparable to the difference in beamwidths, which, due to the circular symmetry of the problem, will be proportional to second order gradients of the temperature anisotropy. To eliminate these effects this beam imperfection has to couple to non-ideal scanning strategy as described in [2] and below. A closely related effect, which does not couple to scanning strategy, is the effect of differential beam ellipticity. Here, the spurious polarization scales as the second order gradient of the temperature anisotropy to leading order. Another effect, widely described in the literature, which again couples beam asymmetry and temperature anisotropy to scanning strategy is the effect due to differential pointing. The idea is simple; if two beams point at two slightly different directions they will statistically measure two different intensities proportional to fluctuations of the background radiation on these particular scales. The difference, which may be naively regarded as polarization, is non-vanishing in this case provided the scanning strategy is non-ideal and contains either a dipole and/or an octupole [2]. Finally, the effect of beam rotation we consider in this work is due to uncertainty in the overall beam orientation. This mixes the Q and U Stokes parameters and as a result also leaks E to B and vice versa. A constructive order-of-magnitude example is the effect of differential pointing. This effect depends on the temperature gradient to first order. The rms CMB temperature gradients at the 1°, $30'$, $10'$, $5'$ and $1'$ scales are ≈ 1.4, 1.5, 3.5, 2.5 and 0.2 μK/arcmin, respectively. Therefore, any temperature difference measured with a dual-beam experiment (with typical beamwidth few arcminutes) with a $\approx 1'$ pointing error will result in a $\approx 1\mu$K systematic polarization which has the potential to overwhelm the B-mode signals.

Similarly, the systematic induced by differential ellipticity results from the variation of the underlying temperature anisotropy along the two polarization-sensitive directions which, in general, differ in scale depending on the average beamwidth, degree of ellipticity and the tilt of the polarization-sensitive direction with respect to the ellipse's principal axes. For example, the temperature difference measured along the major and minor axes of a 1° beam with a 2% ellipticity scales as the second gradient of the underlying temperature which on this scale is $\approx 0.2\mu K/\text{arcmin}^2$ and the associated induced polarization is therefore expected to be on the $\approx \mu K$ level. The spurious signals due to pointing error, differential beamwidth and beam ellipticity all peak at angular scales comparable to the beam size. If the beam size is $\approx 1^\circ$ the beam systematics mainly affect the deduced tensor-to-scalar ratio, r. If the polarimeter's beamwidth is a few arcminutes the associated systematics will impact the measured neutrino mass m_ν, spatial curvature Ω_k, running of the scalar spectral index α and the dark energy equation of state w (which strongly affects the lensing-induced B-mode signal). It can certainly be the case that other cosmological parameters will be affected as well.

Two other spurious polarization signals we explore are due to differential gain and differential rotation; these effects are associated with different beam 'normalizations' and orientation, respectively, and are independent of the coupling between beam substructure and the underlying temperature perturbations. In particular, they have the same scale dependence as the primordial temperature anisotropy and polarization power spectra (as long as the differential gain and beam rotation are spatially independent; this of course changes if they depend on space [23, 24]), respectively, and their peak impact will be on scales associated with the CMB's temperature anisotropy ($\approx 1^\circ$) and polarization ($\approx 10'$).

2.2.1 Mathematical Formalism

We work entirely in Fourier space and in this section we generalize our results to the case of the most general beam shapes [2]. Although the tolerance levels on the beam parameters we derive in Sections 2.4 and 2.5 are based on the assumption of elliptical beams, they can be easily generalized to arbitrary beam shape, given the beam profile, as we describe below. This can be used to adapt our results to actual measured beam maps incorporating other classes of beam non-ideality such as sidelobes.

We expand the temperature anisotropy and Q and U Stokes parameters in 2-D plane waves since for sub-beam scales this is a good approximation. While the (spin-0) temperature anisotropy is expanded in scalar plane waves $e^{i\mathbf{l}\cdot\mathbf{r}}$, the (spin ± 2) polarization tensor $Q + iU$ is expanded in tensor plane waves $e^{i\mathbf{l}\cdot\mathbf{r}} e^{\pm 2i(\phi_{\mathbf{l}} - \phi_{\mathbf{r}})}$ where $\phi_{\mathbf{r}}$ is the angle defining the direction of the radius-vector r in real space as conventional (in an arbitrarily coordinate system on the sky ϕ_r is the azimuthal angle along the line of sight) and $\phi_{\mathbf{l}}$ defines the direction of the wave-vector $\mathbf{l}$ in l-space in a coordinate-system fixed to the beam as defined below, in Eq. 2.2. Since in real space the temperature and polarization fields are convolved with the polarimeter's beams, these expressions are simply the product of their Fourier transforms in Fourier space. For a general beam $B(\mathbf{r})$ the measured 2-D polarized beam map may exhibit a pointing error ρ. In this case, the Fourier transform of the beam function acquires a phase

$$\tilde{B}(\mathbf{l}) \to \tilde{B}(\mathbf{l}) \exp(i\mathbf{l} \cdot \rho). \tag{2.1}$$

It is useful to switch to polar coordinates at this point, where we define

$$\begin{aligned} l_x &= l \cos(\phi_{\mathbf{l}} + \psi - \alpha) \\ l_y &= l \sin(\phi_{\mathbf{l}} + \psi - \alpha) \\ \rho_x &= \rho \cos\theta \\ \rho_y &= \rho \sin\theta \end{aligned} \tag{2.2}$$

and $\alpha \equiv \beta + \theta + \psi$ is the angle of the polarization axis in a coordinate system fixed to the sky (Fig. 1 of [2]). The Fourier representation of an *arbitrary* beam then becomes

$$\begin{aligned} \tilde{B}(\mathbf{l}) &= \int B(\mathbf{r}) e^{i\mathbf{l}\cdot\mathbf{r}} d^2\mathbf{r} \\ &= \int B(\mathbf{r}) e^{ilr\cos(\phi_l+\psi-\alpha-\phi_r)+il\rho\cos(\phi_l+\theta+\psi-\alpha-\phi_r)} d^2\mathbf{r} \\ &\equiv \sum_{m,n} B_{m,n}(l) e^{i(m+n)(\phi_l-\alpha)} \end{aligned} \tag{2.3}$$

where

$$\begin{aligned} B_{m,n}(l) &= i^{m+n} J_n(l\rho) e^{i(m+n)\psi+in\theta} \\ &\times \int r dr J_m(lr) \int d\phi_r B(\mathbf{r}) e^{-i(m+n)\phi_r}, \end{aligned} \tag{2.4}$$

and in the last step we employed the expansion of 2-D plane waves in terms of cylindrical Bessel functions

$$e^{il\rho\cos(\phi_l-\phi_\rho)} = \sum_{n=-\infty}^{n=\infty} i^n J_n(l\rho) e^{in(\phi_l-\phi_\rho)}. \tag{2.5}$$

As in [2], the optimal map constructed from the CMB data depends on the measurements as

$$\begin{aligned} \tilde{m}(\mathbf{p}) &= \left(\sum_{t,j\in\mathbf{p}} A_j^T(\mathbf{p},t) A_j(\mathbf{p},t) \right)^{-1} \\ &\times \left(\sum_{t,j\in\mathbf{p}} A_j^T(\mathbf{p},t) d_j(\mathbf{p},t) \right) \end{aligned} \tag{2.6}$$

where the sums run over all measurements of the pixel $\mathbf{p}$. The pointing vector A is given by

$$A = \left(1, \frac{1}{2} e^{2i\alpha(\mathbf{p},t)}, \frac{1}{2} e^{-2i\alpha(\mathbf{p},t)} \right), \tag{2.7}$$

α is a function of both the pixel $\mathbf{p}$ and t, and A^T is A transposed. Once the leading beam coefficients $B_{m,n}(l)$ have been calculated, the induced power spectra of the systematics can be calculated according to Eqs. (24), (33), (A.1) and (A.2) of [2].

Several of the beam systematics can be mitigated by employing a rotating half wave plate (HWP) polarization modulator (e.g. [31, 32, 33]). These can operate in continuous or stepped rotation. When HWP modulators are included we replace the above scanning angle $\alpha(\mathbf{p},t)$ with $\alpha(\mathbf{p},t) + 2\varphi t$ where φ is the angular velocity of the HWP [22]. Our deduced tolerance levels given below are presented in a fashion independent of the details of the scanning strategy; all the information about the scanning strategy is encapsulated in the functions f_1, f_2 and f_3:

$$\begin{aligned} f_1 &\equiv \frac{1}{2}|\tilde{h}_+(-1,0)|^2 \\ f_2 &\equiv \frac{1}{2}|\tilde{h}_+(-1,-1)|^2 + \frac{1}{2}|\tilde{h}_+(-1,1)|^2 \\ f_3 &\equiv \frac{1}{2}\langle \tilde{f}(0,1)\tilde{h}^*_-(1,-1)\rangle \end{aligned} \tag{2.8}$$

where

$$\begin{aligned} f(m,n) &\equiv \langle e^{-i(2m+n)\alpha(\mathbf{p},t)}\rangle \\ h_\pm(m,n) &\equiv \frac{1}{D}[f(m,n) - f(m\pm 2,n)\langle e^{\pm 4i\alpha(\mathbf{p},t)}\rangle] \\ D &\equiv 1 - \langle e^{-i4\alpha(\mathbf{p},t)}\rangle\langle e^{i4\alpha(\mathbf{p},t)}\rangle \end{aligned} \tag{2.9}$$

and the angular brackets in $\langle e^{in\alpha(\mathbf{p},t)}\rangle$ represent average over measurements of a single pixel $\mathbf{p}$, averaged over time. In these averages $\alpha(\mathbf{p},t) \to \alpha(\mathbf{p},t) + 2\varphi t$, and therefore even if the scanning strategy does not uniformly cover all polarization angles α of a given spatial pixel, the HWP mitigates the spurious polarization caused by beam systematic effects if integrated over long time intervals. If the hexadecapole of the scanning strategy is negligible, the scanning strategy function f_1 depends only on the quadrupole moment of the scanning strategy while f_2 encapsulates information on both the dipole and octupole moments of the scanning strategy.

At this point, it is instructive to show how, in the case of an ideal scanning strategy the first order pointing effect vanishes. As can be seen from Table 2.2 this effect involves a convolution of the beam function and underlying temperature anisotropy power spectrum with f_2 in multipole space. From the above definitions

$$\begin{aligned} h_+(-1,-1) &= 1/D\left[\langle e^{3i\alpha}\rangle - \langle e^{-i\alpha}\rangle\langle e^{4i\alpha}\rangle\right] \\ h_+(-1,1) &= 1/D\left[\langle e^{i\alpha}\rangle - \langle e^{-3i\alpha}\rangle\langle e^{4i\alpha}\rangle\right] \\ h_-(1,-1) &= h_+^*(-1,1) \end{aligned} \tag{2.10}$$

and therefore if with each scanning angle α there is associated an angle $\alpha + 180°$ the f_2 (Eqs. 2.8 and 2.10) vanishes in real space and so does its Fourier transform. Note that even if the scanning strategy is *non-ideal* f_2 will vanish provided that for each angle α the angle $\alpha + 180°$ is sampled the same number of times per pixel. This suggests that the *dipole* systematic can be completely removed by removing all data points that contribute to $h_+(-1,-1)$ and $h_+(-1,1)$, i.e. those measurements at α for which $\alpha + 180°$ is not sampled. Similar considerations apply to f_1 which controls the level of the differential beamwidth- and differential gain-induced systematics (see Table 2.2).

2.2.2 Simplifying Scan Strategy Effects

When the polarization angle at each pixel on the sky is uniformly sampled the average $\langle e^{in\alpha}\rangle$ vanishes for every $n \neq 0$. In this case the scanning strategy is referred to as an *ideal scanning strategy*. For uniform, but non-ideal, scanning strategies, the scanning functions f_1, f_2 and f_3 mentioned above (which are combinations of $\langle e^{in\alpha}\rangle$) are non-vanishing even when $n > 0$ but uniform in real space. As a result their Fourier transforms are unnormalized delta-functions (the actual amplitudes are directly related to the average values $\langle e^{in\alpha}\rangle$), and the convolutions in Fourier space shown in Tables III-IV of [2] become trivial. To determine the tolerance level for beam parameters we assume such uniform scanning strategies.

A uniform scanning strategy is a particularly useful example. A nearly-uniform scanning strategy can be reasonably approximated by a sum over a few lowest multipoles, such as

$$\tilde{f}_i(l) = \sum_{l'=0}^{l'_{max}} f'_i(l')\delta(l-l')/(l-l'). \tag{2.11}$$

Here $|l_{max}|$ is assumed sufficiently small, and $i = 1$ or 2, where f_1, f_2 and f_3 are defined in Eq. 2.8). In this case the ℓ-mode mixing due to the convolution of the underlying power spectra and the scanning functions as in Table 2.2 ($\star$ stands for convolution in multipole space). $\tilde{f}_i$ can be written as

$$\begin{aligned}\tilde{f}_i \star C_l^T &\approx \frac{f_i}{2\pi} \cdot C_l^T \\ f_i &\equiv \sum_{l'=1}^{l'_{max}} f_i'(l'). \end{aligned} \tag{2.12}$$

We assume here that the nonvanishing multipoles of $\tilde{f}_i$ are concentrated near 0, i.e. that the scanning strategy is non-ideal, yet approximately uniform. We have employed this simplifying assumption throughout.

2.3 The Effect of Systematics on Lensing Reconstruction

Gravitational lensing of the CMB is both a nuisance and a valuable cosmological tool (e.g. [34]). It certainly has the potential to complicate CMB data analysis due to the non-gaussianity it induces. However, it is also a unique probe of the growth of structure in the linear, and mildly non-linear, regimes (redshift of a few). [27, 28], as well as others, have shown that with a *nearly ideal CMB experiment* (in the sense that instrumental noise as well as astrophysical foregrounds are negligibly small), neutrino mass limits can be improved by a factor of approximately four by including lensing extraction in the data analysis using CMB data alone. This lensing extraction process is not perfect; a fundamental residual noise will afflict any experiment, even ideal ones. This noise will, in principle, propagate to the inferred cosmological parameters if the latter significantly depend on lensing extraction, e.g. neutrino mass, α and w. It is important to illustrate first the effect of beam systematics on lensing reconstruction. By optimally filtering the temperature and polarization we can reconstruct the lensing potential from quadratic estimators [14]. It was shown that for experiments with ten times higher sensitivity than Planck, the EB estimator yields the tightest limits on the lensing potential.

This result assumes no beam systematics which might significantly contaminate the observed B-mode.

We illustrate the effect of differential beam rotation, ellipticity and differential pointing (see [2]) on the noise of lensing reconstruction with POLARBEAR (1200 detectors), CMBPOL-A (one of two toy experiments we consider for CMBPOL; $0.22\mu K$ sensitivity and $5'$ beam) and a toy-model considered earlier by [22] which we refer to as QUIET+CLOVER in Figures 2.1, 2.2, and 2.3, respectively. These are perhaps the most pernicious systematics. Beam rotation induces cross-polarization which leaks the much larger E-mode to B-mode polarization and differential ellipticity leaks T to B. Both leak to B-mode in a way indistinguishable under rotation from a true B-mode signal. The rotation and ellipticity parameters (ε and e, respectively) we considered range from 0.01 to 0.20 (e is dimensionless and ε is given in radians). The differential pointing ρ, was set to 1% and 10% of the beamwidth while the dipole and octupole components of the scanning strategy were set to the 'worst case scenario' $f_2 = 2\pi$, i.e. the unlikely situation where all 'hits' at a given pixel take place at the same polarization angle α (again, for ideal scanning strategy $f_2 = 0$ and the *dipole* effect due to differential pointing vanishes). Note for POLARBEAR (Figure 2.1) with $\varepsilon, e = 0.2$ the lensing potential can be reconstructed up to $l \approx 200$, while with no beam rotation it can be reconstructed up to $l \approx 250$. However, with CMBPOL-A (Figure 2.2) lensing reconstruction degrades significantly in the presence of beam rotation (from good reconstruction up to l≈600 in the systematics-free case down to l≈ 250 when $\varepsilon, e = 0.2$ and $\rho = 0.5'$ (in case $f_2 = 2\pi$)). The reason for the qualitative difference is that for experiments with sensitivities comparable to PLANCK or POLARBEAR, the best estimator of the lensing potential comes from the TT, TE and EE correlations (depending on scale l) and the cross-correlations involving B-mode are only secondary in probative power (see top left panel of Fig. 2.1). Therefore, lensing reconstruction for these experiments is hardly affected by beam systematics (we ignored the negligible beam systematics' effect on temperature anisotropy and considered only those of E and B). In contrast, as can be seen from Figure 2.2, CMBPOL-A's lensing reconstruction is significantly degraded since its lensing reconstruction is dominated by the contribution of the EB estimator for all relevant multipoles (see top left panel of Fig. 2.2). The modified noise in reconstructing the lensing potential, N_l^{dd}, is consistently substituted into our Fisher matrix and Monte Carlo simulations (below, we summarize the relevant expressions of the quadratic estimators method).

Following [14] the MV noise on the lensing deflection angle reconstructed power spectrum C_l^{dd} is

$$N_{MV}^{dd} = \left[\sum_{\alpha\beta}(N^{-1})_{\alpha\beta}\right]^{-1} \tag{2.13}$$

where

$$\begin{aligned} N_{\alpha\beta}(L) &= L^{-2}A_\alpha(L)A_\beta(L)\int\frac{d^2l_1}{(2\pi)^2}F_\alpha(\mathbf{l_1},\mathbf{l_2})\left(\mathbf{F}_\beta(\mathbf{l_1},\mathbf{l_2})\right. \\ &\times\left. C_{l_1}^{x_\alpha,x_\beta}C_{l_2}^{x'_\alpha,x'_\beta}+F_\beta(\mathbf{l_2},\mathbf{l_1})\mathbf{C}_{\mathbf{l_1}}^{\mathbf{x}_\alpha,\mathbf{x}'_\beta}\mathbf{C}_{\mathbf{l_2}}^{\mathbf{x}'_\alpha,\mathbf{x}_\beta}\right) \\ A_\alpha(L) &\equiv L^2\left[\int\frac{d^2\mathbf{l_1}}{(2\pi)^2}h_\alpha(\mathbf{l_1},\mathbf{l_1})F_\alpha(\mathbf{l_1},\mathbf{l_1})\right]^{-1} \end{aligned} \tag{2.14}$$

and α stands for one of the pairings TT,TE,EE,TB and EB (BB does not participate in these combinations). The coupling takes place between different modes l_1 and l_2. When $\alpha = TT$ or EE

$$F_\alpha(\mathbf{l}_1,\mathbf{l}_2)\rightarrow\frac{h_\alpha(\mathbf{l}_1,\mathbf{l}_2)}{2C_{l_1}^{\prime xx}C_{l_2}^{\prime xx}}, \tag{2.15}$$

and when $\alpha = TB$ or EB

$$F_\alpha(\mathbf{l}_1,\mathbf{l}_2)\rightarrow\frac{h_\alpha(\mathbf{l}_1,\mathbf{l}_2)}{C_{l_1}^{\prime xx}C_{l_2}^{\prime x'x'}} \tag{2.16}$$

where C'_l are the *observed* power spectra, i.e. including lensing, main-beam dilution on small scales, and in principle - *beam systematics* (see Tables 2.1 and 2.2). The latter mainly affect the B-mode polarization, and as a result, the EB estimator. A list of $h_\alpha(\mathbf{l}_1,\mathbf{l}_2)$ can be found in [14]. We have used the publically available code employed in [28, 29][3]. The code is based on the formalism developed in [15], an extension of [14] to the full-sky, to calculate the noise level in lensing reconstruction.

---

[3] http://lpsc.in2p3.fr/perotto/

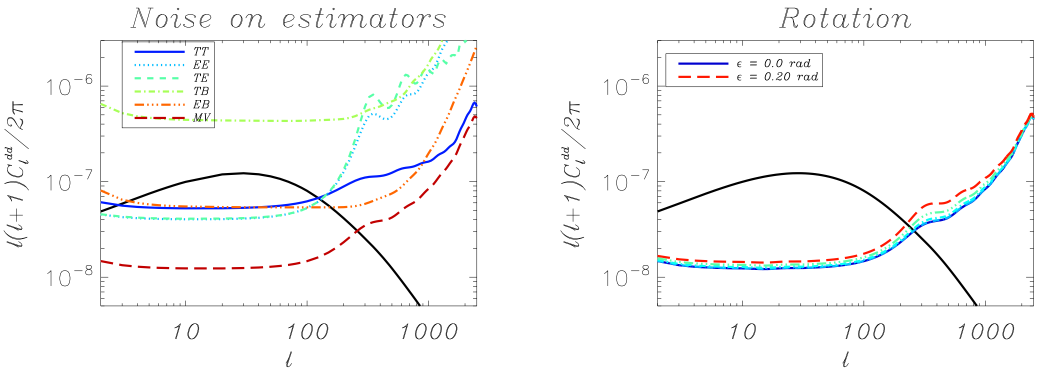

(a) N_ℓ^{dd} (b) Rotation

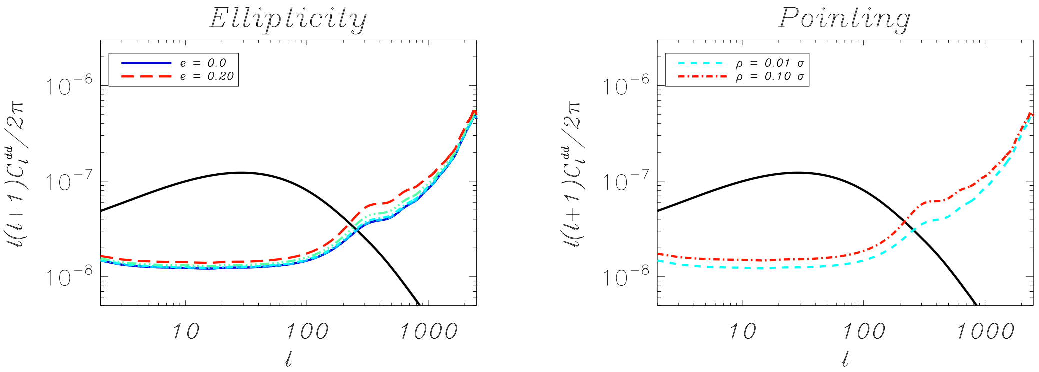

(c) Ellipticity (d) Pointing

Figure 2.1: For all planels the solid black curve is the deflection angle power spectrum C_l^{dd} caused by gravitational lensing by the LSS. a): The noise (with no systematics) in lensing-reconstruction from the different quadratic optimal filters for POLARBEAR. b): Noise in lensing reconstruction for POLARBEAR with the MV estimator including the effects of the most pernicious irreducible cross-polarization systematic: differential rotation. c): Noise in lensing reconstruction for POLARBEAR with the MV estimator including the most pernicious *irreducible* instrumental polarization systematics: differential ellipticity. d): Noise in lensing reconstruction for POLARBEAR with the MV estimator for the most pernicious *reducible* instrumental polarization systematics: differential pointing with 1% and 10% pointing errors (i.e. $\rho = 0.01\sigma$ and $\rho = 0.1\sigma$, respectively) under the 'worst case' assumption that the scanning-strategy-related function $f_2 = 2\pi$.

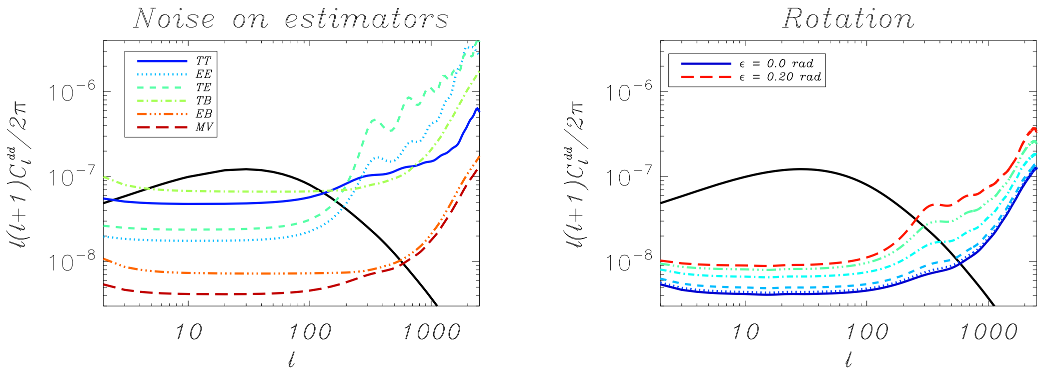

(a) N_ℓ^{dd}

(b) Rotation

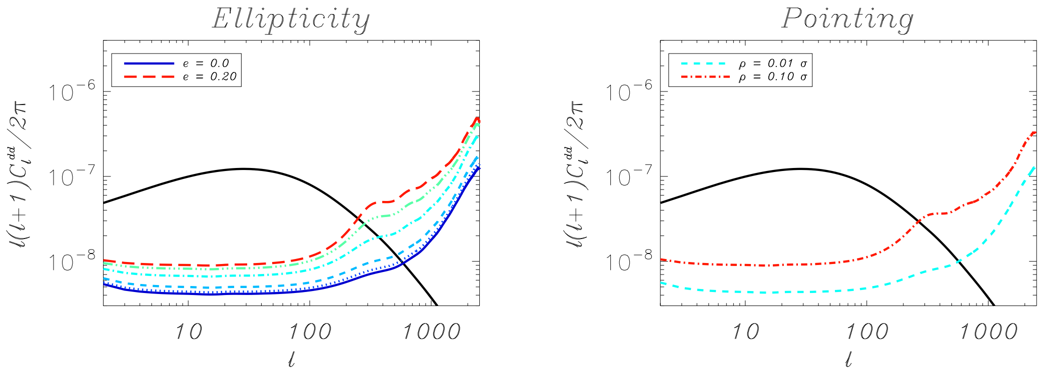

(c) Ellipticity

(d) Pointing

Figure 2.2: Lensing reconstruction with CMBPOL-A: As in Figure 2.1. For CMBPOL-A sensitivity and angular resolution, the lowest-noise estimator comes from correlations of the EB estimator. Therefore, lensing reconstruction is only mildly affected by beam systematics.

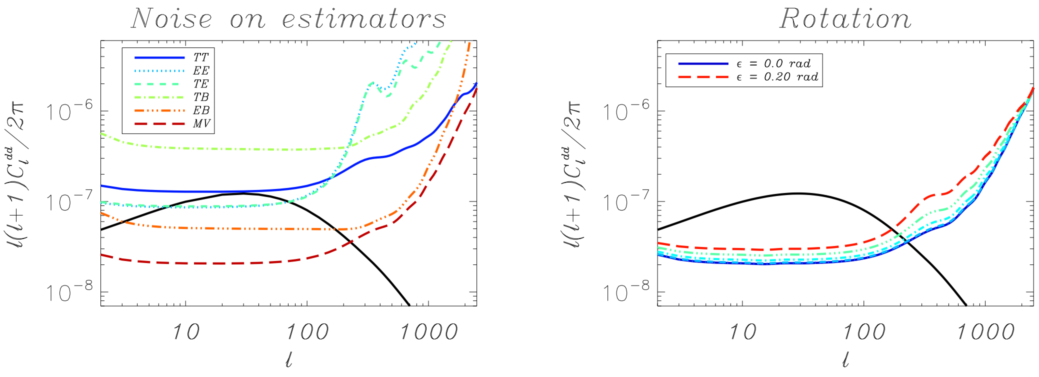

(a) N_ℓ^{dd}

(b) Rotation

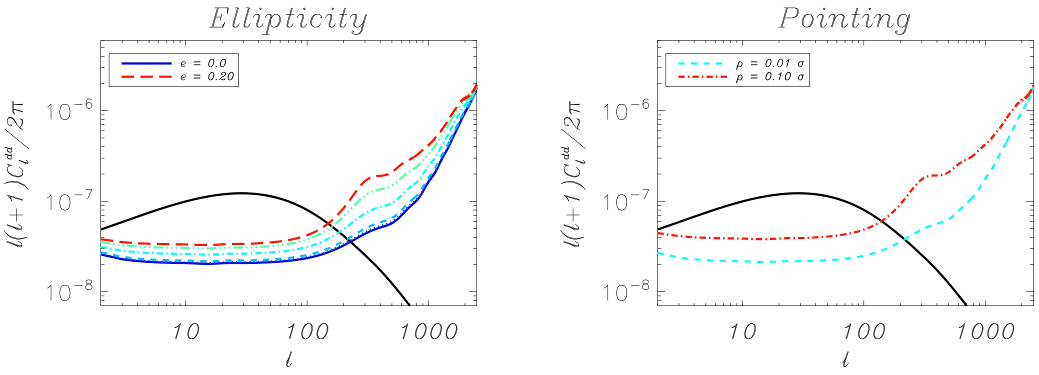

(c) Ellipticity

(d) Pointing

Figure 2.3: Lensing reconstruction with QUIET+CLOVER: As in Figure 2.1. For QUIET+CLOVER sensitivity and angular resolution, the lowest-noise estimator comes from correlations of the EB estimator. Therefore, lensing reconstruction is significantly affected by beam systematics.

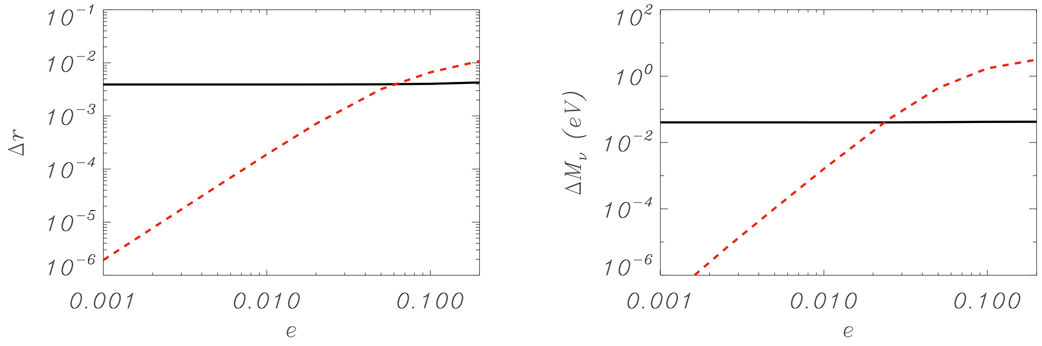

(a)

(b)

Figure 2.4: Uncertainty in the tensor-to-scalar ratio r (left) and total neutrino mass M_ν (right) due to beam ellipticity of POLARBEAR. The black solid curve is the statistical error (uncertainty) and the red dashed curve is the bias. As we vary e, the uncertainty increases by only a few percent (i.e. the width of the corresponding 1-D likelihood function does not significantly change). The bias, however, sharply rises with increasing ellipticity, i.e. the expectation value of r and M_ν significantly changes. In general, we find that beam systematics mainly bias the inferred parameters since, for large enough beam systematics parameters, the spurious polarization signal overwhelms the cosmological signal.

2.4 Error Forecast

Accounting for beam systematics in both Stokes parameters and lensing power spectra is straightforward. In addition, the instrumental noise associated with the main beam is accounted for, as is conventional, by adding an exponential noise term. Assuming gaussian white noise

$$N_l = \frac{1}{\sum_a (N_l^{aa})^{-1}} \tag{2.17}$$

where a runs over the experiment's frequency bands. The noise in channel a is (assuming a gaussian beam)

$$N_l^{aa} = (\theta_a \Delta_a)^2 e^{l(l+1)\theta_a^2/8\ln(2)}, \tag{2.18}$$

where Δ_a is the noise per pixel in μK-arcmin, θ_a is the beam width (see Table 2.3), and we assume noise from different channels is uncorrelated. The power spectrum then becomes

$$C_l^X \rightarrow C_l^X + N_l^X \tag{2.19}$$

where X is either the auto-correlations TT, EE and BB or the cross- correlations TE, TB and EB (the latter two power spectra vanish in the standard model but not in the presence of beam systematics and exotic parity-violating physics [35, 36, 37, 38] or primordial magnetic fields [39]. For the cross-correlations, the N_l^X vanish as there is no correlation between the instrumental noise of the temperature and polarization (in the absence of beam systematics).

2.4.1 Fisher-Matrix-Based Calculation

The effect of instrumental noise is simply to increase the error bars, which is evident from the Fisher matrix formalism below. The 1-σ error $\sigma(\lambda_i)$ on the cosmological parameter λ_i can be read-off from the appropriate diagonal element of the inverse Fisher matrix

$$\sigma(\lambda_i) = \sqrt{(F^{-1})_{ii}} \tag{2.20}$$

where the Fisher matrix elements are defined as

$$F_{ij} = -\Big\langle \frac{\partial^2 L}{\partial\lambda_i \partial\lambda_j} \Big\rangle, \tag{2.21}$$

L is the likelihood function, and Eq. (2.21) is evaluated at the best-fit point in parameter space. Explicitly, the Fisher matrix elements for the CMB read

$$F_{ij} = \frac{1}{2}\sum_l (2l+1) f_{\rm sky} {\rm Trace}\left[\mathbf{C}^{-1}\frac{\partial \mathbf{C}}{\partial\lambda_i}\mathbf{C}^{-1}\frac{\partial \mathbf{C}}{\partial\lambda_j}\right]. \tag{2.22}$$

The pre-factor $\frac{1}{2}(2l+1)f_{\rm sky}$ comes from the sample-variance of the multipole l with an experiment covering a fraction $f_{\rm sky}$ of the sky. The matrix $\mathbf{C}$ is

$$\mathbf{C} = \begin{pmatrix} C_l^{\prime TT} & C_l^{TE} & 0 & C_l^{Td} \\ C_l^{TE} & C_l^{\prime EE} & 0 & 0 \\ 0 & 0 & C_l^{\prime BB} & 0 \\ C_l^{Td} & 0 & 0 & C_l^{\prime dd} \end{pmatrix} \tag{2.23}$$

where the diagonal primed elements $C_l^{\prime XX} \equiv C_l^{XX} + N_l^{XX}$ and $X \in \{T, E, B, d\}$. In general, $N_l^{EE} = N_l^{BB} = 2N_l^{TT}$. Note that, except for N_l^{dd}, which is not an instrumental noise and emerges only because of the limited reconstruction of the lensing potential by the quadratic estimators of [14], the instrumental noise will increase $\mathbf{C}$, but *not* its derivatives with respect to the cosmological parameters. This will increase the error on the parameter estimation as seen from Eqs. 2.20, 2.22, and 2.23. It is merely because the instrumental noise dilutes the information below the characteristic beamwidth scale, and the error increases correspondingly. However, this *is not* necessarily the case with beam systematics since they couple to the underlying cosmological model, and therefore *do* depend on cosmological parameters. This noise due to systematics, $N_l^{\rm sys}$, contributes to both $\mathbf{C}$ *and* $\frac{\partial \mathbf{C}}{\partial\lambda_i}$ and its effect on the confidence level of parameter estimation can be, in principle, either a degradation or an improvement. This argument ignores potential systematic errors, i.e., bias (systematic shift of the average of the statistical distribution which characterizes certain cosmological parameters) of the recovered average values of the cosmological parameters. Indeed, as we show below, the main effect of beam systematics is to bias the inferred cosmological parameters, especially for large beam mismatch parameters, as naively expected (see Fig. 2.4 for a comparison between the bias and the uncertainty induced on the tensor-to-scalar ratio and neutrino masses by beam ellipticity). It is important to note that, although our focus is on beam systematics and their effect on parameter estimation, we do not include the systematics-induced C_l^{TB} and C_l^{EB} in the analysis (Eqs. 2.22, 2.23) because our main concern is how standard data analysis pipelines will be affected by beam systematics. We defer the treatment of the more general case, which includes the parity-violating terms and their effect on constraints of beyond-the-standard-model parity-violating interactions in the primordial universe, to a future work (see Chapter 3).

Given the beam systematics the bias of a parameter can be calculated with the Fisher Matrix. This has been done in [22]. The bias in a parameter λ_i, if not too large, is given by

$$\Delta\lambda_i = \langle\lambda_i^{obs}\rangle - \langle\lambda_i^{true}\rangle = \sum_j \left(\mathbf{F}^{-1}\right)_{ij} B_j \tag{2.24}$$

where the bias vector $\mathbf{B}$ can be written as

$$\mathbf{B} = \sum_l (\mathbf{C}_l^{sys})^t \mathbf{\Xi}^{-1} \frac{\partial \mathbf{C}_l^{cmb}}{\partial \lambda_j} \tag{2.25}$$

and $\Xi_{ij} = \mathrm{cov}(C_l^i, C_l^j)$ and $\mathbf{C}_l$ is a vector containing all six power spectra.

2.4.2 Monte Carlo Simulations

The Fisher matrix approach is known to provide reliable approximation to the uncertainty in case of gaussian distributions and only a lower bound for more general distributions by virtue of the Cramer-Rao theorem. It can yield poor estimates, however, in cases of large biases and parameter degeneracies. To check for such effects in our simulations we repeated the analysis with MCMC simulations which make use of the full likelihood function and not only its peak value and can therefore provide reliable estimates of parameter errors even in the presence of large biases. Our simulations illustrate that even when we consider the

Fisher-matrix-based results as a guide for choosing the beam parameters for the MCMC simulations, the resulting bias that the Monte-Carlo simulations predict can be larger than those found with the Fisher-matrix-based calculation (actually Eq. 2.24 assumes that the bias is small compared to the characteristic width of the likelihood function of the parameter in question; when this is not the case this approximation is invalid) in some cases. This important point is further elucidated in the next section. For our Monte Carlo simulations we use a modified version of CosmoMC which includes measurements of the lensing potential and its cross-correlation with the temperature anisotropy when calculating the likelihood in order to run these simulations. An eleven parameter model is used ($\Omega_b h^2$, $\Omega_{dm} h^2$, Θ, τ, $\Omega_\nu h^2$, w, n_s, n_t, α, $\log(10^{10} A_s)$, and r). We ran simulations for each of the five systematic effects with noise corresponding to POLARBEAR, CMBPOL-B and QUIET+CLOVER experiments. While running Monte Carlo simulations is much more time consuming compared to the Fisher matrix approach, the error forecasts for future experiments will ultimately have to account for a potentially significant biases of the inferred cosmological parameters.

2.5 Results

For both the Fisher and MCMC methods we consider the effect of both irreducible and reducible systematics. By ‘reducible’ we refer to systematics which depend on the coupling of an imperfect scanning strategy to the beam mismatch parameters. These can, in principle, be removed or reduced during data analysis. This includes the differential gain, differential beamwidth and first order pointing error beam systematics. By ‘irreducible’ we refer to those systematics that depend only on the beam mismatch parameters (to leading order). For instance, the differential ellipticity and second order pointing error persist even if the scanning strategy is ideal. For reducible systematics the scanning strategy is a free parameter in our analysis (under the assumption it is non-ideal, yet uniform, over the map) and we set limits on the product of the scanning strategy (encapsulated by the f_1 and f_2 parameters) and the differential gain, beamwidth and pointing, as will be described below.

To calculate the power spectra we assume the concordance cosmological model throughout; the baryon, cold dark mater, and neutrino physical energy densities in critical density units $\Omega_b h^2 = 0.021$, $\Omega_c h^2 = 0.111$, $\Omega_\nu h^2 = 0.006$. The latter is equivalent to a total neutrino mass $M_\nu = \sum_{i=1}^{3} m_{\nu,i}$ =0.56eV, slightly lower than the current limit set by a joint analysis of the WMAP data and a variety of other cosmological probes (0.66eV [40]). We assume degenerate neutrino masses, i.e. all neutrinos have the same mass, 0.19 eV, for the purpose of illustration, and we do not attempt to address here the question of what tolerance levels are required to determine the neutrino hierarchy. As was shown in [28], the prospects for determining the neutrino hierarchy from the CMB *alone*, even in the absence of systematics, are not very promising. This conclusion may change when other probes, e.g. Ly-α forest, are added to the analysis. Dark energy makes up the rest of the energy required for closure density. The Hubble constant, dark energy equation of state and helium fraction are, respectively, $H_0 = 70$ km sec^{-1}Mpc^{-1}, $w = -1$ and $Y_{He} = 0.24$. h is the Hubble constant in 100 km/sec/Mpc units. The optical depth to reionization and its redshift are $\tau_{re} = 0.073$ and $z_{re} = 12$. The normalization of the primordial power spectrum was set to $A_s = 2.4 \times 10^{-9}$ and its power law index is $n_s = 0.947$ [38].

Since the effect of beam systematics is the focus of this paper, and because these systematics are generally manifested on scales smaller than the beamwidth (except for the effects of differential gain and rotation) we concentrate on some specific cosmological parameters which will be targeted by upcoming CMB experiments. These parameters have been chosen for our analysis because we expect them to benefit from lensing extraction or simply because they are somehow associated with small angular scales and therefore are prone to systematics on sub-beam scales. We limit our analysis to the tensor-to-scalar ratio r, dark energy equation of state w, spatial curvature Ω_k, running of the scalar index α and total neutrino mass M_ν. While r is mainly constrained by the primordial B-mode signal that peaks on degree scales (and is therefore not expected to be overwhelmed by the beam systematics which peak at sub-beam scales), it is still susceptible to the tail of these systematics, extending all the way to degree scales, because of its expected small amplitude (less than $0.1\mu K$). The tensor-to-scalar ratio is also affected by differential gain and rotation which are simply rescalings of temperature anisotropy and E-mode polarization power spectra, respectively, and therefore do not necessarily peak at scales beyond the primordial signal.

The other four parameters either determine the *primordial* power spectrum $P(k)$ on small angular scales (e.g. α) or affect the lensed signal (both temperature and polarization) at late times (e.g. M_ν, Ω_k, w). Ideally, the lensing signal, which peaks at $l \approx 1000$, provides a useful handle on the neutrino mass as well as other cosmological parameters which govern the evolution of the large scale structure and gravitational potentials. However, the inherent noise in the lensing reconstruction process ([14]) which depends, among others, on the instrument specifications (instrumental noise and beamwidth), now depends on beam systematics as well. The systematics, however, depend on the cosmological parameters through temperature leakage to polarization, and as a result there is a complicated interplay between these signals and the information they provide on cosmological parameters. As our numerical calculations show, the effect on the inferred cosmological parameters stems from both the *direct effect* of the systematics on the parameters (the top-left 3×3 block of the covariance matrix, Eq. 2.23) and the *indirect effect* on the noise in the lensing reconstruction, N_l^{dd}, in cases where the MV estimator is dominated by the EB correlations (see Section 2.3).

2.5.1 Fisher Matrix Results

The Fisher information-matrix gives a first order approximation to the lower bounds on errors inferred for these parameters. However, by construction, it uses only the information from the peak of the likelihood function. Markov Chain Monte Carlo simulations are known to be superior to Fisher-matrix-based analysis in cases of strong parameter degeneracies and bias but Fisher matrix results are useful for first order approximation and provide starting values for MCMC simulations.

We follow [22] in quantifying the required tolerance on the differential gain, differential beamwidth, pointing, ellipticity and rotation. To estimate the effect of systematics and to set the systematics to a given tolerance limit one has to compare the systematics-free 1σ error in the i-th parameter (Eq. 2.20) to the error obtained in the presence of systematics. The latter has two components; the bias and the uncertainty (which depends on the curvature of the likelihood function, i.e. to what extent does the information matrix constrain the cosmological model in question). As in [22] we define

$$\begin{aligned} \delta &= \frac{\Delta\lambda_i}{\sigma_{\lambda_i}}|_{\lambda_i^0} \\ \beta &= \frac{\Delta\sigma_{\lambda_i}}{\sigma_{\lambda_i}}|_{\lambda_i^0} \end{aligned} \tag{2.26}$$

where the superscript 0 refers to values evaluated at the peak of the likelihood function, i.e. the values we assume for the underlying model, and $\Delta\lambda_i$ and $\Delta\sigma_{\lambda_i}$ are the bias (defined in Eq. 2.24) and the change in the statistical error for a given experiment and for the parameters λ_i induced by the beam systematics, respectively. As shown in [22], these two parameters depend solely on the primordial, lensing and systematics power spectra. We require both δ and β not to exceed 10% of the uncertainty without systematics. As illustrated in Fig. 2.4 for the case of tensor-to-scalar ratio and neutrino total mass, the bias exceeds the uncertainty at some value of the beam ellipticity. This is a general result; for given beam systematic and a cosmological parameter the bias becomes the dominant component of the error in parameter estimation for sufficiently large beam imperfection (ellipticity, gain, etc). This sets the limit on our five systematics parameters as demonstrated in Tables 2.4, 2.5, 2.6, 2.7, 2.8, and 2.9 for PLANCK, POLARBEAR, SPIDER, QUIET+CLOVER, CMBPOL-A and CMBPOL-B (we considered two cases which we refer to as CMBPOL-A and CMBPOL-B, the former is a high sensitivity experiment with 1000 Planck-equivalent detectors, the later is motivated by [27]) whose specifications are given in Table 2.3. For the systematics power spectra we used the expressions in Table 2.2 assuming only temperature leakage (i.e. polarization-free underlying sky) except for the effect of differential rotation where we consider mixing between the E- and B-mode. C^{TE} cannot leak to the B-mode power spectrum since it assumes negative values for certain multipole numbers and C^{E}-contribution is higher order correction to the B-mode systematics and will add only few percent at most to the induced systematics. Due to the scaling of the systematics with the beam width, this potentially negligible C^E contribution, which contaminate the B-mode polarization at second order, will result in only a few percent change to the tolerance levels for the beam parameters we consider. More specifically, Tables 2.4, 2.5, 2.6, 2.7, 2.8, and 2.9 contain the maximum differential gain, beamwidth, pointing, ellipticity and rotation, in units of $\sqrt{\frac{f_1}{2\pi}}$ of a percent, $\sqrt{\frac{f_2}{2\pi}}$ of an arc-second, a percent and a degree, respectively. As explained in Eq. 2.12 the factor 2π in the denominators is the result of our assumption that the scanning strategy is spatially uniform. All results are robust against changing the step size used. Under the assumption of uniform scanning strategy and assuming 'worst case scenario' that the quadrupole moment of the scanning strategy is maximal ($\sqrt{\frac{f_1}{2\pi}} = 1$) in case of differential gain and beamwidth and that the monopole and octupole moments are maximal ($\sqrt{\frac{f_2}{2\pi}} = 1$) these allowed values correspond directly to g and μ in (percent units) and ρ (in arcsec units), respectively. It is also apparent from the tables that better sensitivity and higher resolution experiments generally require better control of beam parameters. This is expected since our criterion is the *fixed* 10% threshold in β and δ, i.e. the systematics are not allowed to exceed the 10% (or any other reasonably chosen threshold) level in the parameter uncertainty (σ_{λ_i}) units. Higher sensitivity experiments will have smaller σ_{λ_i} in general and therefore the allowed g, μ, e, ρ and ε will be smaller. This does not imply necessarily that controlling beam systematics of higher sensitivity experiments will be more challenging since the uncertainty of beam parameters is a direct result of the S/N level with which the beam is calibrated against a point-source. Reducing the detector noise (akin to higher-sensitivity experiment) allows smaller uncertainty in beam parameters. Also, as mentioned above the 10% threshold adapted here is arbitrarily chosen and as long as we keep the systematic bias on the cosmological parameters λ_i smaller than σ_{λ_i}, e.g. even in case δ is as high as 0.2, the beam systematics will not significantly degrade the science. Therefore, even very sensitive high-resolution experiments are expected to yield good systematics control.

2.5.2 MCMC Results

This work is the first to employ Monte-Carlo simulations to assess the effect of beam systematics on parameter estimation. We first considered beam parameters which bias the tensor-to-scalar ratio by 10%, 50%, and 100% of the error (i.e. $\delta = 0.1$, 0.5 and 1.0, see Eq. 2.26) found with the Fisher matrix formalism. The limiting value of $\delta = 0.1$ was chosen for the Fisher matrix formalism so that it was small enough such that we should not be able to see a bias, which is what we want for a limit. For the MCMC simulations, we want to be able to distinctly see a bias and with $\delta = 1$ we expected to observe it. The other two values $\delta = 0.1$ and 0.5 are also reported mainly for the purpose of comparison between the naive expectations (based on Fisher matrix analysis) with the MCMC results. For these simulations we focus only on the most sensitive cosmological parameters: r, w and M_ν. We ran the MCMC analysis on the experiments POLARBEAR, CMBPOL-B, and QUIET+CLOVER.

Our results for POLARBEAR are reported in Table 2.10, for CMBPOL-B in Table 2.11, and for QUIET+CLOVER in Table 2.12. The most sensitive parameter to the beam systematics considered here turns out to be r, the tensor-to-scalar ratio as it is not constrained by the addition of the lensing power spectra. We found the bias on r can be as high as $\sim 100\%$. w and M_ν, which are mostly constrained by the larger (compared to the primordial signal from inflation) lensing signal, are changed by no more that $\sim 10\%$, itself a non-negligible bias. Even in the absence of systematics POLARBEAR and QUIET+CLOVER exhibit a small bias (approximately $\frac{1}{2}\sigma$) in w (Tables 2.10 and 2.12, respectively) towards values smaller than -1 but this situation significantly improves with CMBPOL-B. The reason is that, as is evident from our simulation, the 1-D distribution for w, while peaked at -1, is skewed towards more negative values. As the experiment sensitivity improves, such as in CMBPOL-B, this small bias becomes insignificant. Most importantly, we also found that the levels of bias (in r) caused by differential beamwidth and ellipticity exceed the bias found with the naive inclusion of the power spectrum bias in the Fisher-matrix formalism (Table 2.13). This illustrates that the simplistic approach to bias within the Fisher-matrix formalism *underestimates* the induced bias on the cosmological parameters. However, the Fisher matrix can be used, as done here, to determine the starting values for MCMC simulations. These two systematics, the differential beamwidth and ellipticity, are *second* order gradients of the underlying temperature anisotropy as opposed to the first order gradient in case of, e.g. first order pointing error effect. This implies that for given μ and e this effect steeply increases towards smaller scales. The Fisher-matrix bias calculation is based, however, on the assumption that the bias is relatively small, an assumption which certainly breaks down when high resolution experiments are considered (i.e. with SPIDER's comparatively low angular resolution, for example, we expect the tension between the Fisher-matrix-based and MCMC estimations of the bias to be smaller).

2.6 Conclusions

The purpose of this work was to illustrate the effect of beam systematics on parameter extraction from CMB observations. Beam systematics are expected to be significant especially for detecting the B-mode polarization. Ongoing and future experiments must meet very challenging requirements at the experiment design and data analysis phases to assure polarimetric fidelity. Ultimately, a major target of these experiments is the most accurate estimation of cosmological parameters, and for this end it is mandatory to assess, among other issues, the propagation of beam systematics to parameter estimation. The tolerance levels chosen in this work are somewhat arbitrary and may be changed at will, according to the goals of individual experiments, and the numerical values we quote in the tables should be viewed in this perspective.

The only similar work so far to set tolerance levels on beam mismatch in the context of parameter estimation is [22] which influenced our present work. However, we expand on this work in several ways. While [22] considered only the effect of systematics on the tensor-to-scalar ratio r, we consider a family of parameters associated with the B-mode sector: r, M_ν, α, w and Ω_k. We set all other cosmological parameters to be consistent with the WMAP values. In order to exhaust the potential of the CMB to constrain these parameters we carried out lensing extraction. In addition, we repeated the analysis for POLARBEAR, CMBPOL-B and QUIET+CLOVER with Monte Carlo simulations and found that the Fisher-Matrix approximation is, in general, inadequate for appraising the biases. We also found that high resolution experiments, such as POLARBEAR are very sensitive to bias from second order gradient effects (i.e. differential ellipticity and differential beamwidth) which is underestimated by the Fisher-matrix-based calculation, but fully accounted for with MCMC simulations. Also, unlike [22] our results are presented independently of the scanning strategy details. The only assumption we made was that the scanning strategy is spatially uniform, a condition which can be achieved with or without a HWP which samples the polarization angles in a way which is uniform; both spatially, and in terms of polarization angle. In case that this approximation fails, the more general formalism ([2]) should be used with the added complexity introduced to lensing reconstruction by the scanning-induced non-gaussianity of the systematic B-mode.

We find that parameter bias is the dominant factor and its level actually sets the upper bounds on the beam parameters appearing in Tables 2.4 through 2.9. Our results show that the most severe constraints are set on the most sensitive experiments for a given tolerance on δ and β since these quantities are experiment-dependent (Eq. 2.26) and since, in general, an experiment with higher resolution and better sensitivity will result in smaller errors σ_{λ_i}. We expect that the constraints on the systematics should be more demanding so as to realize the potential of experiments. As mentioned above, the most stringent constraints are obtained from the requirement on the bias rather than from increased parameter uncertainty. Again, for the same reason, as shown for specific examples in Fig. 2.4; the bias *always* exceeds the uncertainty for large enough systematics and this always takes place before the 10% thresholds in Eq. 2.26 are attained. The reason is that for large enough systematics the induced spurious polarization becomes comparable to, or exceeds, the underlying polarization signals, therefore biasing the deduced value. It is easy to visualize configurations in which the bias increases without bound while the ‘curvature’ of the likelihood function (i.e. the statistical error) with respect to specific cosmological parameters does not change. It is also clear from the tables that, in general, the tensor-to-scalar ratio is the most sensitive parameter, and the second most sensitive is α, the running of the scalar index (although there are some exceptions). If the tensor-to-scalar ratio is larger than the case we studied ($r = 0.01$), this conclusion may change since r is mainly affected by the overwhelming B-mode systematics on degree scales. α is predicted to vanish by the simplest models of inflation and was added to parameter space to better fit the WMAP and other cosmological data. As is well-known, information from Ly-α systems and other LSS probes can, in principle, better constrain α if their associated systematics can be controlled to a sufficiently accurate level. For these small scales the CMB is not the ideal tool to extract information and the error that beam systematics induce on α are not significant.

The upper limits we obtained in this work on the allowed range of beam mismatch parameters for given experiments and given arbitrarily-set tolerance levels on the parameter bias and uncertainty, constitute very conservative limits. It can certainly be the case that some of the systematics studied here may be fully or partially removed. This includes, in particular, the first order pointing error which couples to the dipole moment of non-ideal scanning strategies [2]. By removing this dipole during data analysis the effect due to the systematic first order pointing error (dipole) drops dramatically. We made no attempt to remove or minimize these effects in this work. Our results highlight the need for scan mitigation techniques because the coupling of several beam systematics to non-ideal scanning strategies results in systematic errors. This potential solution reduces systematics, which ultimately propagate to parameter estimation, and affect mainly the parameters considered in this work. A brute-force strategy to idealize the data could be to remove data points that contribute to higher-than-the-monopole moments in the scanning strategy. This would effectively make the scanning strategy ‘ideal’ and alleviate the effect of the *a priori* most pernicious beam systematics. This procedure ‘costs’ only a minor increase in the instrumental noise (due to throwing out a fraction of the data) but will greatly reduce the most pernicious reducible beam systematic, i.e. the first order pointing error (‘dipole’ effect). The lesson is clear:

Table 2.1: Definitions of the parameters associated with the systematic effects. Subscripts 1 and 2 refer to the first and second polarized beams of the dual beam polarization assumed in this work.

depends on beam substructure	effect	parameter	definition
No	gain	g	$g_1 - g_2$
Yes	beamwidth	μ	$\frac{\sigma_1-\sigma_2}{\sigma_1+\sigma_2}$
Yes	pointing	ρ	$\rho_1 - \rho_2$
Yes	ellipticity	e	$\frac{\sigma_x-\sigma_y}{\sigma_x+\sigma_y}$
No	rotation	ε	$\frac{1}{2}(\varepsilon_1 + \varepsilon_2)$

the rich treasures of cosmological parameters deducible from B-mode data require a combination of high polarimetric fidelity and judicious data mining. Both are eminently feasible upcoming CMB polarization experiments.

Acknowledgments

We acknowledge the use of the publically available code by Lesgourgues, Perotto, Pastor & Piat for the calculation of the noise in lensing reconstruction. We also used CAMB and CosmoMC for calculations of the Fisher matrices and the Monte Carlo simulations. We acknowledge using resources of the San Diego Supercomputing Center (SDSC). We thank Oliver Zahn for critically reading this paper and for his very useful constructive suggestions. Useful correspondence with Anthony Challinor is gratefully acknowledged. BK gratefully acknowledges support from NSF PECASE Award AST-0548262.

This chapter is a reprint of the material as it appears in Physical Review D, Vol. 79, 063008, 2009, Miller, N.J., Shimon, M., and Keating, B.G., "CMB Beam Systematics: Impact on Lensing Parameter Estimation".

Table 2.2: The scaling laws for the systematic effects to the power spectra C_l^T, C_l^{TE}, C_l^E and C_l^B assuming the underlying sky is not polarized (except for the *rotation* signal where we assume the E, and B-mode signals are present) and a general, not necessarily ideal or uniform, scanning strategy.

effect	param	ΔC_l^{TE}	ΔC_l^E	ΔC_l^B
gain	g	0	$g^2 f_1 \star C_l^T$	$g^2 f_1 \star C_l^T$
beamwidth	μ	0	$4\mu^2 (l\sigma)^4 C_l^T \star f_1$	$4\mu^2 (l\sigma)^4 C_l^T \star f_1$
pointing	ρ	$-c_\theta J_1^2(l\rho) C_l^T \star f_3$	$J_1^2(l\rho) C_l^T \star f_2$	$J_1^2(l\rho) C_l^T \star f_2$
ellipticity	e	$-I_0(z) I_1(z) c_\psi C_l^T$	$I_1^2(z) c_\psi^2 C_l^T$	$I_1^2(z) s_\psi^2 C_l^T$
rotation	ε	0	$4\varepsilon^2 C_l^B$	$4\varepsilon^2 C_l^E$

Table 2.3: Instrumental characteristics of the CMB polarimeters considered in this work: $f_{\rm sky}$ is the observed fraction of the sky, ν is the center frequency of the channels in GHz, θ_b is the FWHM (Full-Width at Half-Maximum) in arc-minutes, Δ_T is the temperature sensitivity per pixel in μK and $\Delta_E = \Delta_B$ is the polarization sensitivity. For all experiments, we assumed one year of observations. CMBPOL A & B represent toy experiments for illustration with CMBPOL-A having 1000 PLANCK detectors and PLANCK resolution and CMBPOL-B has higher resolution but $1\mu K$ noise level.

Experiment	$f_{\rm sky}$	ν	θ_b	Δ_T	Δ_E
PLANCK	0.65	30	33'	2.0	2.8
		44	24'	2.7	3.9
		70	14'	4.7	6.7
		100	9.5'	2.5	4.0
		143	7.1'	2.2	4.2
		217	5.0'	4.8	9.8
		353	5.0'	14.7	29.8
		545	5.0'	147	∞
		857	5.0'	6700	∞
POLARBEAR	0.03	90	6.7'	1.13	1.6
		150	4.0'	1.70	2.4
		220	2.7'	8.0	11.3
SPIDER	0.6	96	58'	0.46	0.65
		145	40'	0.50	0.71
		225	26'	2.22	3.14
		275	21'	5.71	8.08
QUIET+CLOVER	0.015	150	10'	0.34	0.48
CMBPOL-A	0.65	150	5'	0.22	0.32
CMBPOL-B	0.65	150	3'	1.0	1.4

Table 2.4: Systematics tolerance for PLANCK: shown are the nominal cosmological parameters we used along with the tolerance levels (as defined by the criterion that both δ and β (Eq. 2.26), should not exceed the 10% threshold).

Parameter	Nominal value	$\frac{g}{1\%}\sqrt{\frac{f_1}{2\pi}}$	$\frac{\mu}{1\%}\sqrt{\frac{f_1}{2\pi}}$	$(\frac{\rho}{1"})\sqrt{\frac{f_2}{2\pi}}$	$\frac{e}{1\%}$	ε [deg]
r	0.01	0.02	0.42	1.5	0.8	0.72
w	-1	0.33	0.38	2.5	2.4	2.86
Ω_k	0	0.37	0.44	3.0	2.6	3.72
α	0	0.67	0.33	2.2	2.1	2.23
M_ν[eV]	0.56	0.32	0.38	2.4	2.4	2.58

Table 2.5: Systematics tolerance for POLARBEAR: As in Table 2.4.

Parameter	Nominal value	$\frac{g}{1\%}\sqrt{\frac{f_1}{2\pi}}$	$\frac{\mu}{1\%}\sqrt{\frac{f_1}{2\pi}}$	$(\frac{\rho}{1"})\sqrt{\frac{f_2}{2\pi}}$	$\frac{e}{1\%}$	ε [deg]
r	0.01	0.01	0.74	0.5	1.4	0.25
w	-1	0.16	0.38	1.7	1.8	1.26
Ω_k	0	0.18	0.39	1.8	1.8	2.01
α	0	0.17	0.30	1.2	1.3	0.77
M_ν[eV]	0.56	0.15	0.42	1.9	1.8	1.06

Table 2.6: Systematics tolerance for SPIDER: As in Table 2.4.

Parameter	Nominal value	$\frac{g}{1\%}\sqrt{\frac{f_1}{2\pi}}$	$\frac{\mu}{1\%}\sqrt{\frac{f_1}{2\pi}}$	$(\frac{\rho}{1"})\sqrt{\frac{f_2}{2\pi}}$	$\frac{e}{1\%}$	ε [deg]
r	0.01	0.03	0.10	2.2	0.19	0.97
w	-1	0.13	0.31	9.2	0.47	2.86
Ω_k	0	0.10	0.57	9.9	1.75	3.43
α	0	0.19	0.12	5.9	0.55	6.88
M_ν[eV]	0.56	0.10	0.26	10.9	0.38	3.72

Table 2.7: Systematics tolerance for QUIET+CLOVER: As in Table 2.4.

Parameter	Nominal value	$\frac{g}{1\%}\sqrt{\frac{f_1}{2\pi}}$	$\frac{\mu}{1\%}\sqrt{\frac{f_1}{2\pi}}$	$(\frac{\rho}{1"})\sqrt{\frac{f_2}{2\pi}}$	$\frac{e}{1\%}$	ε [deg]
r	0.01	0.009	0.20	0.4	0.4	0.2
w	-1	0.114	0.17	3.2	0.6	0.9
Ω_k	0	0.122	0.18	3.5	0.7	1.0
α	0	0.148	0.13	1.4	0.4	0.6
M_ν[eV]	0.56	0.109	0.18	3.1	0.7	0.8

Table 2.8: Systematics tolerance for CMBPOL-A: As in Table 2.4.

Parameter	Nominal value	$\frac{g}{1\%}\sqrt{\frac{f_1}{2\pi}}$	$\frac{\mu}{1\%}\sqrt{\frac{f_1}{2\pi}}$	$(\frac{\rho}{1"})\sqrt{\frac{f_2}{2\pi}}$	$\frac{e}{1\%}$	ε [deg]
r	0.01	0.0016	0.05	0.04	0.10	0.023
w	-1	0.0259	0.19	0.4	0.28	0.773
Ω_k	0	0.0270	0.21	0.4	0.28	0.372
α	0	0.0266	0.08	0.3	0.21	0.123
M_ν[eV]	0.56	0.0251	0.18	0.4	0.28	0.401

Table 2.9: Systematics tolerance for CMBPOL-B: As in Table 2.4.

Parameter	Nominal value	$\frac{g}{1\%}\sqrt{\frac{f_1}{2\pi}}$	$\frac{\mu}{1\%}\sqrt{\frac{f_1}{2\pi}}$	$(\frac{\rho}{1"})\sqrt{\frac{f_2}{2\pi}}$	$\frac{e}{1\%}$	ε [deg]
r	0.01	0.0031	0.57	0.2	1.1	0.066
w	-1	0.0728	0.40	0.9	1.7	0.716
Ω_k	0	0.0762	0.39	0.8	1.8	0.888
α	0	0.0600	0.30	0.4	1.3	0.315
M_ν[eV]	0.56	0.0700	0.45	1.4	1.7	0.544

Table 2.10: The effect of differential gain, pointing, beamwidth, ellipticity and rotation on parameter estimation for POLARBEAR obtained with MCMC simulations. The systematic beam parameters ε, g, etc. were chosen so that δ^{Fish} (Eq.26) assumes the specified values (third column from left), i.e. the bias -to-uncertainty ratio in the tensor-to-scalar ratio r (assuming r =0.01), as obtained by the Fisher-matrix-based calculation. The values shown are the cosmological parameters recovered from the full likelihood function and their 1σ errors. The biases we obtain for differential beamwidth and ellipticity are orders of magnitude larger and are not shown here.

Parameter	no sys.	δ^{Fish}	diff. gain	diff. pointing	diff. beamwidth	diff. ellipticity	diff. rotation
r	0.0103 ± 0.0036	0.1	0.0108 ± 0.0037	0.0108 ± 0.0038	0.0109 ± 0.0036	0.0107 ± 0.0038	0.0109 ± 0.0037
		0.5	0.0123 ± 0.0038	0.0124 ± 0.0040	0.0133 ± 0.0042	0.0126 ± 0.0041	0.0122 ± 0.0049
		1.0	0.0152 ± 0.0042	0.0152 ± 0.0047	0.0205 ± 0.0058	0.0192 ± 0.0056	0.0147 ± 0.0043
w	-1.170 ± 0.328	0.1	-1.170 ± 0.328	-1.168 ± 0.325	-1.217 ± 0.328	-1.154 ± 0.334	-1.180 ± 0.335
		0.5	-1.163 $\pm$ 0.307	-1.186 ± 0.331	-1.391 ± 0.269	-1.174 ± 0.329	-1.172 ± 0.327
		1.0	-1.171 $\pm$ 0.321	-1.194 ± 0.334	-1.575 ± 0.217	-1.153 ± 0.333	-1.145 ± 0.320
M_ν[eV]	0.537 ± 0.071	0.1	0.539 ± 0.068	0.538 ± 0.070	0.558 ± 0.068	0.531 ± 0.069	0.540 ± 0.070
		0.5	0.540 ± 0.067	0.538 ± 0.073	0.661 ± 0.065	0.538 ± 0.070	0.537 ± 0.068
		1.0	0.544 ± 0.066	0.542 ± 0.074	0.924 ± 0.074	0.533 ± 0.077	0.533 ± 0.070

Table 2.11: The effect of beam systematics on parameter estimation from CMBPOL-B obtained with using MCMC simulations.

Parameter	no sys.	δ^{Fish}	diff. gain	diff. pointing	diff. beamwidth	diff. ellipticity	diff. rotation
r	0.00961 ± 0.00039	0.1	0.00964 ± 0.0040	0.00963 ± 0.0040	0.00964 ± 0.0039	0.00962 ± 0.0039	0.00963 ± 0.0040
		0.5	0.00982 ± 0.0040	0.00979 ± 0.00041	0.00983 ± 0.00040	0.00980 ± 0.00041	0.00980 ± 0.00040
		1.0	0.01004 ± 0.00041	0.01000 ± 0.00042	0.01004 ± 0.00041	0.01002 ± 0.00040	0.00990 ± 0.00040
w	-1.025 ± 0.097	0.1	-1.027 ± 0.095	-1.027 ± 0.097	-1.045 ± 0.100	-1.025 ± 0.095	-1.029 ± 0.097
		0.5	-1.027 ± 0.095	-1.028 ± 0.094	-1.152 ± 0.121	-1.021 ± 0.091	-1.032 ± 0.098
		1.0	-1.026 ± 0.094	-1.027 ± 0.097	-1.304 ± 0.149	-1.026 ± 0.096	-1.026 ± 0.093
M_ν[eV]	0.534 ± 0.014	0.1	0.534 ± 0.014	0.534 ± 0.014	0.538 ± 0.014	0.534 ± 0.014	0.535 ± 0.014
		0.5	0.535 ± 0.014	0.535 ± 0.014	0.556 ± 0.013	0.534 ± 0.014	0.535 ± 0.014
		1.0	0.535 ± 0.014	0.536 ± 0.014	0.577 ± 0.013	0.534 ± 0.014	0.535 ± 0.014

Table 2.12: The effect of beam systematics on parameter estimation from QUIET+CLOVER obtained with using MCMC simulations.

Parameter	no sys.	δ^{Fish}	diff. gain	diff. pointing	diff. beamwidth	diff. ellipticity	diff. rotation
r	0.01035 ± 0.00333	0.1	0.01076 ± 0.03221	0.01076 ± 0.00330	0.01084 ± 0.00323	0.01053 ± 0.00342	0.01046 ± 0.00301
		0.5	0.01199 ± 0.00335	0.01241 ± 0.00365	0.01287 ± 0.00384	0.01289 ± 0.00361	0.01226 ± 0.00361
		1.0	0.01445 ± 0.00358	0.01506 ± 0.00409	0.02326 ± 0.00639	0.02135 ± 0.00587	0.01448 ± 0.00386
w	-1.143 ± 0.362	0.1	-1.163 ± 0.349	-1.141 ± 0.352	-1.167 ± 0.361	-1.131 ± 0.370	-1.143 ± 0.368
		0.5	-1.123 $\pm$ 0.361	-1.109 ± 0.363	-1.228 ± 0.326	-1.131 ± 0.362	-1.121 ± 0.357
		1.0	-1.137 $\pm$ 0.356	-1.153 ± 0.362	-1.347 ± 0.322	-1.160 ± 0.364	-1.137 ± 0.362
M_ν[eV]	0.535 ± 0.109	0.1	0.536 ± 0.105	0.531 ± 0.114	0.548 ± 0.111	0.522 ± 0.112	0.532 ± 0.110
		0.5	0.526 ± 0.120	0.526 ± 0.114	0.611 ± 0.110	0.533 ± 0.124	0.530 ± 0.112
		1.0	0.528 ± 0.117	0.552 ± 0.114	0.774 ± 0.120	0.530 ± 0.123	0.532 ± 0.112

Table 2.13: The bias in the tensor-to-scalar ratio r (δ_r) obtained with MCMC for POLARBEAR, CMBPOL-B, and QUIET+CLOVER. These δ_r values were obtained by assuming each of the five systematics we considered have the values which induce a bias $\delta_r^{Fish} = 0.1$, 0.5 and 1, respectively, in the Fisher matrix analysis. This table is a compilation of the corresponding values for r reported in Tables 2.10, 2.11, and 2.12.

Experiment	Beam parameter	δ_r ($\delta_r^{Fish} = 0.1$)	δ_r ($\delta_r^{Fish} = 0.5$)	δ_r ($\delta_r^{Fish} = 1.0$)
POLARBEAR	$g\sqrt{\frac{f_1}{2\pi}}$	0.14	0.56	1.36
	$\rho\sqrt{\frac{f_2}{2\pi}}$	0.14	0.58	1.36
	$\mu\sqrt{\frac{f_1}{2\pi}}$	0.17	0.83	2.83
	e	0.11	0.64	2.47
	ε	0.17	0.53	1.23
CMBPOL-B	$g\sqrt{\frac{f_1}{2\pi}}$	0.08	0.54	1.10
	$\rho\sqrt{\frac{f_2}{2\pi}}$	0.05	0.46	1.15
	$\mu\sqrt{\frac{f_1}{2\pi}}$	0.08	0.56	1.10
	e	0.03	0.49	1.05
	ε	0.05	0.49	0.74
QUIET+CLOVER	$g\sqrt{\frac{f_1}{2\pi}}$	0.12	0.49	1.23
	$\rho\sqrt{\frac{f_2}{2\pi}}$	0.12	0.62	1.41
	$\mu\sqrt{\frac{f_1}{2\pi}}$	0.15	0.76	3.88
	e	0.06	0.76	3.30
	ε	0.04	0.57	1.24

Chapter 3

Beam Systematics and Impact of Cosmological Birefringence

3.1 Introduction

Future CMB polarimeters are poised to detect the B-mode polarization. It is expected that PLANCK will detect the lensing-induced B-mode in the near future and a host of CMB experiments are expected to detect the horizon-scale inflationary B-mode signal if the tensor-to-scalar ratio is $r \approx 0.01$. This extremely feeble signal is susceptible to a variety of foregrounds and systematics which may severely degrade the science which CMB observations could otherwise do in an ideal-world. Analytic expressions have been obtained for several types of beam systematics as well as the acceptable levels of beam uncertainties, such as differential ellipticity, gain, rotation, etc. (e.g. [20, 22, 41, 42]). We are especially concerned with those beam features whose levels and other characteristics are not precisely known (e.g., the extent to which the beam is elliptical, its gain mismatch, etc) since this cannot be remedied in the process of data analysis and will therefore add an uncertainty to the CMB power spectra. The level of allowed beam uncertainty is determined mainly by the type of science one could do with B-mode polarization; these are associated with inflation and lensing-related science such as neutrino masses, dark energy equation of state, etc. It might be possible that an actual beam calibration will result in a better calibration than the minimum requirements for the science. As it turns out, for as low a tensor-to-scalar ratio as $r = 0.01$ the most stringent experimental requirements on the allowed level of beam uncertainty come from the inflationary science. Not only will B-mode observations open a unique window to inflation and gravitational lensing, it also offers a rare opportunity to peer into two of the most fundamental underlying symmetries of physics, namely - parity and Lorentz invariance. With an horizon-scale optical path we have the longest possible leverage-arm to detect the accumulated effect of 'cosmological birefringence' (CB), a continuous rotation of the polarization plane of the electromagnetic radiation. Lorentz- and/or parity-violating terms in the electromagnetic or gravitational sectors of a hypothetical unified model of the fundamental interactions of nature may induce such a CB (e.g. [16, 43, 35, 44, 45, 46]). Searching evidence for CB in the CMB power spectra have been the objective of several recent works ([47, 36, 48, 37, 38, 49]) which analyzed the data in an ideal, systematics-free, world.

The purpose of this work is to highlight the importance of controlling beam systematics, mainly their effect on the polarization state of the CMB and in the context of CB. A tantalizing idea is to use the TB and EB cross-correlations in the CMB to detect Lorentz-symmetry breaking or parity-odd features. However, these cross-correlations are especially susceptible to even the smallest degradation in the B-mode (due to temperature leakage or beam rotation) and therefore a careful study of the implications beam systematics may have on the CB science is well motivated.

The outline of this paper is as follows. The effect of beam systematics is discussed in Section 3.2. We describe our analysis technique and results in Section 3.3 followed by a discussion in Section 3.4. We conclude in Section 3.5. Our basic calculations are supplemented with two appendices: In Appendix 3.A we estimate the resulting level of beam ellipticity assuming a standard procedure of telescope beam calibration (which determines the level of TB and EB correlations induced by beam ellipticity). Appendix 3.B is dedicated to a brief discussion of the randomness of beam-pair orientation in the focal plane and its implications on the spurious power spectra.

3.2 The Effect of Beam Systematics

No CMB observation is perfect and is always confronted, at some level, by optical beam systematics. Beam mismatch can induce temperature leakage to polarization as well as mode-mixing between the E- and B-modes ([20, 2]). Temperature leakage to polarization is considered the most pernicious systematic due to the fact that the primordial temperature anisotropy is at least an order of magnitude larger than the E-mode and two-three orders of magnitude larger than the B-mode. Therefore, even a small level of temperature leakage to polarization significantly contaminates the signal. For CB science, however, we are most concerned with cross-polarization and we open this discussion with the effect of beam rotation which mixes E and B-modes ([20, 2]). Beam rotation by an angle ε trivially biases the cosmological birefringence angle α at this level which implies that the uncertainty on the inferred α cannot be smaller than the bias induced by the uncertainty in beam orientation, ε. Threshold values for ε have been found for POLARBEAR, PLANCK and CMBPOL based on the requirement that both inflation and lensing science are not degraded above certain level in Chapter 2, which is a reproduction of [41]. However, this requirement does not necessarily protect the CB science from beam systematics.

CMB polarimeters such as PLANCK will have sufficiently high instrumental sensitivity to allow a statistically significant detection of C^{TB} (in a systematics-free world), the ‘smoking gun’ for CB. As will be shown below, PLANCK and POLARBEAR have the raw sensitivity to detect rotation angles as small as few arcminutes. Any beam rotation by a larger angle will wash out the cosmological rotation of the polarization plane if CB is small enough. In these high-sensitivity experiments high polarimetric fidelity is required.

In the following we briefly discuss what impact two other beam systematics have on CB. These two effects, due to beam ellipticity and pointing error, leak temperature to polarization and are not a simple mixing of polarization as is the case with beam rotation. Since these two offsets will have a unique spectral-dependence in Fourier space (the systematic B-mode power spectra due to differential pointing and ellipticity scale as $\propto l^2 C_l^T$ and $\propto l^4 C_l^T$, respectively) they can be *statistically* distinguished and separated (with some residual 'noise'), in principle, from CB which inherits the spectral shape of C_l^{TE} Eq. 1.9 will not be preserved in this case and we do expect that the likelihood function will change its *shape* and not be only biased. Table 3.1 summarizes the effect of differential rotation, pointing and ellipticity studied in [2] on C_l^{TB} and C_l^{EB}. It should be mentioned here that two other beam systematics considered in [2], differential gain and beamwidth, do not contribute to C_l^{TB} and C_l^{EB}. They do, however, affect C_l^{TE}, C_l^{EE} and C_l^{BB}, but since our main goal here is to test the susceptibility of C_l^{TB} and C_l^{EB} to beam systematics and the implications it has on the inferred α we do not address the effects of differential gain and beamwidth in this work.

3.3 Analysis and Results

An easy way to assess parameter uncertainty (α, the CB rotation angle in our case) is to invoke the Fisher information-matrix approach (though not in the presence of significant bias, as discussed below). The elements of the Fisher matrix are defined as follows

$$F_{ij} = \frac{1}{2}\sum_l (2l+1) f_{sky} \mathrm{Trace}[\mathbf{C}^{-1}\frac{\partial \mathbf{C}}{\partial \lambda_i}\mathbf{C}^{-1}\frac{\partial \mathbf{C}}{\partial \lambda_j}] \tag{3.1}$$

where the 4-D symmetric covariance matrix $\mathbf{C}_l$ (per each multipole l) is defined as

$$\mathbf{C}_l \equiv \begin{pmatrix} C_l^{TT} & C_l^{TE} & C_l^{TB} & C_l^{Td} \\ C_l^{TE} & C_l^{EE} & C_l^{EB} & 0 \\ C_l^{TB} & C_l^{EB} & C_l^{BB} & 0 \\ C_l^{Td} & 0 & 0 & C_l^{dd} \end{pmatrix} \tag{3.2}$$

where C_l^{dd} and C_l^{Td} refer to the power spectra associated with the lensing deflection angle [41]. The partial derivatives are taken with respect to the parameters λ_i. Here we allow nonvanishing TB and EB correlations and include lensing extraction. The dimensionality of the Fisher matrix is $N \times N$ where N is the dimension of parameter space of the cosmological model in question. The 1σ error on the parameter λ_i is given by

$$\sigma_{\lambda_i} = \sqrt{(\mathbf{F}^{-1})_{ii}}. \tag{3.3}$$

The 1σ error obtained by this procedure only sets a lower limit on the actual error. In general, when parameter degeneracy is high, as well as in the presence of significant bias, one resorts to Monte Carlo Markov Chain (MCMC) analysis [41]. The terms C_l^{TB} and C_l^{EB} drop from the matrix $\mathbf{C}$ (Eq. 3.2) in the standard model, but in general, especially here, they do not.

A small bias in a parameter λ_i compared to the statistical uncertainty, is given by

$$\Delta\lambda_i = \langle\lambda_i^{obs}\rangle - \langle\lambda_i^{true}\rangle = \sum_j \left(\mathbf{F}^{-1}\right)_{ij} B_j \tag{3.4}$$

where the bias vector $\mathbf{B}$ can be written as

$$\mathbf{B} = \sum_l (\mathbf{C}_l^{sys})^t \mathbf{\Phi}^{-1} \frac{\partial \mathbf{C}_l^{cmb}}{\partial \lambda_j}, \tag{3.5}$$

$\mathbf{\Phi}_{ij} \equiv \mathrm{cov}(C_l^i, C_l^j)$ and $\mathbf{C}_l$ is a vector containing all six power spectra [22, 41]. Our analysis includes lensing reconstruction and is essentially a generalization of [41].

As pointed above already, the underlying assumption of this work is that the primary target of upcoming CMB experiments is the inflationary B-mode; lensing-induced B-mode as well as the B-mode polarization induced by the Chern-Simons-type interaction term are only secondary. In addition, it was shown already that the inflationary signal is more prone to beam systematics than the lensing signal is and therefore it was assumed that optimizing the beam systematics to the former should be sufficient for the latter [41]. Here, we use the analytic expressions for beam systematics found in [2] to determine the resulting bias in the inferred CB for both PLANCK and POLARBEAR. Before presenting the results of our Fisher-matrix analysis it is constructive to plot the systematic C_l^{TB} and C_l^{EB}. These are shown for both PLANCK and POLARBEAR in Figure 3.1. Black (dotted), blue (dashed) and yellow (dotted-dashed) curves correspond to the systematics induced by differential pointing, ellipticity and beam-rotation, respectively (note that the effect of pointing on the EB cross-correlation is negligible and falls below the scale shown). For all the effects we assumed worst-case scanning strategy and polarimeter orientation as will be discussed below and extensively discussed in [2, 41]. Red (continuous) curves show levels of C_l^{TB} and C_l^{EB} which these experiments could have detected (obtained from the Fisher-matrix analysis) in the absence of systematics. We refer to them as 'nominal CB' detection. For comparison, the green (continuous) curve corresponds to a much larger rotation of the polarization plane that will result in C_l^{TB} and C_l^{EB} roughly three times larger than the largest systematics-induced TB and EB correlations. It is evident from the figure that realizing the nominal potential of PLANCK and POLARBEAR to detect CB via the TB and EB correlations will require a much better control of systematics than the level set by the inflationary-induced B-mode detection requirements, for example.

The results of our Fisher-matrix analysis are shown in Table 3.2. Nominal uncertainties in α (i.e. the statistical error in a systematics-free experiment) are compared with the bias induced by differential pointing and ellipticity, $\Delta\alpha$. The values for the differential pointing ρ and ellipticity e are adopted from Chapter 2, consistent with the assumption that PLANCK and POLARBEAR are optimized for inflation and lensing science. In the analysis we used all information from multipoles $l \leq 1200$. Figure 3.1 suggests that the bias decreases if l_{max} is smaller but this of course comes on the expense of statistical uncertainty. We repeated the analysis with lower l_{max} which indeed resulted in lower bias but even for l_{max} as small as 200 it was unacceptably large. The effect of beam rotation results in a pure bias in the inferred α and is therefore trivial and not included in the table. Again, we find that beam calibration levels that suffice for the inflationary and lensing science are unfortunately insufficient for the CB science and this is the main conclusion of this paper. Especially worrisome in this context are beam rotation and differential ellipticity. Both systematics are independent of the scanning strategy and therefore cannot be easily mitigated. In addition, beam rotation induces both EB and TB correlations which have the same spectral shape in multipole-space as the CB; one cannot distinguish a beam rotation from CB. While it is clear from our analysis that the allowed ellipticity based on the inflation+lensing requirements may not be sufficient for CB purposes, beam calibration in a real experiment will result in a better control of ellipticity than the minimum allowed by inflation/lensing. We show in Appendix 3.A that both PLANCK and POLARBEAR will benefit from a reasonable control of ellipticity which will allow beam ellipticities lower than the minimum required for inflationary and lensing science and will therefore result in an essentially unbiased CB detection from the E-B correlations of the CMB in case the nominal values of the respective α are considered. However, TB is still prone, even in this ideal case, to beam ellipticity. Beam rotation remains the paramount concern, and of all types of systematics we identify it as the main obstacle towards CB detection; the nominal α values are typically a factor ≈ 10 smaller than the allowed beam rotation (Table 3.2). Recently, it was shown how optimal estimators, which can filter spatially-dependent rotation, can be used to filter-out a spatially-dependent rotation due to the non-standard statistics it induces by inducing $l-l$ mode coupling [23]. However, the *constant* beam rotation we consider here cannot be distinguished from CB by this method.

The systematics induced by differential pointing depend, to first order, on the scanning strategy and for a non-ideal, yet uniform, scanning strategy we encapsulate the relevant information in the two scanning functions f_2 and f_3 ([2]) whose exact definitions are irrelevant to this discussion since we always assume the worst case scenario $f_i = 2\pi$.

The cosmological model adopted in our numerical calculations closely follows the WMAP5 results [38]; the baryon, cold dark mater, and neutrino physical energy densities in critical density units $\Omega_b h^2 = 0.021$, $\Omega_c h^2 = 0.111$, $\Omega_\nu h^2 = 0.006$. The latter is equivalent to a total neutrino mass $M_\nu = \sum_{i=1}^{3} m_{\nu,i}$ =0.56eV. Dark energy makes up the rest of the energy required for a spatially-flat universe. The Hubble constant, dark energy equation of state and helium fraction are, respectively, $H_0 = 70$ km sec^{-1}Mpc^{-1}, $w = -1$ and $Y_{He} = 0.24$. h is the Hubble constant in 100 km/sec/Mpc units. The optical depth to reionization and its redshift are $\tau_{re} = 0.073$ and $z_{re} = 12$. The normalization of the primordial power spectrum was set to $A_s = 2.4 \times 10^{-9}$ and its power law index is $n_s = 0.947$.

3.4 Discussion

CMB observations, especially those which will have the sensitivity and fidelity to detect the ‘forbidden’ power spectra C^{TB} and C^{EB}, will be able to set tight constraints on CB, a phenomena related to the bedrock of fundamental physics and its symmetries. Cosmology improves on terrestrial experiments in this context due to the long optical path lengths which enable the detection, in principle, of extremely small effects. However, since a statistically significant detection of CB heavily relies on measuring the TB and EB ‘smoking gun’ correlations, and due to the fact that these involve the sub-μK B-mode signal which is prone to numerous systematics, a credible detection of non-vanishing α should account for these possible sources of confusion. We saw that beam-rotation, differential ellipticity, as well as differential pointing, gain and beamwidth (to a lesser extent) can bias the inferred α but also change the uncertainty (in the case of differential pointing and ellipticity) due to their direct effect on the TB and EB correlations. While the differential pointing is very small due to its shallow l-dependence (compared to other systematics considered here) and the effect of beam ellipticity can be partially harnessed (Appendix 3.A to this chapter), it is the beam rotation effect which mainly contaminates CB. In particular, we have shown that CMB experiments which are optimized for inflationary and lensing science *may not* be adequate for the CB science that requires a much better control of beam rotation. The nominal α-detection with PLANCK and POLARBEAR is 3.8 and 1.1 arcminutes, respectively. Beam rotation should therefore be controlled to 0.75 and 0.21 arcminutes if a 5σ detection of CB is required. This systematic effect cannot be mitigated by scanning strategy. The effect of differential pointing (which is subdominant to the effect of differential ellipticity) can be further suppressed by scanning strategy mitigation [2]. The differential-ellipticity, together with the beam rotation effect, seem the most pernicious for TB spectra (Fig. 3.1). We consistently assumed the worst-case-scenario as we did when we employed the constraints on C^{BB} by assuming the tilt of the polarization direction to the ellipse major axis is 45° (see Chapter 2). However, an estimate of the real uncertainty on beam ellipticity (Appendix 3.A) shows that, in practice, beam ellipticity should not be a major problem to

TB measurements by PLANCK and POLARBEAR. The EB cross-correlations, however, should vanish if we take $\psi = 45^\circ = \theta$. Nevertheless, for the purpose of illustration, and in the plots only, we assumed $\psi = 22.5^\circ = \theta$ so as to maximize the EB correlations for the given beam parameters. We further explored the effect of randomness of the angle ψ in a multi-pixel elliptical-beam experiment (Appendix 3.B) and found that our worst-case-scenario is actually representative of an average multi-pixel experiment. Similar considerations were also applied to beam rotation.

3.5 Conclusion

CB is an interesting ancillary science that future CMB polarimeters will target. We considered in detail two such experiments: PLANCK and POLARBEAR. Our past experience taught us that controlling beam systematics to a sufficiently high precision as to aim at the B-mode detection (in case the tensor-to-scalar ratio is $r \approx 0.01$) will also automatically guarantee a high fidelity lensing-induced B-mode measurement. However, as we show here, this minimum requirement will in general not suffice for a credible CB detection via the "forbidden" TB and EB correlations. The likely reason for this is that while BB correlations are quadratic in the beam-imperfection parameters (e.g. $\propto e^2, \varepsilon^2$) the TB correlations are only linear in these *small* beam parameters (and the EB correlation is in general noisy). This implies that for a given ellipticity or beam rotation the fractional bias in the TB cross-correlations will be larger than the the corresponding fractional bias in the BB power spectrum by O(1/e) and O($1/\varepsilon$), respectively.

Whereas the effect of differential pointing on the TB and EB power spectra, we showed, is negligible, the effect of ellipticity is larger and can compromise the CB science if only the minimal requirement of the inflation/lensing science is satisfied. However, we demonstrate in Appendix 3.A to this chapter that in practice the expected level of ellipticity uncertainty is relatively small (if the beam is standardly calibrated against a bright point source). The most pernicious effect is due to beam rotation which precisely mimics BC, has the same l-dependence, and cannot be mitigated by idealizing the scanning strategy. Our conclusion is that while TB and EB are unique indicators for new-physics in principle, they can in practice be excited by imperfect beams and in order to realize the promising potential of the high-sensitivity and fine-resolution PLANCK and POLARBEAR at CB detection beam rotation has to be controlled to the sub-arcminute level. Unless beam rotation is controlled to the arcminute level, a conservative approach, which does not use C_l^{TB} and C_l^{EB}, may be more adequate for the CB science.

3.A Forecasted Beam Ellipticity

It is instructive to estimate the expected uncertainty of beam ellipticity which may result from a standard beam-calibration procedure with a nearly black-body point-source such as Jupiter ($T_p \approx 150K$, $\theta_p \approx 0.5$ arcmin). By Wiener filtering [42] a map of the expected signal one expects to recover the source image with a signal-to-noise level

$$\left(\frac{S}{N}\right)^2 = \int \frac{|\tilde{S}(\mathbf{l})|^2}{P(\mathbf{l})} \frac{d^2\mathbf{l}}{(2\pi)^2}. \tag{3.6}$$

where $\tilde{S}(\mathbf{l})$ is the Fourier transform of the point source and $P(l)$ is the instrumental noise, i.e. the $(S/N)^2$ is the ratio of the signal and noise power-spectra integrated over all accessible multipoles in the experiment in question. The higher S/N the smaller are the uncertainties in the recovered beam parameters. The Fourier transform of the convolved calibration source is

$$\tilde{T}_p^{\text{obs}} = \tilde{T}_p e^{-\frac{1}{2}l_x^2\sigma_x^2 - \frac{1}{2}l_y^2\sigma_y^2 - i\mathbf{l}\cdot\rho} \tag{3.7}$$

where we assume an elliptical gaussian beam with principal axes σ_x and σ_y, and pointing ρ. This results in

$$\left(\frac{S}{N}\right)^2 = \frac{2\ln(2)}{\pi(1-e^2)} \left(\frac{T_p}{\Delta_b}\right)^2 \left(\frac{\theta_p}{\theta_b}\right)^4 \eta^2 f_t \tag{3.8}$$

where η is an experiment-specific optical-efficiency parameter (≤ 1) and f_t is the fraction of observation time dedicated to beam calibration (we adopt the value 1/30). Δ_b is the instrumental temperature equivalent noise, θ_b is the beamsize and e is its ellipticity. Since the pointing merely adds a phase to the beam function it

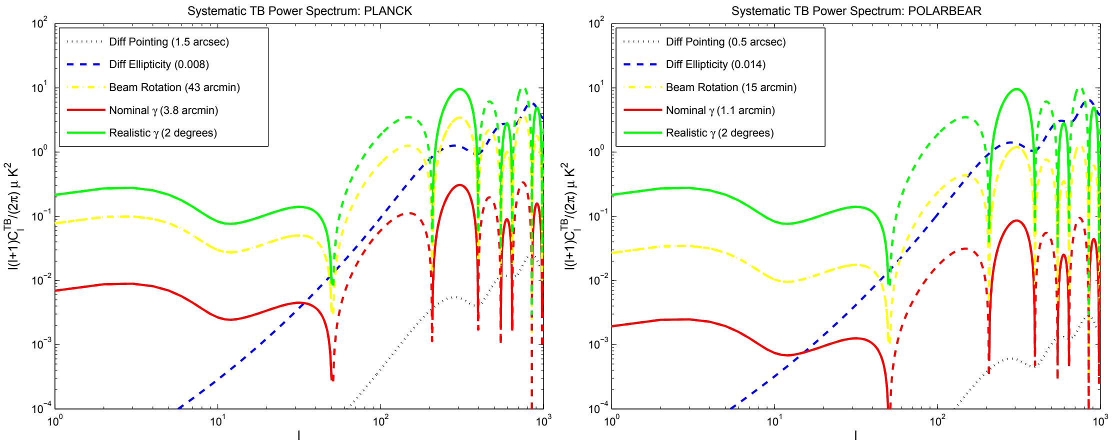

(a) Systematic TB PLANCK (b) Systematic TB POLARBEAR

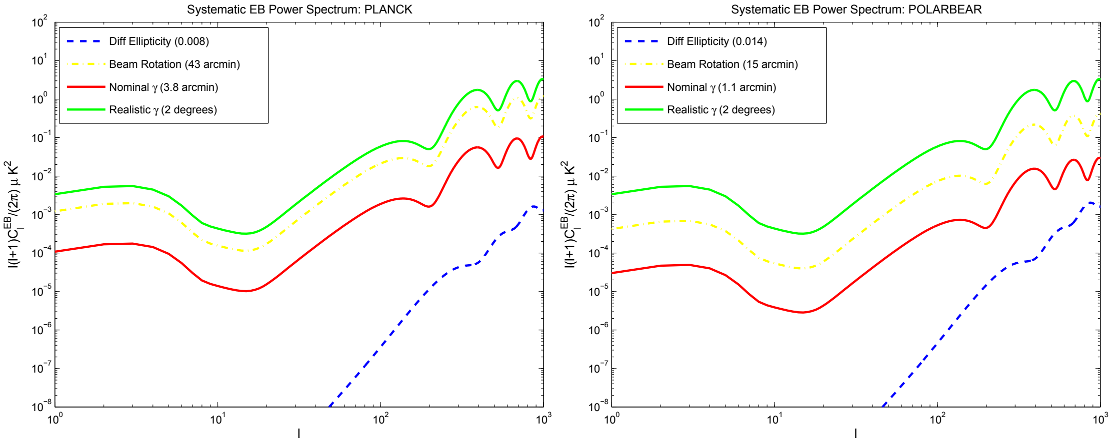

(c) Systematic EB PLANCK (d) Systematic EB POLARBEAR

Figure 3.1: TB and EB systematics compared to the nominal CB signals (i.e. those we expect to obtain in the absence of beam systematics): black (dotted), blue (dashed) and yellow (dotted-dashed) curves refer to the systematics induced by differential pointing and ellipticity and by beam rotation, respectively. Red and green (continuous) curves represent the cross-correlations in the nominal and realistic CB cases, respectively. 'Realistic' is defined as the CB that would be roughly three times larger than the largest systematic. Dashed-dotted curves represent the absolute values of negative T-B cross-correlations in certain l-ranges. All signals are calculated based on the assumption that the beam systematics of PLANCK and POLARBEAR are optimized for the detection of the inflationary signal at the $r = 0.01$ level

drops from the expression for S/N. Similarly, S/N is also independent of the beam rotation angle since temperature measurements are insensitive to ε. Calibrating the beam rotation with a polarized source will not work here since by analogy to Eq. 3.6 the rotation only adds a phase. Therefore, the following procedure, which is based on S/N considerations, will be used to determine the uncertainty of e only. To estimate these uncertainties we require that varying the beam parameters results in signal changes smaller than the noise. That is, we allow the uncertainty in the beam's ellipticity to grow from 0 until the $(S/N)^2$ changes by unity

$$(S/N)^2 \rightarrow (S/N)^2 + 1. \tag{3.9}$$

This condition readily yields the uncertainty in beam parameters

$$\Delta(e^2) = [S\eta/N]^{-2} f_t^{-1}. \tag{3.10}$$

Assuming Jupiter is a $150K$ black body with a characteristic scale of $\theta_p = 0.5'$, typical beamsizes θ_b are 5' (4') and instrumental noise Δ_b $1.7\mu K$ ($10\mu K$) for PLANCK (POLARBEAR) as well as 5% optical efficiency η we obtain the following estimates on expected uncertainty in beam ellipticity $e = 1.1 \times 10^{-3}$ (PLANCK) and $e = 1.2 \times 10^{-4}$ (POLARBEAR). Using the scaling of ellipticity-induced TB and EB correlations ($\propto e$ and $\propto e^2$, respectively), it is clear that based on this estimate beam ellipticity is unlikely to be the dominant contaminant of the EB correlations but the TB correlations will still be somewhat biased even for the optimal ellipticity we find here (O(10^{-3}) for PLANCK and O(10^{-4}) for POLARBEAR).

3.B Focal Plane Considerations

Previous works assumed, for simplicity, single-pixel experiments [20, 22, 2] (even Chapter 2). However, in practice the beam-pairs are scattered in the focal plane with different polarization orientations and other beam parameters such as gain, beamwidth, ellipticity, etc. We briefly discuss how the random orientation of beam polarization only mildly suppress spurious B-mode polarization. A schematic focal plane is depicted in Fig. 3.2. We assume all beams have the same ellipticity for the purpose of illustration but they differ by their orientations with respect to the radius-vector which connects the center of the focal plane to the beam center (denoted χ) and the polarization axis makes an angle ψ with the ellipse major axis. We further assume that the major axes of the beams are nearly orthogonal ($\chi_1 - \chi_2 \approx 90^\circ$) and similarly their respective polarization directions satisfy ($\psi_1 - \psi_2 \approx 90^\circ$), where the subscripts stand for 'beam 1' and 'beam 2' of each pair, respectively. We calculate the covariance of the individual systematic power spectra

$$cov(C_l^Y, C_{l'}^Y) \equiv \delta_{l,l'}[\langle (C_l^Y)^2\rangle - (\langle C_l^Y\rangle)^2] \tag{3.11}$$

where Y stands for either BB, TB or EB and the angular brackets denote averages over the angles ψ and χ. Since the number of pairs is finite, all the estimates we obtain here for the suppression of systematics by assuming infinitely many detector pairs constitute only upper limits. Nevertheless, we show that even if the number of detectors is assumed infinite, the gain in systematic suppression is insignificant. Taking the ratio of the covariance to the worst-case C_l^B, C_l^{TB} and C_l^{EB} ($\psi + \chi = 45^\circ$, 45° and 22.5°, respectively) it is straight forward to show that with an infinite number of pairs the systematic C_l^B, C_l^{TB} and C_l^{EB} drop to 71%, 71% and 50% of their worst-case values - an insignificantly small change to our conclusions. We can apply a similar calculation to beam rotation. in this case averaging is carried out over the angle ε (random orientations of the pair subject to the constraint that the polarization directions of the two polarimeters remain orthogonal). Here we obtain that C_l^B, C_l^{TB} and C_l^{EB} are suppressed to 35%, 71% and 50% of their worst-case values. Again, this will not quanlitatively change our conclusions.

This chapter is a reprint of the material as it appears in Physical Review D, Vol. 79, 103002, 2009, Miller, N.J., Shimon, M., and Keating B.G. "CMB Polarization Systematics due to Beam Asymmetry: Impact on Cosmological Birefringence". The dissertation author was the primary investigator and author of this paper.

Table 3.1: The contribution of the systematic effects to the power spectra C_l^{TB}, C_l^{EB} assuming the underlying sky is not polarized (except for the *rotation* signal when we assume E-, and B-mode polarization are present) and ideal sky scanning. The definitions of s_θ and s_ψ as well as f_3 can be found in [2]

effect	parameter	ΔC_l^{TB}	ΔC_l^{EB}
gain	g	0	0
monopole	μ	0	0
pointing	ρ	$\frac{1}{2}[1 + J_0(l\rho)]J_2(l\rho)s_\theta C_l^T + \frac{f_3}{2\pi}s_\theta J_1^2(l\rho)C_l^T$	$s_\theta c_\theta J_2^2(l\rho)C_l^T$
quadrupole	e	$-I_0(z)I_1(z)s_\psi C_l^T$	$I_1^2(z)s_\psi c_\psi C_l^T$
rotation	ε	$\sin(2\varepsilon)C_l^{TE}$	$\frac{1}{2}\sin(4\varepsilon)C_l^E$

Table 3.2: Estimated bias in the inferred rotation angle assuming POLARBEAR and PLANCK were optimized to detect the inflationary B-mode signal associated with r=0.01. The bias induced by differential ellipticity is much larger than the naive uncertainty, highlighting the need in careful data analysis when interpretation of polarization plane rotation is required. The relatively small bias induced by the pointing is negligible compared to the ellipticity-induced bias and this is consistent with the findings in Chapter 3 and explained by the steep l-dependence of the ellipticity systematics.

Experiment	$\sigma_\gamma^{\mathrm{nominal}}$[deg]	parameter	$\Delta\gamma$[deg]
POLARBEAR	0.0179	ρ	0.0094
		e	56.07
PLANCK	0.0641	ρ	0.0060
		e	93.9

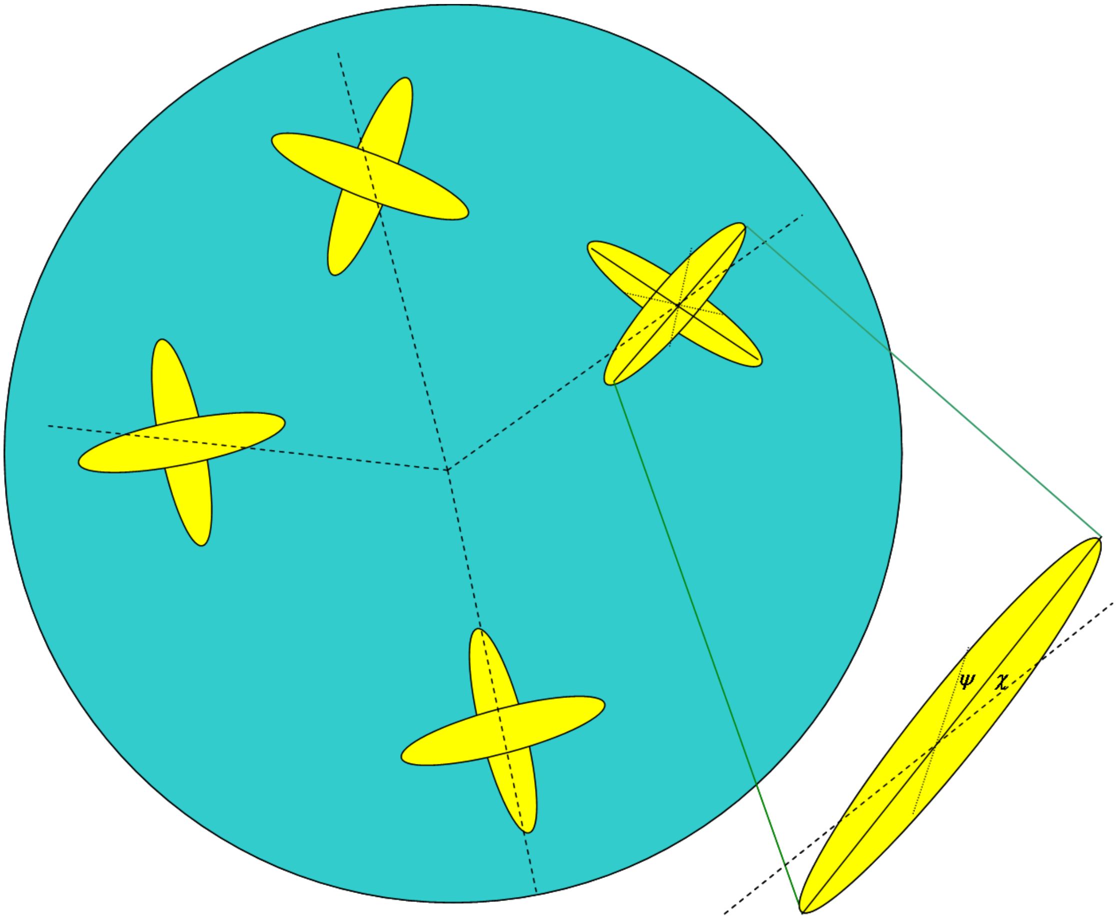

Figure 3.2: Layout of typical beam pairs in the focal plane: dashed lines represent radius-vectors from the center of the focal plane through the center of each pair. Continuous lines represent the ellipse major axes and the angle the major axis makes with the radius-vector is χ. The polarization axis (dotted line) makes an angle ψ with the major axis. In [2] and Chapter 2 it was assumed that $\chi = 0$, therefore every ψ in our analytic expressions (Table 3.1 should be replaced with $\psi + \chi$.

Chapter 4

The Temperature-Polarization Correlation and Primordial Gravitational Waves

Primordial gravitational waves (PGWs) polarize the CMB (see for example [50, 51, 52, 53, 54, 19, 55, 56, 57, 58, 59]). Current experiments are using the polarization of the CMB to search for this PGW background ([60, 61, 62]. This polarization can be used as a direct test of inflation. An alternative probe of the inflationary epoch which does not use the PGW background was studied by ([63]). This probe was used in recent analyses by the WMAP team ([64]) to provide plausibility for the inflationary paradigm. This chapter presents a test similar in spirit to that of [63].

CMB polarization can be separated into two independent components: E-mode (grad) polarization and B-mode (curl) polarization. B-mode polarization can only be generated by PGWs (see for example [55, 56, 57]), therefore most CMB polarization experiments which are searching for evidence of PGWs focus on measuring the BB power spectrum. However the TE cross correlation power spectrum offers another method to detect PGWs ([65]). The TE power spectrum is two orders of magnitude larger than the BB power spectrum and it was suggested that it may therefore be easier to detect gravitational waves in the TE power spectrum ([58, 66]).

In this chapter, we first discuss the method of detection of PGWs by measuring the TE power spectrum for low ℓ. This method, originally proposed in [58], is based on a measurement of ℓ_0, the multipole where the TE power spectrum first changes sign. Hereafter we will call this method "the zero multipole method". The TE power spectrum due to density perturbations is positive on large scales, corresponding to $\ell < \ell_0$, changes sign at $\ell = \ell_0$, and then oscillates for $\ell > \ell_0$, while for PGWs the TE power spectrum must be negative for small ℓ and then also oscillates for larger ℓ. The current best set of cosmological parameters, obtained in [67], gives, in the absence of PGWs, $\ell_0 = 53$. Therefore, the measurement of the difference between the multipole number, ℓ_0, where the TE power spectrum changes sign, and $\ell = 53$ is the way to detect PGWs. We will then consider an alternative method based on Wiener filtering, removing the contribution to the TE power spectrum due to density perturbations. Since the TE power spectrum due to PGWs is negative on large scales a test of negativity of the resulting TE power spectrum is a test of PGWs. In this chapter, we present an analysis of both of these methods, based on Monte Carlo simulations.

At the present time, the main priority and the main challenge in CMB polarization observations is the detection of the PGW background via the BB power spectrum. In connection with BB experiments, the methods based on the TE cross correlation can be considered as very useful auxiliary measurements of PGWs because systematic effects in TE measurements are not degenerate with those in BB measurements. For example, T/B leakage or even E/B leakage could swamp a detection of BB, whereas T/E leakage would be small and well controlled (see [68]). These BB systematics could falsely indicate a detection of PGWs, but measurements of the TE power spectrum provide insurance against such a spurious detection. Additionally, galactic foreground contamination affects BB and TE in different ways, which enables us to perform powerful cross-checks and subtraction of foregrounds in BB measurements.

Another advantage of TE measurements for experiments which measure a small fraction of the sky, is related to the fact that a significant contaminant to the B modes is caused by E/B mixing. This limits the power spectrum of PGWs that can be detected ([69]). The E-modes are practicly unaffected by E/B mixing so, in contrast to the BB measurements, the TE power spectrum should be nearly the same for both full and partial sky measurements.

The plan of this chapter is the following. In Section 4.1, we introduce the primordial power spectra of scalar (density) and tensor (PGW) perturbations (4.1.1). Then following [65] and [58], we explain why the sign of the TE power spectra for scalar and tensor perturbations is opposite for large scales (4.1.2). In Section 4.2, we describe in more detail the zero multipole method for the detection of PGWs. In Section 4.3, we describe the method for detection of PGWs based on Wiener filtering along with the statistical tests used and a comparison of the tests. In Section 4.4, we present results of numerical Monte Carlo simulations for two toy experiments. In the first toy experiment we neglect instrumental noise and the uncertainties are limited only by cosmic variance (4.4.1). In the second toy experiment, along with cosmic variance, we take into account instrumental noise which is comparable to real noise in current ground experiments (4.4.2). For comparison, we also present results of simulations for the two satellite experiments, WMAP (4.4.3) and Planck (4.4.5). Applying the technique to the actual WMAP 5 year data is done in Section 4.4.4. In Section 4.5, we compare the the signal-to-noise ratio of the TE measurements with those of BB measurements.

4.1 TE Cross Correlation

The power spectrum of TE correlations is determined by primordial power spectra of scalar and tensor perturbations and time evolution of these perturbations during the epoch of recombination.

4.1.1 Primordial Power Spectra

The primordial power spectra describing the initial scalar (density) perturbations (denoted by s) and tensor (PGW) perturbations (denoted by t) are (see, for example, [67])

$$\begin{aligned} P_s(k) &= A_s \left(\frac{k}{k_0}\right)^{n_s-1+\frac{1}{2}\alpha_s \log(k/k_0)} \\ P_t(k) &= A_t \left(\frac{k}{k_0}\right)^{n_t}, \end{aligned} \tag{4.1}$$

where $k_0 = 0.002$ Mpc^{-1}, this value of k_0 is obtained by fitting of CMB data ([70]). The variables n_s and n_t are the scalar and tensor spectral indices respectively. The variable α_s is the running of the scalar spectral index. In terms of A_s and A_t, the tensor-to-scalar ratio, r, is

$$r \equiv \frac{A_t}{A_s} = \frac{P_t(k_0)}{P_s(k_0)} \tag{4.2}$$

The location of ℓ_0 is determined by the parameters n_t and r. In this chaper, we do not specify particular cosmological models considering the generation of primordial spectra, $P_s(k)$ and $P_t(k)$, which means that for our purposes we consider n_s, n_t, and r as independent parameters. (This is not true if we use some particular cosmological model. For example, in standard inflation models, the parameters n_t and r are related by the consistency relation, $n_t = -r/8$ (see, for example, [64]).) In other words, we consider all parameters n_s, n_t, and r as independent except in 4.4.1 and 4.4.2, where along with model-independent we give also model-dependent constraints on r.

4.1.2 Opposite Signs of Scalar and Tensor Perturbations to TE Correlation

Taking into account that scalar and tensor perturbations are not correlated, the TE power spectrum is simply a sum of two TE power spectra for scalar and tensor perturbations correspondingly.

First, the physical motivation for the difference in the cross correlation contributions produced by scalar and tensor perturbations for small ℓ was demonstrated and physically interpreted for the cross correlation of the Stokes parameters T and Q in [65]. For scalar perturbations the Stokes parameter Q contains only

E-modes, hence the TE correlation is identical with the TQ correlation and is positive for small ℓ. As was then emphasized in [58], the sign of the TE correlation for tensor perturbations is negative for small ℓ. The simple qualitative physical interpretation of the fact that the contributions of the TE correlation are different for scalar and tensor perturbations is the following. For both scalar and tensor perturbations, the temperature fluctuations, $T(\ell)$, for small ℓ (when oscillations of $T(\ell)$ are absent) are proportional to the metric perturbations h at the moment of recombination, while the E-mode fluctuations, $E(\ell)$, are proportional to $\dot{h}$ at the moment of recombination. Hence, the TE correlation is proportional to $h\dot{h} \propto \frac{d(h^2)}{d\eta}$. Taking into account the growth of scalar perturbations and tensor perturbations decay, one can see that the contributions to the TE correlation for scalar and tensor perturbations are opposite.

To understand this in more detail, following [58], we consider the multipole expansion of the TE cross correlation with coefficients C_ℓ^{TE}. These coefficients are related to the spherical harmonic expansion coefficients of the temperature anisotropy and polarization by

$$C_\ell^{TE} = \left\langle a_{T,\ell m} a^*_{E,\ell m} \right\rangle \tag{4.3}$$

where the brackets denote averaging over all possible statistical realizations. The statistical properties of the CMB field in general, and the TE cross correlation specifically, follow from the statistical properties of the underlying scalar or tensor metric field. Assuming gaussianity together with statistical isotropy and homogeneity, the TE cross correlation takes the form

$$C_\ell^{TE} = \int \frac{dk}{k} a_{T,\ell}(k) a_{E,\ell}(k) \tag{4.4}$$

where $a_{T,\ell}(k)$ is the contribution from temperature perturbation while $a_{E,\ell}(k)$ is the contribution from E-polarization. The integration over k takes into account the contribution from all the possible wavenumbers.

It was shown in [58]

$$a_{T,\ell}(n) \sim h_k(\eta)\Big|_{\eta=\eta_{rec}} \tag{4.5}$$

$$a_{E,\ell}(n) \sim \frac{dh_k(\eta)}{d\eta}\Bigg|_{\eta=\eta_{rec}} \tag{4.6}$$

where $h_k(\eta)$ is the mode function of the metric perturbation, and η_{rec} is the conformal time at recombination. It follows that the TE correlation is approximately

$$C_\ell^{TE} \propto \int dnF(\ell,k)\left(\frac{dh_k^2(\eta)}{d\eta}\right)\Bigg|_{\eta=\eta_{rec}} \tag{4.7}$$

where $F(\ell,k)$ is a strictly positive function which peaks at $\sim \ell \approx k\left(\eta_{today}-\eta_{rec}\right)$. Heuristically, the function $F(\ell,k)$ projects the k-space onto the ℓ-space. Therefore the sign of the integral in the RHS of Eq. 4.7 evaluated at around $\ell \approx k\left(\eta_{today}-\eta_{rec}\right)$ determines the sign of C_ℓ^{TE} on large scales.

The adiabatic decrease of the gravitational wave amplitude upon entering the Hubble radius is preceded by the monotonic descrease of the gravitational wave mode function $h_k(\eta)$ as a function of η. Since $h_k(\eta)$ is decreasing the integral on the RHS of Eq. 4.7 is negative. The RHS of Eq. 4.7 is negative for $k\left(\eta_{today}-\eta_{rec}\right) < 90$ since h_k is decreasing over that range. Therefore, for $\ell < 90$ the correlation C_ℓ^{TE} must be negative. For larger ℓs, the $F(\ell,k)$ in Eq. 4.7 and, hence, the TE cross correlation power spectrum changes sign as a function of ℓ.

Thus the TE cross correlation, due to density pertrbations, must be positive at lower ℓ (as mentioned above, the TE cross correlation in absence of PGWs changes sign at $\ell_0 \approx 53$). If we were able to separate them we could use this signature for detection of PGWs. However, even without such separation the presence of PGWs manifests itself in the value of ℓ_0, which is the smallest ℓ where the total TE correlation power spectrum (scalar plus tensor) changes its sign. Thus, the sign of the TE correlation is a very prominent signature of PGWs. For this reason, in the next section, we investigate the dependance of ℓ_0 on r, n_s, and n_t.

4.2 Dependance of ℓ_0 on Parameters of PGW Power Spectrum

The method of detecting PGWs which implies a calculation of ℓ_0, where the TE power spectrum first goes to zero, will be called hereafter as the zero multipole method. We take into account uncertainties in determination of C_ℓs which are unavoidable in any experiment:

$$\begin{aligned}(\Delta C_\ell^{TE})^2 &= \frac{1}{(2\ell+1)f_{sky}}\Bigg((C_\ell^{TE})^2 + \\ &\quad (C_\ell^{TT}+N_\ell^{TT})(C_\ell^{EE}+N_\ell^{EE})\Bigg) \qquad (4.8)\end{aligned}$$

(see, for example, [8]). Even in an ideal experiment, when we neglect instrumental noise ($N_\ell = 0$) and measure the full sky ($f_{sky} = 1$), we still have uncertainties related with cosmic variance (which arises from the fact that we have only one realization of the sky in CMB measurements) (see, for example, [8]). For a more realistic experiment, we take into account noise and partial sky coverage (see Section 4.4). Over small multipole bands it is reasonable to approximate the power spectrum as linear. In the range $20 \le \ell \le 70$, it seems reasonable to use a linear approximation for $(\ell+1)C_\ell/2\pi$. It seems unlikely that in this range any deviations from a linear approximation can be larger than mentioned above uncertianties.

Plots of C_ℓ^{TE} for different values of r are shown in Fig. 4.1 plotted for $n_t = 0$. It can be seen that a linear fit to the TE power spectrum do well approximates $(\ell+1)C_\ell^{TE}/2\pi$ near ℓ_0.

Thus near ℓ_0, $(\ell+1)C_\ell^{TE}/2\pi$ can be approximated as a line with negative slope $a - b\ell$, where a and b are positive real numbers. For any set of experimental data, we can find a and b by applying a least squares fit. The values a and b corresponding to the best fit obviously can be used for prediction of $\ell_0 = a/b$. This value, ℓ_0, can then be used to constrain the parameter r under some assumptions about spectral indices n_s and n_t.

We need to investigate how ℓ_0 depends on the cosmological parameters r,

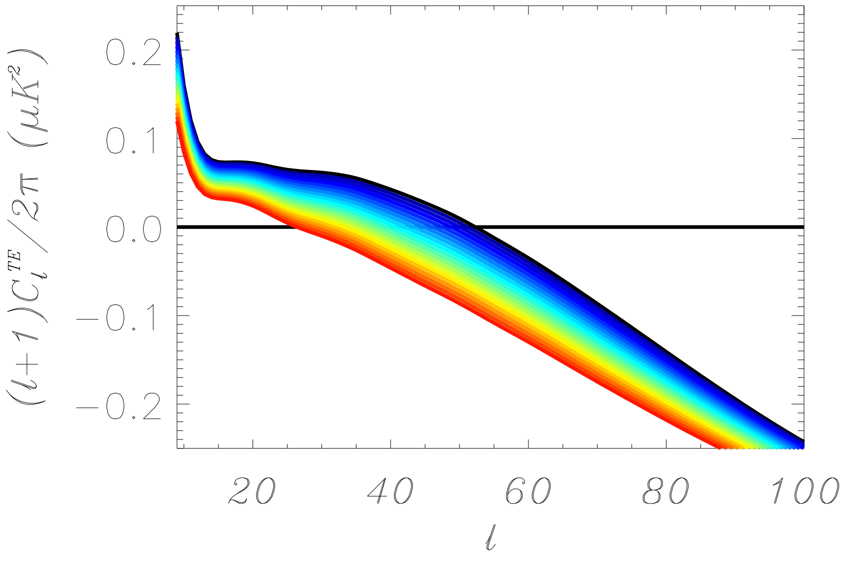

Figure 4.1: The TE cross correlation power spectrum for different values of r with $n_t = 0$. The black line is $r = 0.0$ and the red line is $r = 2.0$. Lines are given for $0 < r < 2.0$ with a spacing of $\Delta r = 0.1$.

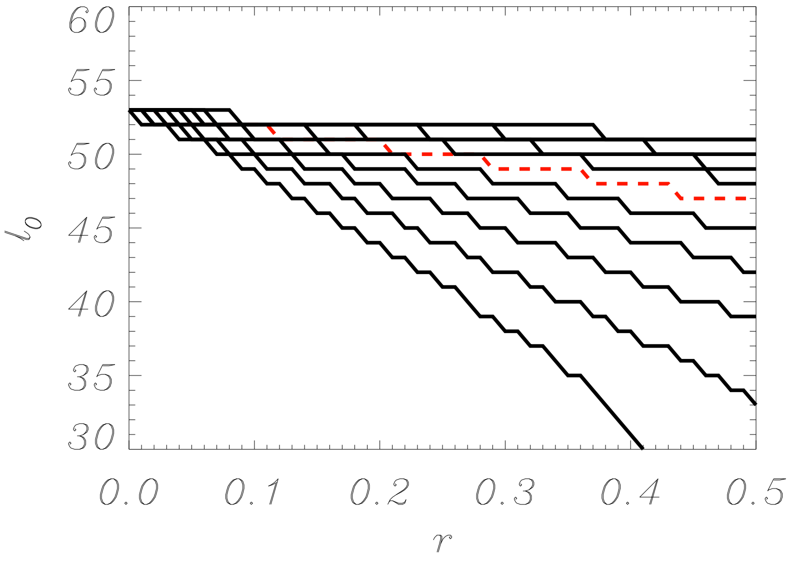

Figure 4.2: Plot of crossover multipole number ℓ_0 for different values of n_t. $n_t = -0.5$ to 0.5 with spacings of 0.1. The dashed red line correspond to $n_t = 0$.

n_t, n_s, $A_s = P_s(k_0)$, and the optical depth to reionization, τ. The value of ℓ_0 for a standard ΛCDM cosmology described in [67] as a function of n_t and r is shown in Fig. 4.2 and 4.3. All power spectra were generated with the code CAMB[1] ([71]). If $r = 0$, $\ell_0 = 53$, while if $r = 0.3$ (the WMAP3 upper limit on the tensor-to-scalar ratio) and $n_t = 0$, we find that $\ell_0 = 49$.

From Fig. 4.2 and 4.3, one can see that ℓ_0 decreases with increase of r. This effect is more pronounced for smaller n_t. For example, if $r = 0.3$, then $\ell_0 = 52$ for $n_t = +0.5$, $\ell_0 = 49$ for $n_t = 0$, and $\ell_0 = 38$ for $n_t = -0.5$. The fact that ℓ is discrete (the plots are composed of a set of step functions) puts limitations on using this method for determination of r. For example, a value of $r = 0.01$ and $r = 0$ will most likely correspond to the same ℓ_0 and therefore no matter what the sensitivity is this method cannot distinguish between absence of PGWs and PGWs corresponding to such small r. For $n_t = 0$ (the Harrison-Zel'dovich scale-free spectrum), $\delta\ell_0 = -1$ corresponds to δr of 0.08. For negative values of

---

[1] see http://camb.info on web

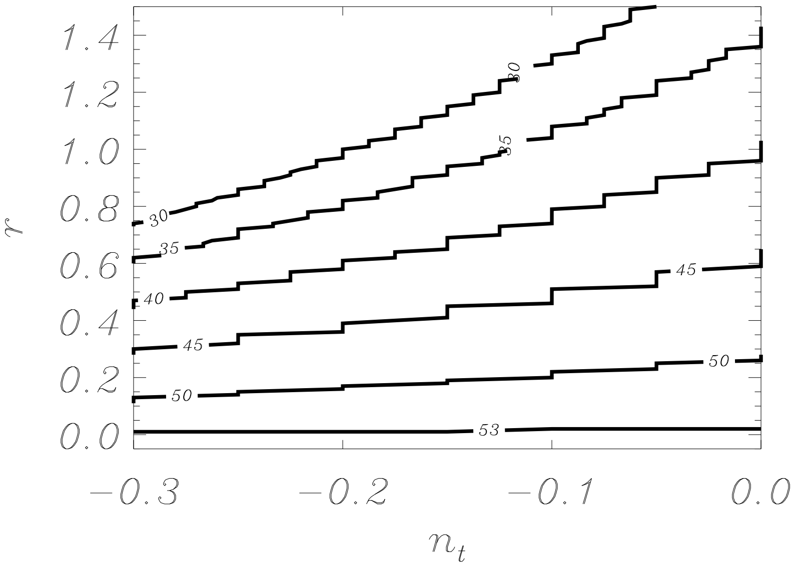

Figure 4.3: A contour plot of the values of ℓ_0 for differing values of r and n_t.

n_t, $\delta\ell_0 = -1$ corresponds to smaller δr. For $n_t = -0.5$, for example, $\delta\ell_0 = -1$ requires $\delta r \approx 0.02$.

The effect of variations of the scalar spectral index n_s on ℓ_0 is opposite: A decrease of ℓ_0 with increase of r is more pronounced for larger n_s, however we do not need to worry about it because n_s is well constrained by the observations of TT and EE power spectra (see for example [67]) along with Ly-α measurements (see for example [72]). Thus everywhere in this chapter we use $n_s = 0.95$ (the value given by WMAP3 [67]) with no running of the scalar spectral index, α_s. A change of 0.2 in the running of the scalar spectral index has no effect in the value of ℓ_0 when using $k_0 = 0.002$ Mpc^{-1}. Even if it did have an effect on the value of ℓ_0, it can be well constrained by the same observations that constrain n_s.

The value of ℓ_0 does not depend on A_s, because for fixed r, A_t must change by the same factor as A_s leaving ℓ_0 unchanged, i.e. any rescaling of the primordial power spectra does not change ℓ_0. The same thing happens when one varies the optical depth to reionization, τ. The value of ℓ_0 is in the range where the TE power spectrum for scalar and tensor perturbations depend on τ in the same way for instantaneous reionization (they are damped by the factor, $\exp(-2\tau)$, since the relevant scales are within the cosmological horizon at the time of reionization ([8]). Thus any variation of τ can be considered just as a rescaling of the TE power spectrum which leaves the value of ℓ_0 unchanged. It is possible for different reionization histories to cause a change in ℓ_0 as shown in [73], however we will assume instantaneous reionization for the purpose of this chapter.

Thus, even if we cannot separate the contributions of scalar and tensor perturbations to the TE power spectra, PGWs still leave their imprint on the value of ℓ_0. In the next section, we will consider the possibility of such separation with the help of Wiener filtering.

4.3 Wiener Filtering of the TE Cross Correlation Power Spectrum

Wiener filtering has been used often in the case of CMB data analysis. For example, it was used to combine multi-frequency data in order to remove foregrounds and extract the CMB signal from the observed data ([74, 75]). Here we examine the use of the Wiener filter to subtract the PGW signal from the total TE correlation signal. This is done because the Wiener filter reduces the contribution of noise in a total signal by comparison with an estimation of the desired noiseless signal ([76]). In our case, the signal is the one due to PGWs only, and the signal contributed by density perturbations is considered to be "noise".

The observed signal can be written as

$$C_\ell^{TE} = C_{\ell,s}^{TE} + C_{\ell,t}^{TE} = \left\langle a_{E,\ell m}^{*} a_{T,\ell m} \right\rangle \tag{4.9}$$

where s and t refer to the contributions to the power spectrum due to scalar and tensor perturbations respectively. The values $a_{E,\ell m}$ and $a_{T,\ell m}$ refer to the spherical harmonic coefficients of the temperature and polarization maps. In our application to TE correlation, we consider the Wiener filter, $W_{TE,\ell}$:

$$W_{TE,\ell} = \frac{C_{\ell,t}^{TE}}{C_{\ell}^{TE}} = -\frac{\left|C_{\ell,t}^{TE}\right|}{C_{\ell}^{TE}} \tag{4.10}$$

The filtered signal, $a'_{X,\ell m}$ (for $X = T$ and E), is obtained from the measured signal, $a_{X,\ell m}$, as

$$a'_{X,\ell m} = a_{X,\ell m} W_{TE,\ell}^{1/2} \tag{4.11}$$

In this chapter, we assume the Wiener filter is perfect, in the sense that it leaves the signal due to PGWs only. We then get, for the filtered multipoles $C_{\ell,filt}^{TE}$,

$$\begin{aligned} C_{\ell,filt}^{TE} &= \left\langle a'^{*}_{T,\ell m} a'_{E,\ell m} \right\rangle \\ &= W_{TE,\ell} C_{\ell}^{TE} = \frac{C_{\ell,t}^{TE}}{C_{\ell}^{TE}} C_{\ell}^{TE} = C_{\ell,t}^{TE} \end{aligned} \tag{4.12}$$

In practice this is not true, because we are trying to determine $C_{\ell,t}^{TE}$, which is not known in advance. Nevertheless, the assumption that the Wiener filter is perfect is good as a first approximation and illustrates the detectability of PGWs with the help of TE correlation measurements.

The filtering can reduce the measured signal to the desired signal, but, since we are trying to remove the density perturbations and not the actual noise, we can not reduce the measurement uncertainties. These uncertainties in C_{ℓ}^{TE} are then entirely determined by the noise in the original signal.

We have shown that the TE power spectrum due to PGWs is negative on large scales, hence a test determining whether the Wiener filtered power spectrum is negative or not is a probe of PGWs.

There are three different statistical tests we use to see if we can measure a negative TE power spectrum. The first test is a Monte Carlo simulation to determine signal-to-noise ratio, S/N (Section 4.3.1). The other two tests are standard non-parametric statistical tests: the sign test (Section 4.3.2) and the Wilcoxon rank sum test ([77]) (Section 4.3.3).

For all of our tests, we calculate a random variable. If the data satisfies the hypothesis that $r = 0$, we can calculate the mean and uncertainty in the variables.

If we make one realization of data, the random variable is determined from its distribution. Because we are not using any real observational data, we must run a Monte Carlo simulation to reduce the risk of randomly getting a value for the variable taken from the outlying area of its distribution. To do this, the filtered multipoles, $C_{\ell,filt}^{TE}$, are randomly chosen from a gaussian distribution with mean $C_{\ell,t}^{TE}$ and standard deviation ΔC_{ℓ}^{TE} where

$$\begin{aligned}(\Delta C_{\ell}^{TE})^2 &= \frac{1}{(2\ell+1)f_{sky}}\Bigg((C_{\ell}^{TE})^2 + \\ &\qquad (C_{\ell}^{TT}+N_{\ell}^{TT})(C_{\ell}^{EE}+N_{\ell}^{EE})\Bigg) \qquad (4.13)\end{aligned}$$

(see, for example, [8]), the variable f_{sky} refers to the fraction of the sky covered by observations and N_{ℓ} is the effective power spectrum of the instrumental noise (see [8] for details on how N_{ℓ} is related to actual instrumental noise).

Our determination of $C_{\ell,t}^{TE}$ is dependent on ℓ. However, for two of our tests we ignore the value of ℓ in the calculation of the random variable. We assume that the calculated random variable is gaussian. In order for this to work, the random variable must be calculated from gaussian variables. The errors on the multipoles for the "ideal" toy experiment are large enough so that we can assume the multipoles are taken from a single distribution and not from a distribution that depends on ℓ.

4.3.1 Monte Carlo S/N Test

For this test, the random variable we calculate, S/N, is defined as

$$S/N = \sum_{\ell=2}^{53} \frac{C_{\ell,t}^{TE}}{\Delta C_{\ell}^{TE}}. \qquad (4.14)$$

The reason why the sum in this equation is taken in the range $2 < \ell < 53$ is because only in this range $sgn(C_{\ell}^{TE}(\text{scalar})) = -sgn(C_{\ell}^{TE}(\text{tensor}))$. In other words, if we include higher multipoles we confront with a danger of a false detection, because the total TE power spectrum is negative for $\ell > 53$.

The value of S/N is gaussian distributed because it is a sum of many modes of squares of gaussian distributed values, $C_\ell = a^2_{\ell,m}$. We approximate each C_ℓ^{TE} as being gaussian distributed for the purpose of this chapter. For each set of parameters we run this simulation one million times to determine the mean, $\langle S/N \rangle$, and standard deviation, $\sigma_{S/N}$. The mean of this distribution is determined by the preassumed value of r, while the standard deviation is determined by parameters of the experiment and gives the confidence level of detection. We run such Monte Carlo simulations for different values of r to determine in what range of r we can detect PGWs. When then using real observational data, we can compare the actual value of S/N with the results of Monte Carlo simulations to infer the likelihood, as function of r, which determines the probability that $r \neq 0$, or that PGWs exist at detectable levels.

4.3.2 Sign Test

The sign test is a test of compatability of observational data with the hypothesis that $r = 0$. If we do have $r = 0$, then $C_{\ell,filt}^{TE}$ will be equally distributed around zero. Application of this test to the filtered data is very simple. In practice, all observational data are distributed between several bins and the averaging of the signal is produced in each bin separately. Let N_{bins} be the number of such bins. The sign test actually gives the probability that in N_- bins the average is negative and in $N_+ = N_{bins} - N_-$ it is positive, if $r = 0$. This probability, P, is given by the binomial distribution

$$P(N_+) = \left(\begin{array}{c} N_{bins} \\ N_+ \end{array} \right) 0.5^{N_{bins}} = \frac{N_{bins}!}{N_+! N_-!} 0.5^{N_{bins}} \tag{4.15}$$

The probability that the hypothesis $r = 0$ is wrong is

$$P(r \neq 0) \approx 1 - 2 \sum_{i=0}^{N_+} P(i) \tag{4.16}$$

The value $\sum_{i=0}^{N_+} P(i)$ is the probability that we would get $\leq N_+$ positive values given $r = 0$. This is the same as the probability of getting $\leq N_+$ negative values given $r = 0$. Therefore our confidence that $r \neq 0$ is just 100% minus the sum of the probabilities describe above (the probability that the N_+ is closer to the mean, $N_{bins}/2$, if $r = 0$). This equation only makes sense if $N_+ < N_{bins}/2$, since that is required for $r > 0$. If $N_+ > N_{bins}/2$, that would imply $r < 0$, which is not physical. We would have to interpret the result as a random realization of $r \geq 0$, with the most likely result of $r = 0$. Therefore we would not be able to say $r \neq 0$ with any confidence.

Let us consider the following example: we put all measurements of C_ℓ^{TE} into 11 bins and in three of them the average is positive. In this example, the probability that the hypothesis $r = 0$ is wrong is equal to 89%.

One possible drawback of this method is that it does not take into account any measure of the signal-to-noise ratio of individual measurements. As we show in Section 4.3.4, it is possible to have two completely different sets of data with the same probability of having $r = 0$. This test is also unable to make any prediction as to the value of r, only that it differs from zero.

4.3.3 Wilcoxon Rank Sum Test

This statistical test deals with two sets of data. The first set of data is taken from a real experiment which measures C_ℓ^{TE} with some unknown r. The second set of data is generated by Monte Carlo simulations (see Section 4.3.1) with $r = 0$. The objective of the Wilcoxon rank sum test is to give the probability that the hypothesis $r = 0$ is wrong ([77]).

First, we choose some random variable U, whose probability distribution is known if $r = 0$. For that, let us combine all data from first set with n_1 multipoles and second set with n_2 multipoles into one large data set, which obviously contains $n_1 + n_2$ multipoles. Then, we rank all multipoles in the large data set from 1 to $n_1 + n_2$ according to their amplitude (rank 1 for the smallest and rank $n_1 + n_2$ for the largest). Now, the variables R_1 and R_2 are defined as the sum of the ranks for the first original data set and the second original data set, correspondingly. Finally, the variable U, is

$$
\begin{aligned}
U &= \min(U_1, U_2), \text{ where} \\
U_i &= R_i - n_i(n_i+1)/2, \qquad i = 1,2 \qquad (4.17)
\end{aligned}
$$

If all multipoles of the first data set are larger than all multipoles of the second data set, then $U_1 = n_1 n_2$ and $U_2 = 0$. It is not difficult to show that $U_1 + U_2 = n_1 n_2$. If both sets of measurements have no evidence for PGWs, $\langle U_1 \rangle = \langle U_2 \rangle$. It is also simple to see that $U_1 + U_2 = n_1 n_2$.

It is important to emphasize that the ranks of multipoles are random variables because all multipoles themselves are random variables, hence U_1, U_2, and U are random variables. If n_1+n_2 is large, the distribution of U can be approximated as a gaussian with a known mean and standard deviation. In this approximation we have

$$
\begin{aligned}
m_U &= n_1 n_2/2 \qquad (4.18) \\
\sigma_U &= \sqrt{\frac{n_1 n_2 (n_1 + n_2 + 1)}{12}} \qquad (4.19)
\end{aligned}
$$

In some cases, instead of U, the variables R_1 or R_2 are used. The reason U is used here is because m_U is symmetric in the data sets. If $r = 0$ in both sets of data, then the distributions of U_1 and U_2 are the same, no matter what n_1 and n_2 are. The distributions of R_1 and R_2 would be the same only if $n_1 = n_2$. The probability that the first data set corresponds to $r \neq 0$ obtained from the test in which R_1 or R_2 is used is the same as if U is used.

Since this test requires Monte Carlo simulations for the second set of data, we ran this test many times for many different data sets to get an accurate mean value for U.

To reject the hypothesis $r = 0$ means to detect PGWs. Using the Wilcoxon rank sum test the allowable value of r is determined, if instead of comparing with simulated data with $r = 0$, we compare with simulated data with $r = r_0 \neq 0$. In order to get a range of allowable values for r, we need to run multiple Monte Carlo simulations with multiple values for r_0. This is where the assumption that the $C_{\ell,t}^{TE}$

are from a random distribution that is independent of ℓ is used. This implies that the ranks are random variables. If the errors on the $C_{\ell,t}^{TE}$ are small enough, then the ranks will be predetermined. Therefore, our assumption about the distribution of U will not be true and the test would have to be modified. Fortunately, this is not the case for even an experiment only limited by cosmic variance.

To illustrate how this test works, let us consider the following example. Assume there are 4 multipoles in the first set of data and consider that $r = 0.3$ is the correct value. There are also 4 multipoles in the second set of data (which for sure corresponds to $r = 0$). All quantities below are expressed in μK^2. The value for the first data set are $C_{10}^{TE} = -0.005$, $C_{20}^{TE} = 0.02$, $C_{30}^{TE} = -0.015$, and $C_{40}^{TE} = -0.01$. The values for the second data set are $C_{10}^{TE} = 0.03$, $C_{20}^{TE} = 0.003$, $C_{30}^{TE} = -0.02$, and $C_{40}^{TE} = -0.003$. A ranking of multipoles gives the ordering from lowest to highest, with 1 referring to the first data set and 2 referring to the second data set, as 21112212. This results in $R_1 = 2 + 3 + 4 + 7 = 16$, $U_1 = 16 - 10 = 6$, and $U_2 = 16 - 6 = 10$. Therefore $U = \min\{10, 6\} = 6$. For $n_1 = n_2 = 4$, to reject the hypothesis that $r = 0$ at 95% confidence level, U_1 should be less than one (see, for example, [78]). In this example, since $U_1 = 6 > 1$, the first set of data cannot be considered as a detection of PGWs.

4.3.4 Comparison of Tests

The S/N test is greatly affected by outlying measurements. A measurement of one large negative multipole could falsely imply a detection. Both the sign test and the Wilcoxon rank sum test are not affected by individual outlying measurements. In the sign test, the value of individual measurements is irrelevant, because the test is sensitive only to the sign of individual measurements. The Wilcoxon rank sum test is affected by outliers, but considerably less than the S/N test. If the outlier is larger (or smaller) than every other multipole, its rank does not depend on its particular value.

If we have two completely different sets of data, the main disadvantage of the sign test, as mentioned in Section 4.3.2, is that it could give the same result, while for the two other tests the chance to obtain the same value of r is negligible.

For example, one set of data, consisting of 4 small negative multipoles and 4 large positive multipoles, gives the same result as another set of data, consisting of 4 large negative multipoles and 4 small positive multipoles. The S/N test gives two very different values of S/N for these two sets of data. We can also use the Wilcoxon rank sum test to compare these two sets of data. In this case $U = 16 = \frac{1}{2}m_U$, which corresponds to a confidence level of hypothesis that $r = 0$ of less than 10%.

With observational data, the sign test can be applied and does not require any Monte Carlo simulations (which could be considered as an advantage of this test). The S/N test requires Monte Carlo simulations, but only for the distribution of the random variable S/N. The Wilcoxon rank sum test requires large Monte Carlo simulations and combines the data sets generated by these simulations with observational data. In other words, Monte Carlo simulations are absolutely necessary after obtaining observational data, which may be considered a disadvantage of this test. Thus, each of the three tests has advantages and disadvantages, suggesting that the best way to work out observational data is to apply all these three tests.

4.4 Discussion and Results

[58] used equal amplitudes of scalar and tensor perturbations to sharpen the discussion in their plots. They defined the tensor-to-scalar ratio, R, as the ratio of the temperature quadrupoles, $R \equiv C_{2,t}^{TT}/C_{2,s}^{TT}$ and set $R = 1$. Using standard WMAP3 cosmological parameters ([67]), the definition of tensor-to-scalar ratio, r, used in this chapter is approximately twice as large as their definition of R. The exact relationship between r and R will depend on the cosmological parameters used. This means that $R = 1$ is equivalent to $r \approx 2$, which has currently been strongly ruled out by WMAP in combination with previous experiments ([67]). We need to see if this method can detect a value of r that is currently within the limits. We assume that there is no foreground contamination. In reality foregrounds affect the measured location of ℓ_0 (we will consider the effects of foregrounds on ℓ_0 elsewhere). For the experiments that do not observe the full sky, correlations

between multipoles must be taken into account. The multipoles are binned together of such width that the correlations between the bins are sufficiently small.

Two different toy experiments, along with the two satellite experiments WMAP and Planck, are considered to constrain r. The first toy experiment is a full sky experiement. It is idealized in two aspects. The first idealization is that we can take measurements over the full sky while the second idealization is that we assume there is no detector noise. The only uncertainty is due to cosmic variance. Such experiment represents the best limit to which the gravitational waves can be detected by the CMB TE correlation. This toy experiment is close to a space-based experiment with access to the full sky. It is similar to what the Beyond Einstein inflation probe would be able to detect. This toy experiment will be hereafter referred to as the ideal experiment. The second toy experiment is a more realistic one. In this experiment, measurements are on 3% of the sky, the frequency is 100 GHz, and the duration of the experiment is 3 years. The noise in each detector of the 50 polarization sensitive bolometer pairs can be described by their noise equivalent temperature (NET) of 450 $\mu K\sqrt{s}$. The detectors' beam profile is assumed to be gaussian and and it is described by the width at half of the maximum sensitivity, abbreviated as FWHM of 0.85°.

This second toy experiment is similar to current ground-based experiments and the constraints from this experiment represent those that can and will be obtained in the next several years. This will be referred to as the realistic experiment.

The predicted errors for Planck are based on using the 100 GHz, 143 GHz, and 217 GHz channel in the High Frequency Instrument (HFI). The numbers are gotten from the Planck science case, the "bluebook"[2]. The WMAP noise was obtained by 3 years of observations of the Q-band, V-band, and W-band detectors.

4.4.1 Ideal Experiment

A plot of TE for $r = 0.3$ and $n_t = 0.0$ with error bars for ℓ binned in bins of width $\Delta\ell = 10$ is shown in Fig. 4.4. This figure separately shows the contribution to the TE mode of density perturbations, contribution of PGWs with $r = 0.3$,

---

[2] http://www.rssd.esa.int/index.php?project=Planck

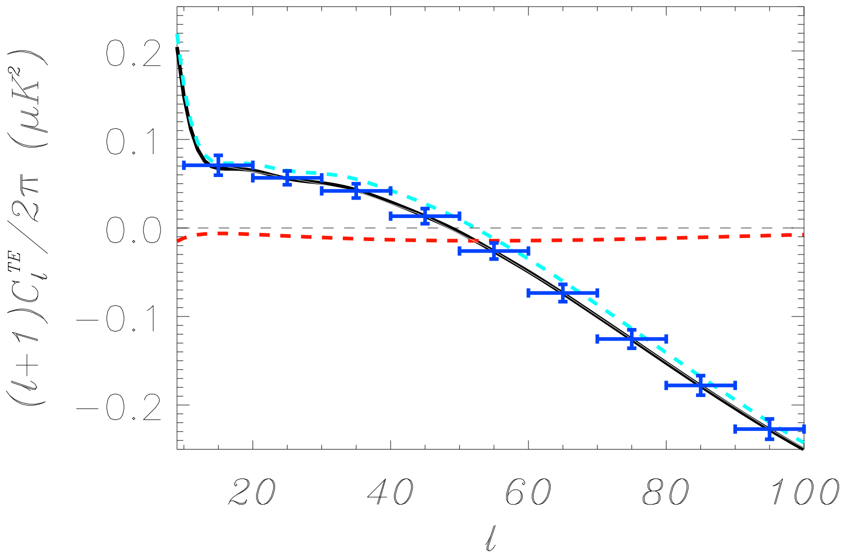

Figure 4.4: The black line is the total TE mode with a $r = 0.3$. The red line is the contribution from PGWs only while the light blue line is the contribution from the density perturbations. Blue is the error bars for the ideal experiment binned in intervals of $\Delta\ell = 10$.

when the TE power spectrum due to density perturbations is approximately five times larger than the power spectrum due to PGWs at $\ell < \ell_0$.

The Monte Carlo simulation for the calculation of ℓ_0, with an input model of $r = 0.3$ and $n_t = 0$, results in the value of $\ell_0 \approx 49$ with an uncertainty of $\Delta\ell_0 \approx 1.3$. A contour plot of the limits on the resulting measurement of r is shown in Fig. 4.5. The white is the allowed region for r and n_t that falls within the 1σ errors of ℓ_0. The black is the region forbidden with 68% confidence. If $n_t = 0$, then we measure $r \approx 0.3 \pm 0.1$. If we consider the inflationary consistency relation, $n_t = -r/8$ ([64]), we then get the constraint $r = 0.3^{+0.09}_{-0.1}$. The uncertainty is smaller, but not by much. We predict a 3σ detection of PGWs by the zero multipole method.

The detectability of ℓ_0 using the ideal experiment is shown in Fig. 4.6. For $n_t = 0$ the effective number of σ detection is $\sigma \approx 10r$. We make this approximation by determining the detectability for several values of r and then approximating a

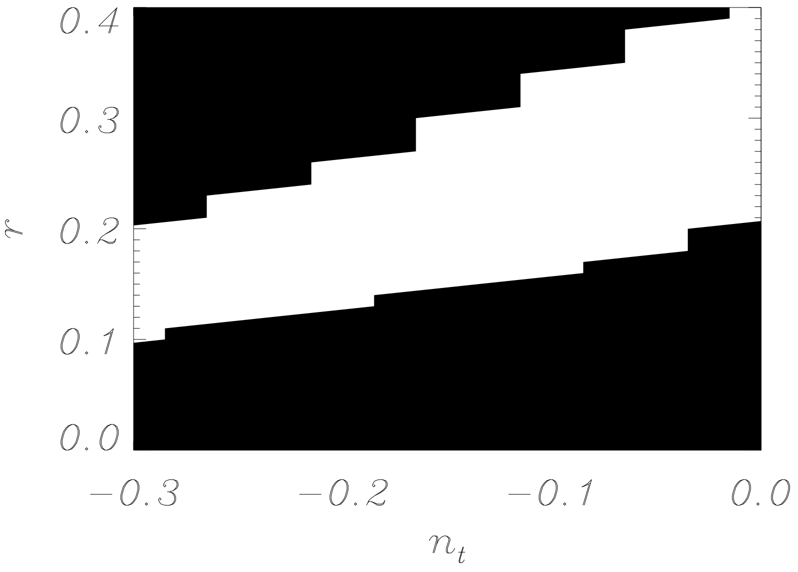

Figure 4.5: This is a plot of the allowed r and n_t for the 1σ region of ℓ_0 for the ideal experiment. The white is the 1σ region while the black is the forbidden region

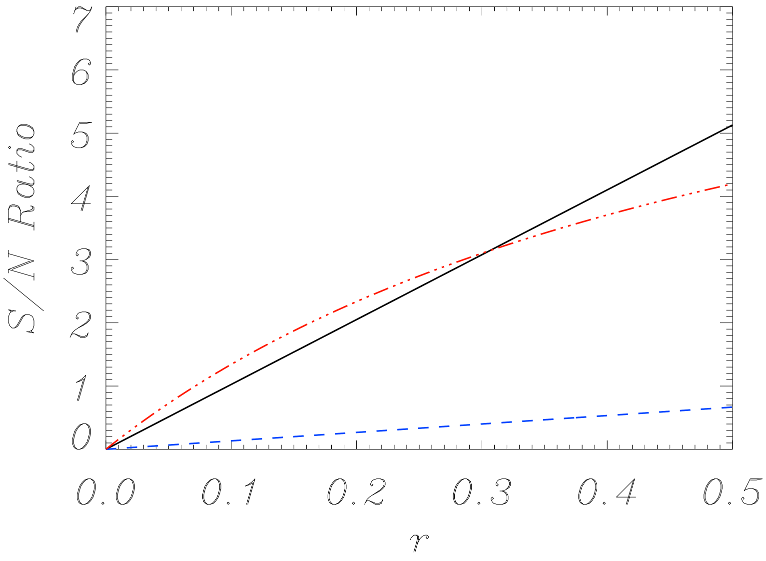

Figure 4.6: The signal-to-noise ratio for the zero multipole method are shown as the solid black, for ideal experiment, and dashed blue, for realistic experiment, lines. The signal-to-noise ratio for realistic measurements of the BB power spectrum is shown as the dash-dot red curve. For all curves $n_t = 0$.

line. For comparison the results are also shown for the zero-multipole method with the realistic experiment and for measurements of the BB power spectrum with the realistic experiment described above. We assume we can make measurements over a range of 60 multipoles for BB measurements.

The Monte Carlo simulation for the Wiener filtering gives an average of 19 measured TE power spectrum multipoles greater than zero out of a total of 52 independent multipoles. If the null hypothesis was true, the sign test would indicate there is a 3.5% chance of measuring ≤ 19 positive multipoles. This is equivalent to a $\approx 1.8\sigma$ detection. A plot of the distribution of the number of positive multipoles is shown in the upper panel plot of Fig. 4.7. There is an 81% chance for the observed N_+ to give a 1σ detection of PGWs.

The S/N test gives a mean value of $S/N = -17.1$ and standard deviation of 7.21. The upper left panel in Fig. 4.8 shows the distribution of the S/N values

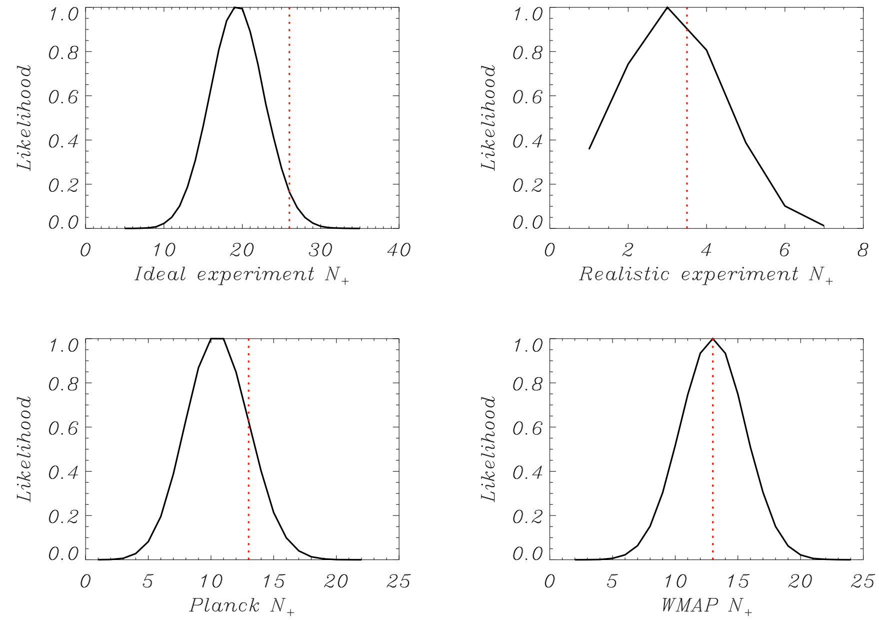

Figure 4.7: This is a plot of the distribution of the number of positive multipoles for the Monte Carlo simulation for the ideal experiment (upper left), the realistic experiment (upper right), Planck (lower left), and WMAP (lower right). The dotted red line shows where $N_+ = \frac{1}{2}N_{bins}$

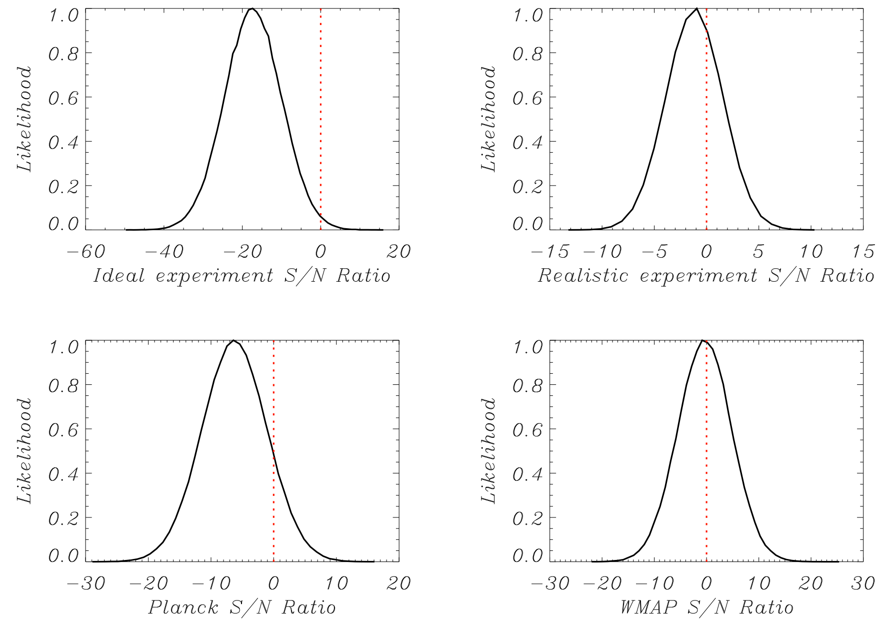

Figure 4.8: The S/N statistic distribution for the ideal experiment (upper left), realistic experiment (upper right), Planck (lower left), and WMAP (lower right). The dotted red line shows where $S/N = 0$.

for the Monte Carlo simulation with $r = 0.3$. If $r = 0.3$ we would have a 0.8% probability of the measured $S/N > 0$. This negative value signifies that a non-zero tensor-to-scalar ratio produced an anti-correlation. We can assume that the standard deviation would be the same if the mean of S/N was 0 (equivalent to $r = 0.0$), because it is equivalent to adding a constant value to every measured value (and hence adding a constant to S/N which would not change the error). Therefore, if $r = 0$, the probability of getting $S/N < -17.4$ is 0.8%, and hence we have a 99% chance that $r \neq 0$. A plot of $\langle S/N \rangle$ and $\sigma_{S/N}$ as a function of r is shown in Fig. 4.9. As can be seen from the plot, we can predict a value of r for any value of S/N. The value of $\sigma_{S/N}$ is a relatively constant function of r and so our prediction about the distribution of S/N for different value of r is a good approximation to the true distribution.

The Wilcoxon rank sum test gives $U_{avg} - m_U = -1.23\sigma_U$. The variable U_{avg} is the mean value for U in the Monte Carlo simulations described earlier. The

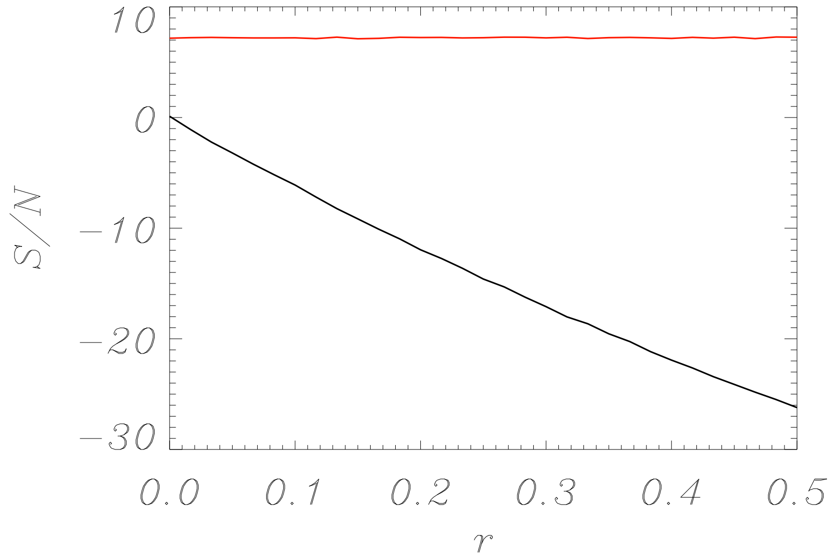

Figure 4.9: This is a plot of $\langle S/N \rangle$ and $\sigma_{S/N}$ as a function of r for the ideal experiment. The black line is $\langle S/N \rangle$ and the red line is $\sigma_{S/N}$.

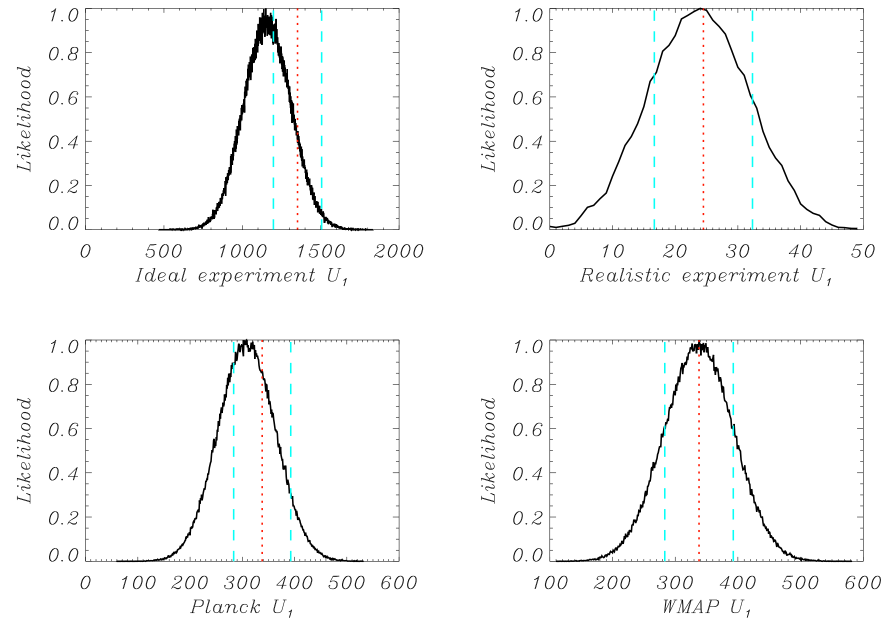

Figure 4.10: This is the plot of the distribution of U for the ideal experiment (upper left), realistic experiment (upper right), Planck (lower left), and WMAP (lower right). The red dotted line is the value for m_U and the light blue dashed lines enclose the 1σ region for U assuming the hypothesis that $r = 0$

values m_U and σ_U are given in Section 4.3.3. The distribution of U for the Monte Carlo simulations with $r = 0.3$ is shown in Fig. 4.10. The standard deviation of the distribution of measured U is the same as the standard deviation of the distribution of U assuming the hypothesis that $r = 0$. The only difference between the distributions is that m_U is shifted by a constant value. Therefore, there is a 22% chance that $U - m_U < -2\sigma_U$. There is also a 40% chance that we measure $U - m_U < -1\sigma_U$, and are not even able to make a 1σ detection of PGWs.

A comparison of the three tests is shown in Fig. 4.11. This is obtained by simulated with with several values of r and then interpolating between them. A 2σ detection is obtained for $r = 0.26$ (S/N test), $r = 0.3$ (sign test), and $r = 0.5$ (Wilcoxon rank sum test), highlighting its intended use as a monitor of a false positive detection for large r.

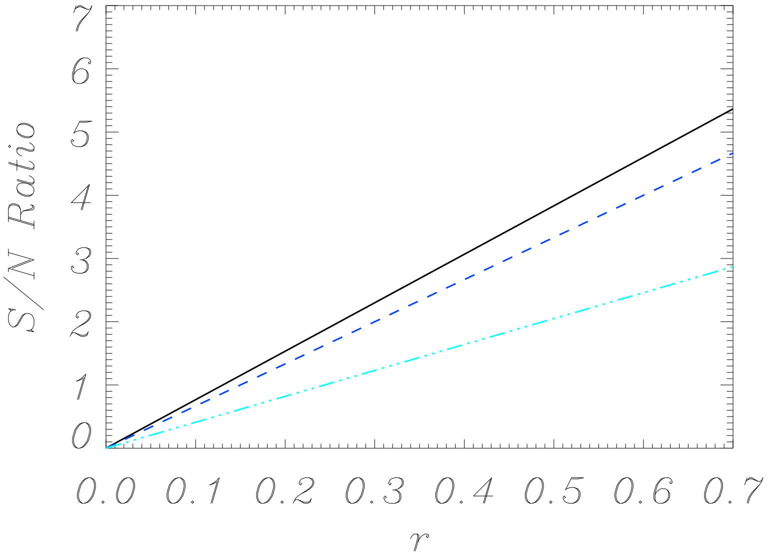

Figure 4.11: This is the plot of the signal-to-noise ratio (number of σs) for different values of r for the three different tests. The black line is the S/N test, the dashed dark blue line is the sign test, and the dotted-dashed light blue line is the Wilcoxon rank sum test

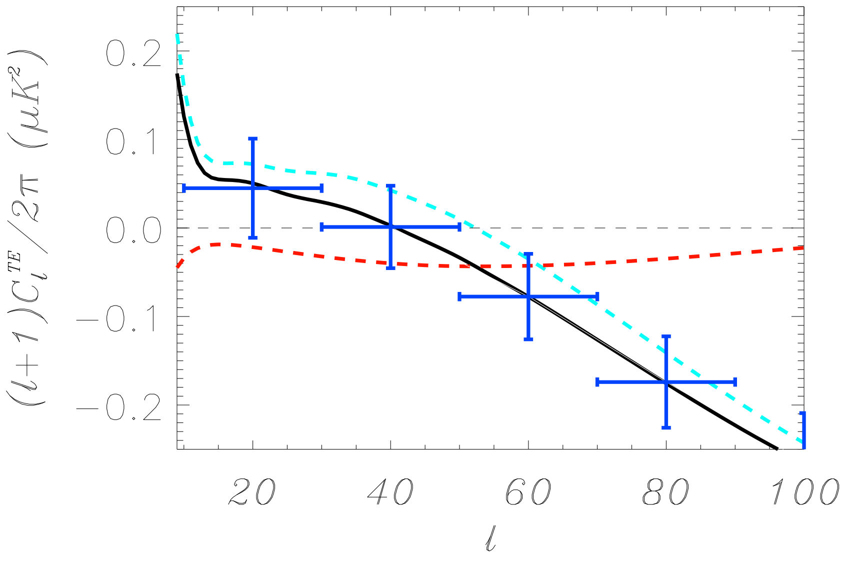

Figure 4.12: This figure is the same as Fig. 4.4 but presents for the realistic experiment with $r = 0.9$.

4.4.2 Realistic Ground Based Experiment

A plot of the error bars for the realistic experiment is shown in Fig. 4.12 with $r = 0.9$. Observations on an incomplete sky require the multipoles to be binned in sizes of $\Delta\ell = 10$. This experiment has much larger error bars than the ideal experiment and it is not able to detect low values of r with the TE cross-correlation only. Plots of the TE power spectrum due to density perturbations and PGWs are shown in Fig. 4.12 along with the combined TE power spectrum.

For this experiment, the constraints on measuring ℓ_0 are significantly larger than those for the ideal experiment. The 1σ uncertainty on ℓ_0 is $\Delta\ell_0 \approx 10$. This corresponds to a limit of $r < 0.9$ with 68% confidence. If we want a 2σ limit, then the constraint expands to $r \leq 1.5$. If we assume the inflationary consistency relation, then this error on ℓ_0 would correspond to a 1σ upper limit of about $r \lesssim 0.7$. Fig. 4.13 shows the region of r and n_t allowed with 68% confidence of ℓ_0.

As mentioned earlier, Fig. 4.6 shows the signal-to-noise ratio of the zero

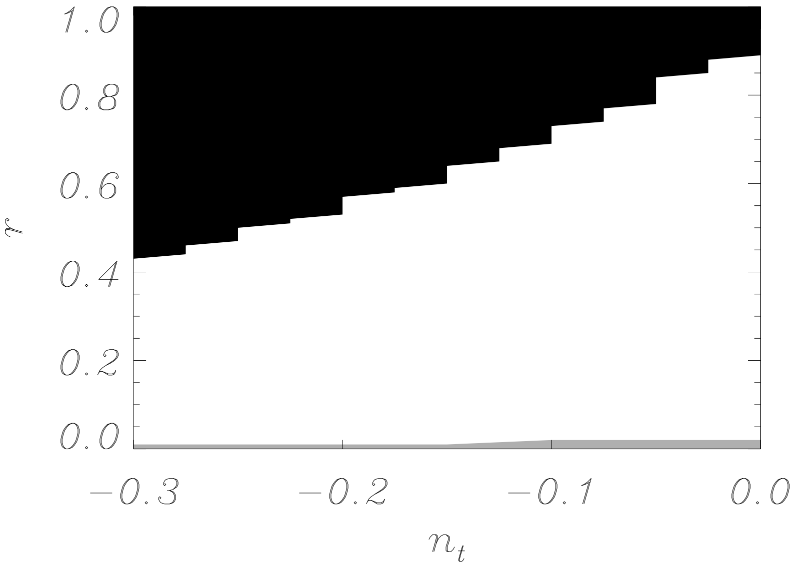

Figure 4.13: An upper limit on r due to the realistic experiment with $\Delta l_0 = 10$

multipole method for the realistic experiment. The measurements of the BB power spectrum are much more sensitive to PGWs and the sensitivity is roughly the same as in the ideal experiment. This shows that the zero multipole method is less sensitive to PGWs than measurements of the BB power spectrum.

The results for the Wiener filtering method are much worse than those for the ideal experiment for $r = 0.3$. Since this experiment observes a small portion of the sky, the multipoles are correlated and we must bin together to get reasonably uncorrelated measurements. For this experiment, we only have 7 to 8 uncorrelated multipoles, instead of 52 uncorrelated multipoles in the case where the full sky is observed. Getting 7 out of 8 negative multipoles is a 3% probability if there are no PGWs. For the Monte Carlo simulations of the realistic experiment, on average, half of measured multipoles are positive and half are negative. A plot of the distribution of the number of positive multipoles is shown in the upper right panel of Fig. 4.7. In this case, we cannot distinguish $r = 0.3$ from $r = 0.0$ with any significance.

The S/N test gives an average value of $S/N = -0.95$ with standard deviation of 2.64. For the realistic toy experiment, the distribution of S/N for $r = 0.3$ is shown in the upper right panel of Fig. 4.8. In order to obtain 68% confidence detection of PGWs, we must use $r \approx 0.7$. In this sense the TE test provides monitoring and insurance against false positive detection with $r > 0.7$, which could arise, for example, if foregrounds or other systematic effects arer improperly removed.

The last statistical test, the Wilcoxon rank sum test, gives $U_{avg} - m_U = -0.20\sigma_U$. The distribution of U for $r = 0.3$ is shown in the upper right panel of Fig. 4.10. This gives the weakest result in terms of the three tests for the Wiener filtered data. The realistic experiment will not be able to constrain $r < 0.3$ using the TE cross correlation power spectrum. Its limit is closer to $r < 0.7 - 0.9$ at only 68% confidence depending on the test used. For a higher confidence in a detection of PGWs, the value of r would need to be much higher. Since the observed distribution of U corresponds almost exactly to the simulated distribution of U under the assumption that $r = 0$, therefore we have a 16% chance of measuring $U - m_U < -1\sigma_U$.

4.4.3 WMAP

A constraint on r using a measurement of ℓ_0 for WMAP is almost impossible. Using error bars consistent with WMAP noise, we get $\Delta\ell_0 \approx 15$ for an input of $r = 0.3$ and $n_t = 0$. The published results of WMAP give limits of $r < 0.3$ so adding this method to the WMAP results would not change constraints significantly. In fact, using the real WMAP data[3] we get $\ell_0 \approx 48$. With an uncertainty of $\Delta\ell_0 \approx 15$, the probability of getting a value farther away from $\ell_0 = 53$ is larger than 50%, so we cannot detect primordial gravitational waves in the published WMAP data using the zero multipole method.

The results of the Wiener filtering showed that the WMAP cannot make a detection of gravitational waves using the TE cross correlation power spectrum alone. As with the two toy experiments, the result of the scalar and tensor separation was similar. The Monte Carlo simulation gave on average gave 13 positive multipoles out of a total of 26 uncorrelated multipoles. We would get the same

---

[3] http://lambda.gsfc.nasa.gov/

result if the input data had $r = 0.0$ so we cannot detect PGWs with WMAP using only the TE power spectrum. A plot of the distribution of the number of positive multipoles is shown in the lower right panel of Fig. 4.7. As can be seen, this distribution of N_+ for WMAP noise and $r = 0.3$ is simply the distribution for $r = 0$.

For WMAP, the S/N test gives the value of $S/N = -0.02$ with a standard deviation of 5.09. The distribution is shown in the lower right panel of Fig. 4.8. The distribution is centered around $S/N = 0$ so there is no chance of using this test to detect PGWs in WMAP's TE power spectrum. The probability of getting a 1σ or 2σ detection is the same probability that we would randomly get a detection if there are no PGWs.

The rank sum test gives a value of $U_{avg} - m_U = -0.004\sigma_U$, which is implies no ability to distinguish WMAP's observed TE data from a data set with no PGWs. A plot of the distribution of U for WMAP error bars is shown in the lower right panel of Fig. 4.10. We reach the same conclusion for WMAP noise as for the realistic experiment. There is only a 16% chance that we can measure $U - m_U < -1\sigma_U$ and make a 1σ detection of $r = 0.3$

The published WMAP results show an anti-correlation of TE power spectrum at large scales. Unfortunately this is not a detection of PGWs as theorized in [58]. The contribution to the TE power spectrum due to PGWs only changes sign once for $\ell \lesssim 90$. If a claimed evidence for gravitational waves is to be believed, then the TE power spectrum would have to change sign three times for $\ell \lesssim 60$. In fact, other than the two anticorrelations at low ℓ, the rest of the multipoles, up to $\ell = 53$, are consistent with $r = 0$. None of the described tests applied to the current WMAP data will give any detection of PGWs.

4.4.4 WMAP 5

We apply the test described in the previous section to the publically available WMAP5 data. We use both the binned and unbinned versions of the data. The unbinned version of the data provides values and errors for every multipole. The binned version of the data provides fewer measurements, but smaller error

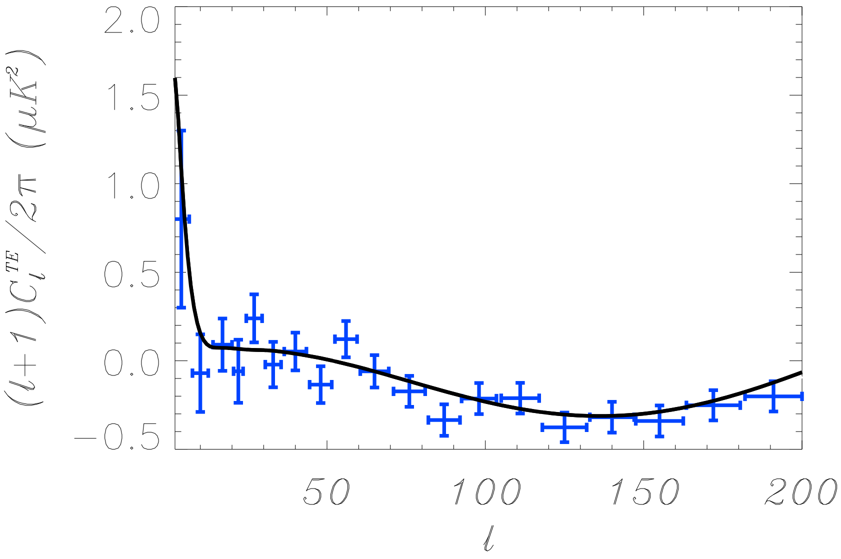

Figure 4.14: The solid black line is the TE cross correlation power spectrum predicted by the ΛCDM model with no PGWs, which is the best fit fo all WMAP5 data. This plot also shows WMAP5 results for TE cross correlation with errorbars (blue crosses).

bars because binning means the averaging over ℓ from ℓ to $\ell + \Delta\ell$. The current best constraint on r is $r < 0.2$ at 95% confidence level. This constraint is provided by WMAP5 in combination with distance measurements of Type Ia supernovae and imprints of baryon acoustic oscillations on the spatial distribution of galaxies ([38]). By itself, WMAP5 provides a constraint of $r < 0.43$ at 95% confidence level ([79]). The ΛCDM model of WMAP5 gives $\ell_0 = 52$. A plot of the WMAP5 best fit within the framework of the ΛCDM model and their results of C_ℓ^{TE} measurements are shown in Fig. 4.14.

We use several different fitting routines to determine the value of ℓ_0 from the WMAP5 data.

a) The first routine is a linear fit. This routine minimizes the χ^2 error criterion. In other words, this is the least squares technique. We minimize the value $S_1 = \sum_i (f(\ell_i) - C_{\ell_i})^2$, where f is our linear fitting function and ℓ_i and C_{ℓ_i}

are the data.

b) The second routine, which is also a linear fit, is a least absolute deviations fitting routine. Instead of minimizing S_1, we minimize $S_2 = \sum_i |f(\ell_i) - C_{\ell_i}|$. An advantage to this routine is that it should be more robust to outlying data compared to the least squares technique. A disadvantage is that it is unstable. By instability, we mean that small variations in ℓ can cause considerable variations in the slope of the fitted line. In contrast, the least squares technique is stable. The second disadvantage is that the minimum of S_2 may correspond to more than one fitting line.

c) Our third fitting routine, in contrast to both previous ones, is a polynomial fit rather than linear. We use the same least squares fitting routine as our first routine, except we fit to a quadratic polynomial instead of a linear one.

For all our routines, we fit over the range $\ell = 35$ to $\ell = 70$. The TE correlations can be approximated as a line over this range for our first two routines and ℓ_0 will be within this range unless r is extremely large.

The results for the calculation of ℓ_0 for the two linear fitting routines are shown in Fig. 4.15 and the result for the polynomial fitting routine is shown in Fig. 4.16. A table of the calculated ℓ_0 and their standard deviation is shown in Table 4.1. There is no detection of PGWs using this method. The measured values are all consistent with $\ell_0 = 52$. To go from a limit on ℓ_0 to a limit on r, we first calculate the ℓ_0 as a function of r and n_t. We then marginalize over n_t by integrating the likelihood function to remove the dependance on n_t. Doing this, we get a limit of $r < 2.0$ at 95% confidence. If we use the assumption that the PGWs are generated by inflation and apply the inflationary consistency relation, $n_t = -r/8$ ([80]), we get $r < 1.0$ at 95% confidence. Neither of these is better than $r < 0.43$ at 95% confidence.

Applying the filtering method, we assume that the power spectrum of scalar perturbations is given by the ΛCDM model, which is the best fit to the WMAP5 data. Then, we apply the statistical tests **a**, **b**, and **c** to the difference between the power spectrum of this model and power spectrum formed from the raw data.

The results of the filtering are shown in Fig. 4.17. For the Wilcoxon rank

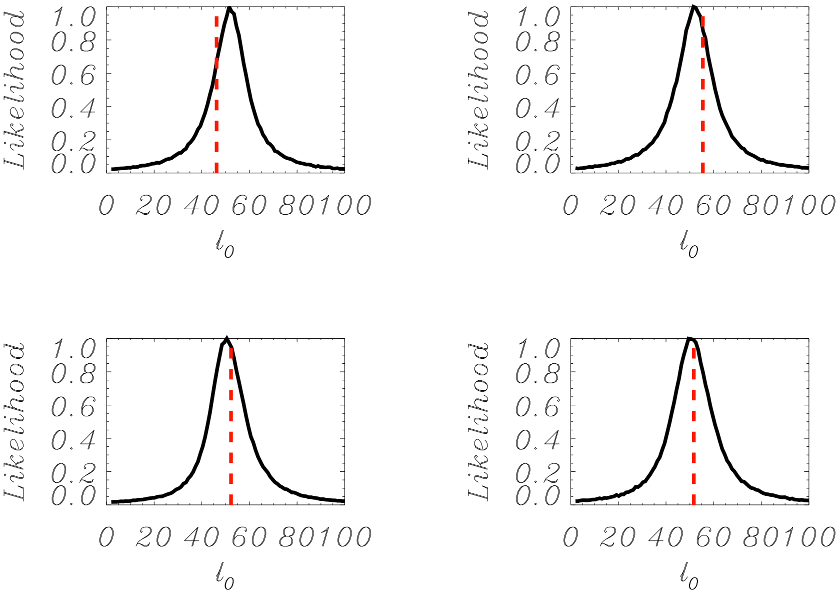

Figure 4.15: These plots show the results of the calculation of ℓ_0 for the two linear fitting routines. The top row is for the unbinned data and the bottom row is for the binned data. The left column is the routine which minimizes the χ^2 error criterion. The right column is the least absolute deviation fitting routine.

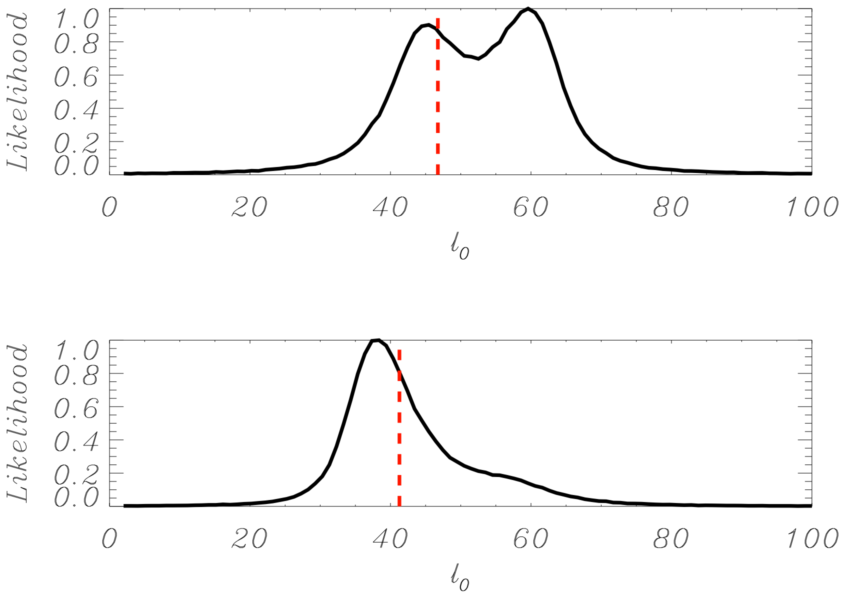

Figure 4.16: These plots show the results of the calculation of ℓ_0 for the polynomial fitting routine. The top plot is for the unbinned data and the bottom plot is for the binned data.

sum test, the plots show the mean value of U if $r = 0$ in the WMAP5 data set and the mock data set (red dashed line) and the distribution of U given the WMAP5 data set and a mock data set with $r = 0$ (solid black line). Results using both the unbinned WMAP5 data along with the binned WMAP5 data are shown in Fig. 4.17. For the Wilcoxon rank sum test, the distribution of U is centered somewhat below the mean value we would get if $r = 0$ in the WMAP5 data. The difference is only 0.34σ for the unbinned data and 0.6σ for the binned data so we cannot reject the hypothesis that $r = 0$. The S/N values are less than half of a standard deviation away from a value of zero, which they would be if the TE power spectrum due to density perturbations matched perfectly to the measured TE power spectrum. We cannot place a limit on r using these tests because they are only testing hypotheses that $r = 0$. Since these are non-parametric statistical tests, they can help to answer the question whether $r = 0$ or not. In other words, all these tests do not help constrain r.

4.4.5 Planck

The uncertainty in ℓ_0 is much better for Planck than for the realistic experiment and about twice as large for the ideal experiment. The Monte Carlo simulations resulted in $\Delta\ell_0 \approx 3.75$ for an input TE power spectrum with $r = 0.3$ and $n_t = 0$. This results in $\approx 68\%$ confidence that $r \neq 0$, under the assumption that $n_t = 0$.

The sign test gives on average 10 positive measurements of the TE power spectrum out of a total of 26 uncorrelated multipoles. There is a 16% chance of getting ≤ 10 positive multipoles if $r = 0$. A plot of the distribution of the number of positive multipoles for Planck is shown in the lower left panel of Fig. 4.7. There is a 50% chance that we will measure $N_+ < 10$ and hence have a 1σ detection of $r = 0.3$.

The S/N test gives a value of $S/N = -6.24$ with a standard deviation of 5.09. There is only a 10% chance that the S/N test results in a value of S/N larger than zero, if $r = 0.3$, and a 10% chance getting $S/N < -3.12$ if $r = 0$. This is close to a 90% probability of detection. The distribution of the S/N variable is

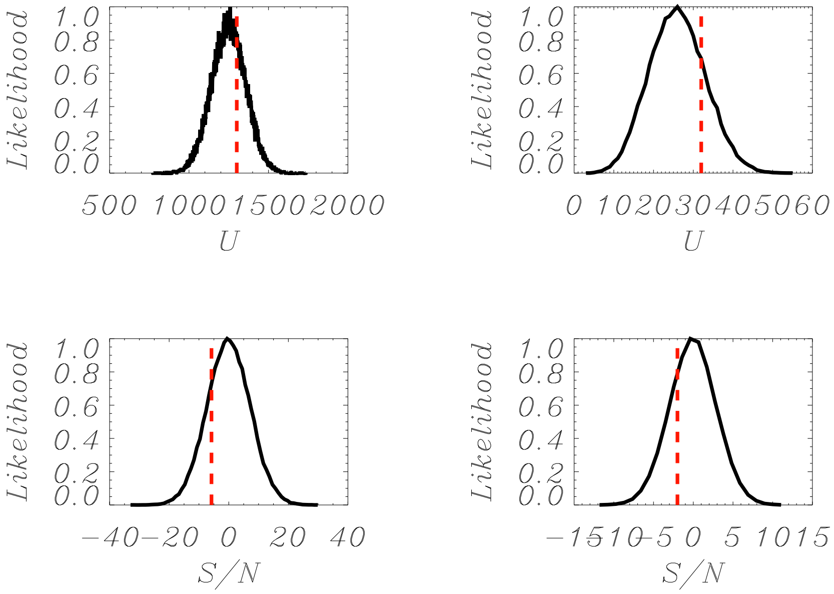

Figure 4.17: The upper left plot shows the results for the Wilcoxon rank sum test using the unbinned data. The dashed red line shows the mean value of U if $r = 0$. The solid black line is the distribution of U with the WMAP5 data set and a mock data set with WMAP5 error bars and $r = 0$. The upper right plot is the same as the upper left plot except it uses the binned data. The lower left plot shows the results for the S/N test using the unbinned data. The dashed red line in the value of S/N for WMAP5. The solid black line is the distribution of the S/N value for a mock data set with $r = 0$ and WMAP5 error bars. The lower right plot is the same as the lower left plot except it uses the binned data.

shown in lower left panel of Fig. 4.8.

Again, the rank sum test gives the lowest confidence result with a value of $U_{avg} - m_U = -0.66\sigma_U$. A plot of the distribution of U is shown in the lower left panel of Fig. 4.10. There is a 37% probability that we will measure $U - m_U < -1\sigma_U$ and a 9% probability that we measure $U - m_U < -2\sigma_U$ for Planck.

4.5 Comparing Measurements of the TE Power Spectrum to the BB Power Spectrum

As mentioned earlier, it was originally suggested that it might be easier to detect PGWs using the TE power spectrum instead of the BB power spectrum. For both methods, this turned out not to be true. The reason for this is because we are trying to measure the TE power spectrum at the place where the signal is lowest ($C_\ell^{TE} = 0$). In measurements of the BB power spectrum, if we neglect instrumental noise, the signal decreases with a decrease in r and so does the cosmic variance limited uncertainty. This is not the case for the TE power spectrum. The uncertainty in the measurement of the TE power spectrum due to PGWs is determined by the total TE, TT, and EE power spectra. When the TE power spectrum goes to zero, the TT and EE power spectrum do not approach zero (in fact, they increase as we approach to ℓ_0). We therefore have a low signal-to-noise ratio around ℓ_0 making it very hard to detect PGWs using the zero multipole method. Below we give simple summarizing arguments why the same is true for the Wiener filtering of the TE power spectrum

If $N_\ell \ll C_\ell^{BB}$, the signal-to-noise ratio for the BB power spectrum is

$$(S/N)_{BB} = \frac{C_\ell^{BB}}{\Delta C_\ell^{BB}} = \gamma \frac{C_\ell^{BB}}{C_\ell^{BB} + N_\ell} \approx \gamma, \tag{4.20}$$

where

$$\gamma = \sqrt{\frac{(2\ell+1) f_{sky}}{2}} \tag{4.21}$$

If $N_\ell > C_\ell^{BB}$ then we will not be able to detect PGWs and a comparison with the TE power spectrum is not worthwhile.

If $N_\ell \ll C_\ell^{EE}$ and $r < 1$, for the TE power spectrum, the signal-to-noise ratio is

$$\begin{aligned}(S/N)_{TE} &= \frac{C_{\ell,t}^{TE}}{\Delta C_\ell^{TE}} \\ &= \sqrt{2}\gamma \frac{C_{\ell,t}^{TE}}{[(C_\ell^{TE})^2 + (C_\ell^{TT} + N_\ell/2)(C_\ell^{EE} + N_\ell)]^{1/2}} \\ &\approx \sqrt{2}\gamma \frac{C_{\ell,t}^{TE}}{[(C_\ell^{TE})^2 + C_\ell^{TT} C_\ell^{EE}]^{1/2}} \\ &\approx \sqrt{2}\gamma \frac{r}{\alpha + \beta r} \qquad (4.22)\end{aligned}$$

where α and β are

$$\begin{aligned}\alpha &= \frac{\sqrt{(C_{\ell,s}^{TE})^2 + C_{\ell,s}^{TT} C_{\ell,s}^{EE}}}{D_\ell^{TE}}, \\ \beta &= \frac{2C_{\ell,s}^{TE} D_\ell^{TE} + D_\ell^{TT} C_{\ell,s}^{EE} + C_{\ell,s}^{TT} D_\ell^{EE}}{2D_\ell^{TE}\alpha}, \qquad (4.23)\end{aligned}$$

where

$$D_\ell^{XY} = C_{\ell,t}^{XY}/r \qquad (4.24)$$

One can see that α and β are on the order of unity. Therefore, the signal-to-noise ratio is approximated as

$$(S/N)_{TE} = \sqrt{2}\gamma \frac{r}{\alpha + \beta r} \approx \sqrt{2}\gamma \frac{r}{\alpha} \qquad (4.25)$$

In other words if $r < \alpha/\beta \sim 1$, BB measurements have the obvious advantage in comparison with the Wiener filtering of the TE power spectrum. Indeed if $r \lesssim 1$, $(S/N)_{BB} \sim \gamma$, while $(S/N)_{TE} \sim \gamma r < \gamma$. This is because in BB measurements, applying proper data analysis, we can entirely eliminate contributions of scalar perturbations to CMB polarization signal as well as to the uncertainties. For the perfect Wiener filtering of the TE power spectrum, we can eliminate the contribution of scalar perturbations to the signal only, but cannot eliminate their contribution to the uncertainties.

4.6 Conclusion

The measurement of where the TE cross correlation first changes sign can be used to detect or put constraints on PGWs. Such constraints are not as strong as the ones given by measurements of the BB power spectrum, however it is useful to have a supplementary method to detect PGWs. We have shown how well the TE mode can constrain the amount of PGWs from just a measurement of the angular scale where it first changes sign for two different toy experiments and two real satellite experiments. The absolute best limit with which we can measure ℓ_0 only gives us less than a 3σ detection of the PGW component if $r = 0.3$. The current confidence limits gives us $r < 0.3$ at 95% confidence level. Current and future experiments are optimized to measure the BB power spectrum if $r \leq 0.1$ even in the presence of foregrounds, which are not taken into account in this chapter. Future satellite experiments should be able to detect $r < 0.01$ which is 10 times better than the sensitivity to r than the result of the ideal experiment. If one neglects even cosmic variance, the discreteness of ℓ limits the calculation of ℓ_0, and the sensitivity to r, to values considerably larger than 0.01. The cosmic variance is largest at low ℓ and is proportional to the total power spectrum. Since the TE cross correlation has contributions from density perturbations the errors in the measured TE power spectrum make detecting deviations of ℓ_0 from 53 difficult, though they also provide insurance against a false detection or imperfect subtraction of instrumental and foreground systematic effects.

The other method described in this chapter is one in which we filter out the signal due to density perturbations, leaving only the contribution to the TE power spectrum due to PGWs. We then test the resulting TE power spectrum to see if it is negative. Three different statistical tests were used to see if there was a significant detection of PGWs. The S/N test can give a value for r using a comparison with Monte Carlo simulations, while the Wilcoxon rank sum test can only give an allowable range for r. The sign test will only tell us if $r \neq 0$.

Using the Wiener filtering method, we are unable to make as significant of a detection as using the zero multipole method. The best result was for the S/N test which would give a 2.3σ detection of $r = 0.3$. To detect PGWs on the level of 3σ, the tensor-to-scalae ratio r should be $r \geq 0.4$. The sign test would give 2σ detection for $r = 0.3$ and a 3σ detection for $r = 0.45$. The Wilcoxon ranked sum test gives only a 1.2σ detection for $r = 0.3$ and a 3σ detection for $r = 0.7$. Similar results were gotten for the other three experiments tested. Thus in the sense of potential to detect PGWs, the zero multipole method is the best, next best is the S/N test, then the sign test, and the worst is the Wilcoxon ranked sum test.

[58] present illustrative examples in which high r is consistent with measured TT, EE, and TE correlations. The value of r is so high in these examples that if PGWs with such r really existed, current BB experiments would already detect PGWs. All models predict that the TE cross correlation power spectrum change sign only once for $\ell < 100$. The fact WMAP cannot exclude several multipoles with $C_\ell^{TE} > 0$ in between multipoles of $C_\ell^{TE} < 0$ means that the TE cross correlation power spectrum either changes sign several times for $\ell < 100$ or there is some instrumental noise which causes some anticorrelation measurements. Using instrumental noise consistent with WMAP, our Monte Carlo simulations give $\Delta\ell_0 \approx 16$ and $\ell_0 > 40$, which means that there is no evidence of PGWs in the TE correlation power spectrum.

We applied our results to the released WMAP5 dataset. The WMAP5 data was chosen as WMAP5 has made the best measurements of the TE power spectrum so far at the scales we are looking at. QUaD has also made high sensitivity measurements of the TE power spectrum, but on smaller scales ([81]). We are able to say that $r < 2.0$ at 95% confidence, which is nowhere near the current $r < 0.43$ limits at 95% confidence provided by WMAP5 alone. Using this technique, it will be impossible to improve this constraint. These techniques, however, are helpful as insurance against a false detection of r from such effects as beam systematics [2]. These effects could be potential pitfalls for upcoming experiments with higher signal-to-noise than WMAP.

This chapter is the combined text of the material that appears in Monthly Notices of the Royal Astronomical Society, Volume 386, Issue 2, pp 1053-1063, 2008, Polnarev, A.G, Miller, N.J., and Keating, B.G "CMB Temperature Polarization Correlation and Primordial Gravitational Waves" and Advances in Astronomy, 309024, 2009, Miller, N.J. Keating, B.G., and Polnarev, A.G., "CMB Temperature Polarization Correlation and Primordial Gravitational Waves: WMAP5". The dissertation author was the primary investigator and author of these papers.

Table 4.1: A table of the zero multipole, ℓ_0, and the uncertainty in ℓ_0, $\Delta\ell_0$, for the different fitting routines and data sets considered in Section 4.4.4

Fitting	Data	ℓ_0	$\Delta\ell_0$
linear, χ^2	Unbinned	46.2	14.2
linear, abs. dev.	Unbinned	55.5	14.8
quadratic, χ^2	Unbinned	46.8	11.2
linear, χ^2	Binned	52.26	13.6
linear, abs. dev.	Binned	51.7	14.3
quadratic, χ^2	Binned	41.3	10.1

Chapter 5

Using the CMB to Constrain Neutrino Mass and Chemical Potential

The CMB holds a wealth of information about the evolution of the universe. From measurements of the CMB, we can constrain basic cosmological parameters such as the spatial curvature of the universe and the energy density of baryons, dark matter, and dark energy. The neutrino energy density, which is related to the sum of the neutrino masses, is a parameter that has already been constrained by CMB temperature and polarization measurements. Several groups have determined that future CMB experiments will be able to measure neutrino properties to unprecedented accuracy [28, 82]. This chapter will go further and look at how well future CMB experiments will be able distinguish between the different masses of the three neutrinos, not just the neutrino energy density which is related to the sum of the neutrino masses, and how well we will be able to constrain the neutrino degeneracy parameters. In section 5.1, we will give an introduction to neutrinos and the current limits on their masses and parameters describing the neutrino mixing matrix. In section 5.2, we will discuss how neutrinos affect Big Bang Nucleosynthesis (BBN), the CMB, and large scale structure. In section 5.3, we will describe the MCMC simulations we ran. In section 5.4, we will show the results of our MCMC simulations. In section 5.5, we will give some concluding remarks about our simulations.

5.1 Introduction

A neutrino is an electrically neutral and weakly interacting particle [83]. It was first proposed by Wolfgang Pauli in 1930 to preserve conservation of energy, momentum, and angular momentum in beta decay (the decay of a neutron into a proton, electron, and anti-neutrino). In the standard model, there are three flavors of neutrinos that participate in the weak interaction: the electron neutrino, the muon neutrino, and the tau neutrino. However, if neutrinos have mass, then the mass eigenstates are not the same as their flavor eigenstates. The neutrino that has mass m_1, ν_1 is a quantum mechanical superposition of the three flavor eigenstates. This leads to a phenomenon known as neutrino oscillation, where a neutrino created with a specific flavor can later be measured to have a different flavor. The probability of detecting a different flavor of neutrino oscillates as the neutrino propagates leading to the name neutrino oscillation.

The matrix that takes the neutrino mass eigenstates to flavor eigenstates is called the Maki-Nakagawa-Sakata mixing matrix. Neutrino mixing can be written as

$$|\nu_\alpha\rangle = \sum_i U_{\alpha i}|\nu_i\rangle \tag{5.1}$$

where U is the Maki-Nakagawa-Sakata mixing matrix. In the equation, the subscript α refers to a flavor state and i refers to a mass state. The mixing matrix is described by three mixing angles and a CP violating term. The matrix is

$$U = \begin{pmatrix} c_{12}c_{13} & s_{12}c_{13} & s_{13}e^{-i\delta} \\ -s_{12}c_{23} - c_{12}s_{23}s_{13}e^{i\delta} & c_{12}c_{23} - s_{12}s_{23}s_{13}e^{i\delta} & s_{23}c_{13} \\ s_{12}s_{23} - c_{12}c_{23}s_{13}e^{i\delta} & -c_{12}s_{23} - s_{12}c_{23}s_{13}e^{i\delta} & c_{23}c_{13} \end{pmatrix} \tag{5.2}$$

where $s_{ij} = \sin\theta_{ij}$ and $c_{ij} = \cos\theta_{ij}$. The parameters θ_{12}, θ_{23}, and θ_{13} are the three mixing angles and δ is the CP violating term. The columns refer to the different mass states, while the rows are for the different flavor states.

Neutrino oscillation depends on the mass squared differences between the different mass eigenstates. The constraints are therefore limits on $\Delta m_{ij}^2 \equiv m_i^2 - m_j^j$.

The current limits, from atmospheric and solar neutrino experiments, are $\Delta m^2_{21} = 7.9^{+0.6}_{-0.4} \times 10^{-5}$ eV^2, $\Delta m^2_{31} = 2.43^{+0.13}_{-0.13} \times 10^{-3}$ eV^2. Since $\Delta m^2_{31} \gg \Delta m^2_{21}$, there are two different possible neutrino hierarchies. The normal hierarchy is when $m_3 \gg m_1 \approx m_2$. The inverted hierarchy is when $m_1 \approx m_2 \gg m_3$. The current limits on the neutrino mixing matrix parameters are $\sin^2 2\theta_{13} < 0.032$, $\tan^2\theta_{12} = 0.45^{+0.09}_{-0.07}$, and $\sin^2 2\theta_{23} = 1^{+0.0}_{-0.1}$.

Neutrinos obey Fermi-Dirac statistics where the distribution function can be written as

$$\begin{aligned} f_\nu(p;T_\nu;\xi) &= \frac{1}{e^{\frac{p}{T_\nu}-\xi}+1} \\ f_{\bar\nu}(p;T_\nu;\xi) &= \frac{1}{e^{\frac{p}{T_\nu}+\xi}+1} \end{aligned} \tag{5.3}$$

where $\xi \equiv \mu/T_\nu$ is the degeneracy paramater and T_ν is the neutrino temperature [84]. We are using natural units where $\hbar = c = k_B = 1$. The degeneracy parameter is a comoving invariant, unchanged as the universe expands. Combining CMB measurements (BOOMERANG and DASI) with BBN (helium and deuterium abundance) and SNIa data gives the following 2σ constrains on the degeneracy parameter [85]:

$$\begin{aligned} -0.01 < \quad & \xi_{\nu_e} \quad < 0.22 \\ | \quad & \xi_{\nu_{\mu,\tau}} \quad | < 2.6. \end{aligned} \tag{5.4}$$

If the neutrino degeneracy parameters are not independent and they all have the same value, then we get the following constraint [86, 87, 88]

$$|\xi_\nu| \le 0.1. \tag{5.5}$$

We can write the neutrino energy density and pressure in terms of their distribution function and comoving momentum, $q = pa$, as

$$\begin{aligned} \rho_\nu + \rho_{\bar\nu} &= \frac{a^{-4}}{2\pi^2}\int_0^\infty q^2 dq \sqrt{q^2+(aM)^2}\left[f_\nu(q/a;T_\nu;\xi) + f_{\bar\nu}(q/a;T_\nu;\xi)\right] \\ P_\nu + P_{\bar\nu} &= \frac{a^{-4}}{6\pi^2}\int_0^\infty q^2 dq \frac{q^2}{\sqrt{q^2+(aM)^2}}\left[f_\nu(q/a;T_\nu;\xi) + f_{\bar\nu}(q/a;T_\nu;\xi)\right] \end{aligned} \tag{5.6}$$

where $M = m_\nu/T_\nu$.

When calculating the energy density and pressure of massive neutrinos, the usual equations require the mass and the distribution function. Since the distribution function depends on the degeneracy parameters of the flavor eigenstates and the masses depend on the mass eigenstates, this is not as simple. Since neutrino masses are small enough, we can define an effective mass for the flavor eigenstates using

$$m_{\alpha,\mathrm{eff}}^2 = \sum_i m_i^2 \left|U_{\alpha i}\right|^2 . \tag{5.7}$$

Using $m_{\alpha,\mathrm{eff}}$ as the mass for the neutrinos in the equations for the energy density and pressure is a good approximation and what is done for our simulations.

5.2 Neutrinos, Big Bang Nucleosynthesis, and the CMB

Neutrinos play a crucial role in the early universe. Neutrinos participate in reactions that determine the neutron-to-proton ratio which, in turn, affects the abundances of the light elements produced during Big Bang Nucleosynthesis (BBN). The weak reactions that set the neutron-to-proton ratio are

$$\begin{aligned} \nu_e + n &\rightleftharpoons p + e^- \\ \bar{\nu}_e + p &\rightleftharpoons n + e^+ \\ n &\rightleftharpoons p + e^- + \bar{\nu}_e . \end{aligned} \tag{5.8}$$

The rates of these reactions depend on the electron neutrino and anti-neutrino distribution functions, f_{ν_e} and $f_{\bar{\nu}_e}$, which depend on the electron neutrino degeneracy parameter, ξ_{ν_e}. The neutron-to-proton ratio and light element abundances also depend on the expansion rate of the universe. This depends on all three neutrinos and their degeneracy parameters. BBN therefore distinguishes ξ_{ν_e} from ξ_{ν_μ} and ξ_{ν_τ}.

The light element abundance that we are mainly concerned with is the helium abundance, Y_p. Y_p is determined principally by the neutron-to-proton ratio at $T \sim 100$ keV. This is set by the weak reactions in Eq. 5.8 and the baryon density,

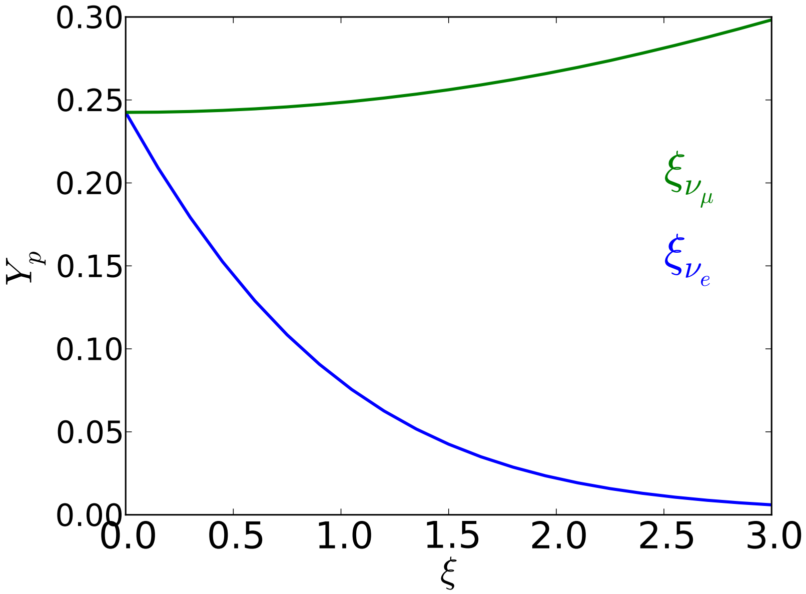

Figure 5.1: A plot of Y_p as a function of ξ. The blue line is for ξ_{ν_e}, while the green line is for ξ_{ν_μ}.

Ω_b. Therefore, Y_p depends strongly on the neutrino degeneracy parameters. A plot of the helium abundance as a function of neutrino degeneracy parameter is shown in Figure 5.1. The electron neutrino degeneracy parameter ξ_{ν_e} has a much stronger (and opposite) effect on Y_p than the muon neutrino degeneracy parameter ξ_{ν_μ}. Y_p decreases significantly as we increase ξ_{ν_e}, but slightly increases as we increase ξ_{ν_μ}. ξ_{ν_μ} and ξ_{ν_τ} have the exact same effect on Y_p so a plot for ξ_{ν_τ} not shown.

The helium abundance has a strong effect on the temperature anisotropy and polarization of the CMB. Since helium recombination occurs before hydrogen recombination, for a given baryon density, the number density of free electrons at hydrogen recombination depends directly on the helium abundance. In Chapter 1.1, we described Silk damping. The photon mean free path, which determines the scale at which the anisotropies are damped, is inversly proportional to the number density of free electrons. Increasing Y_p reduces the number density of free electrons and therefore increases the photon mean free path. The result would be a suppression of the anisotropy on larger angular scales (lower ℓ).

Neutrinos will also affect the temperature anisotropy and polarization of the CMB through their contribution to the energy density and pressure of the universe. Neutrinos will affect the growth of large-scale structure which in turn affects the amount of lensing of the CMB. The matter power spectrum is sensitive to the epoch when neutrinos became non-relativistic. Non-relativistic neutrinos are a source of cold dark matter (CDM). They can be deflected by gravitational potential wells and contribute to the growth of large scale structure. Relativistic neutrinos are a source of hot dark matter (HDM). They have too much energy to be caught in gravitational potential wells and will suppress structure below their free-streaming scale. Knowing when neutrinos became non-relativistic is important in determining the effects of neutrinos on large scale structure. For a flat universe, $\Omega_k = 0$, and a fixed dark energy fraction, Ω_Λ, decreasing the neutrino masses will increase the amount of HDM at the expense of CDM at a given redshift. This will cause a suppression of structure formation at high redshifts. The neutrino degeneracy parameters have a similar effect. Changing the degeneracy parameters will affect the neutrino distribution function and hence the amount of HDM and CDM at any given redshift. Since the lensing of the CMB is a direct probe of large scale structure formation, if large scale structure is suppressed, then the CMB deflection angle power spectrum, C_ℓ^{dd}, will be smaller on all scales.

A plot of the CMB TT, EE, TE, and dd power spectra as a function of neutrino degeneracy parameter is shown in Figure 5.2. A large neutrino degeneracy parameter is chosen to illustrate its effect on the theoretical power spectra.

5.3 MCMC Simulations

As has been done in [89, 90, 91], we modified the CMB Boltzmann code CAMB [25], by replacing the neutrino distribution function

$$f_\nu(q) + f_{\bar{\nu}}(q) = \frac{1}{e^q + 1} \tag{5.9}$$

with

$$f_\nu(q;\xi) + f_{\bar{\nu}}(q;\xi) = \frac{1}{2}\left(\frac{1}{e^{q+\xi}+1} + \frac{1}{e^{q-\xi}+1}\right) \tag{5.10}$$

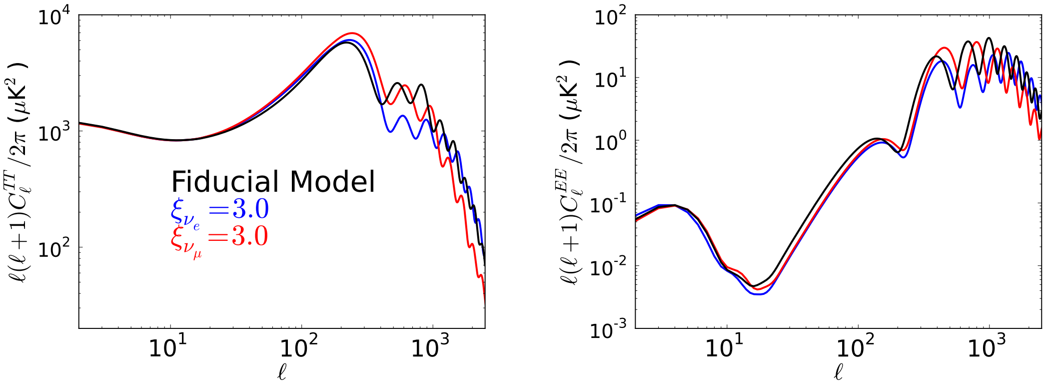

(a) TT power spectrum

(b) EE power spectrum

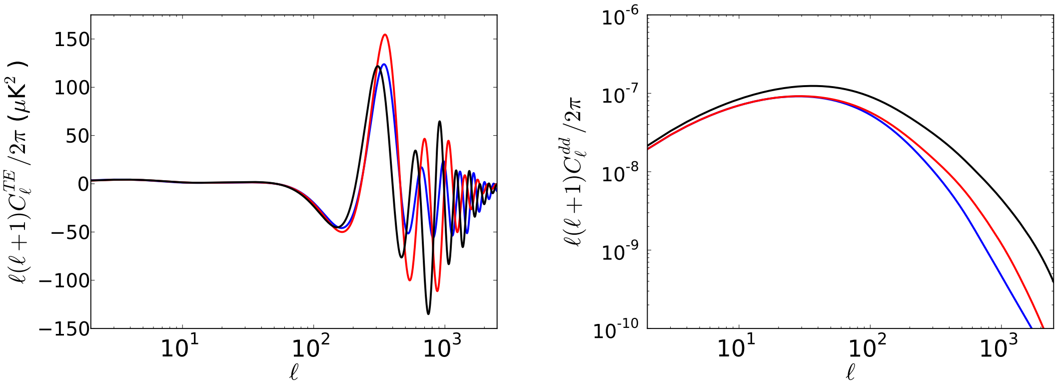

(c) TE power spectrum

(d) dd power spectrum

Figure 5.2: A plot of the CMB power spectrum for different neutrino degeneracy parameters. For each plot, black is the fiducial WMAP model, blue is $\xi_e = 3.0$, and red is $\xi_\mu = 3.0$.

where $q \equiv p/T$ and $\xi = \mu/T$ is the neutrino degeneracy parameter. We allowed the three neutrino flavors to have different degeneracy parameters ξ_{ν_e}, ξ_{ν_μ}, and ξ_{ν_τ}. For the Maki-Nakagawa-Sakata neutrino mixing matrix, we chose $\theta_{13} = 0$, $\theta_{23} = \pi/4$, $\theta_{12} = 0.59$, and $\delta = 0$, which are consistent with current observations.

We also integrated the Wagoner-Kawano BBN code into CAMB. Given $\Omega_b h^2$ and a set of neutrino denegeracy parameters, we can calculate the helium abundance, Y_p, with the BBN code. We can then input the calcuated helium abundance into CAMB instead of using a constant helium abundance for all the different cosmological models.

We used the Markov chain Monte Carlo code "CosmoMC" [26] to determine the constraints on the parameters for different experiments. CosmoMC calls CAMB to generate its theoretical models. In our simulations we adopted a 14 parameter cosmological model. We allowed m_1, Δm^2_{21}, Δm^2_{31}, ξ_{ν_e}, ξ_{ν_μ}, and ξ_{ν_τ} to be free paramaters in addition to the equation-of-state of dark energy, w, and the seven standard cosmological parameters: $\Omega_b h^2$, $\Omega_c h^2$, θ, τ, n_s, $\log(10^{10} A_s)$, r. We assumed the normal hierarchy for the masses of the neutrinos. We implemented priors on Δm^2_{21}, and Δm^2_{31} consistent with the current constraints from neutrino oscillation experiments. We could have allowed θ_{13}, θ_{23}, θ_{12}, and δ to also be free parameters with priors from neutrino experiments, but we chose to limit ourselves to only six neutrino parameters in order to get results in a reasonable timeframe. With our choice of mixing parameters, the mixing matrix is

$$U \approx \begin{pmatrix} 0.83 & 0.56 & 0 \\ -0.39 & 0.59 & 0.71 \\ 0.39 & -0.59 & 0.71 \end{pmatrix} \tag{5.11}$$

As can be seen from our mixing matrix and equation 5.7, ν_μ and ν_τ have the same effective mass. Because the muon and tau neutrinos have the same effective mass, we can swap their degeneracy parameters and not change any of our results. In addition, because the CMB only depends on the sum of neutrino and anti-neutrino distribution functions, a negative degeneracy parameter is the same as a positive degeneracy parameter.

Simulations were run for three experiments: POLARBEAR, PLANCK, and the Experimental Probe for Inflationary Cosmology (EPIC). POLARBEAR is a CMB experiment that was constructed in the Atacama desert in 2011 [92, 93] and is described in Chapter 6. PLANCK is a satellite mission run by the European Space Agency that launched in May 2009 [94]. EPIC is a mission concept study for a future satellite mission to measure the CMB polarization [95, 96]. The specifications used for each experiment is shown in Table 5.1. The specifications for POLARBEAR are taken from an early version of the POLARBEAR focal plane, but it is similar to the final version. The specifications for EPIC are chosen from the "Intermediate Mission" concept study. To generate a simulated power spectra, we used WMAP5 cosmological parameters with neutrino masses of $m_1 = 0.01\text{eV}$, $\Delta m_{21}^2 = 7.9 \times 10^{-5}\text{eV}^2$, and $\Delta m_{31}^2 = 2.4 \times 10^{-3}\text{eV}^2$. For this simulation, all neutrino degeneracy parameters were set to zero.

5.4 Results

A table of the results for the relevant neutrino parameters from our simulations are shown in Table 5.2. The parameter M_ν is the sum of the masses of the three neutrinos. All upper limits are 95% or 2σ upper limits. One dimensional likelihoods for the neutrino parameters are shown in Figure 5.3. None of the CMB experiments are able to constrain Δm_{21}^2 or Δm_{31} better than the priors we implemented. As such, their likelihoods look like the gaussian prior, so they are not shown. PLANCK is able to constrain the parameters to higher precision that POLARBEAR as a result of its ability to map the whole sky instead of the 3% that POLARBEAR will map from the ground. The constraints from EPIC should be considered the best constraints that we would ever be able to get from the CMB. The limits on ξ_{ν_e} are competitive with the results that can be obtained from ground based neutrino experiments. Several 2-dimensional likelihood plots for ξ_{ν_e} and other neutrino parameters are shown in Figure 5.3. The slight degeneracy between ξ_{ν_e} and $\Omega_c h^2$ results from the fact that an increase in neutrino energy density must be compensated by increasing the density of CDM in order to keep the change in the matter power spectrum from neutrino free-streaming fixed.

Table 5.1: Sensitivity parameters of the CMB experiments considered in this work: f_{sky} is the observed fraction of the sky, ν is the center frequency of the channels in GHz, θ_b is the full width at half maximum in arc-minutes, Δ_T is the temperature sensitivity per pixel in μK and $\Delta_E = \Delta_B$ is the polarization sensitivity.

Experiment	f_{sky}	ν [GHz]	θ_b [1']	Δ_T [μK]	Δ_E [μK]
PLANCK	0.65	30	33	4.4	6.2
		44	23	6.5	9.2
		70	14	9.8	13.9
		100	9.5	6.8	10.9
		143	7.1	6.0	11.4
		217	5.0	13.1	26.7
		353	5.0	40.1	81.2
		545	5.0	401	∞
		857	5.0	18300	∞
POLARBEAR	0.03	90	6.7	1.1	1.6
		150	4.0	1.7	2.4
		220	2.7	8.0	11.3
EPIC	0.65	30	28	0.5	0.7
		45	19	0.3	0.4
		70	12	0.2	0.3
		100	8.4	0.2	0.3
		150	5.6	0.3	0.4
		220	3.8	0.7	0.9
		340	2.5	2.2	3.2
		500	1.7	9.4	13.3
		850	1.0	740	1047

Table 5.2: Constraints on neutrino parameters for the different experiments

Experiment	Parameter	Constraint
POLARBEAR	ξ_{ν_e}	0.16 ± 0.18
	ξ_{ν_μ}	< 1.1
	m_1	< 0.23 eV
	M_ν	< 0.80 eV
PLANCK	ξ_{ν_e}	0.030 ± 0.036
	ξ_{ν_μ}	< 0.45
	m_1	< 0.084 eV
	M_ν	< 0.29 eV
EPIC	ξ_{ν_e}	0.012 ± 0.016
	ξ_{ν_μ}	< 0.29
	m_1	< 0.054 eV
	M_ν	< 0.20 eV

In this analysis, we have calculated Y_p from $\Omega_b h^2$ and the three neutrino degeneracy parameters. It is useful to look at which of these parameters drives the calculated value of Y_p. Two-dimensional likelihood plots for Y_p and the parameters it depends on (ξ_{ν_e}, ξ_{ν_μ}, and $\Omega_b h^2$) are shown in Figure 5.5. There is a strong anti-correlation between Y_p and ξ_{ν_e} that can be seen in Figure 5.5a. A correlation between Y_p and $\Omega_b h^2$ can be seen in Figure 5.5c, because the baryon density directly influences the reaction rates in BBN and hence Y_p. As a result, there is an anti-correlation between ξ_{ν_e} and $\Omega_b h^2$, which can be seen in Figure 5.5d. No correlation can be seen between Y_p and ξ_{ν_μ} in Figure 5.5b. The effect of ξ_{ν_μ} on Y_p is just too small compared to ξ_{ν_e} and Y_p to see in our simulations. That is the reason why our constraints on ξ_{ν_μ} are much worse than our constraints on ξ_{ν_e}.

5.5 Conclusions

In addition to a probe of the standard cosmological model, the CMB has become a probe of fundamental physics. It has been able to set constraints on the energy scale of inflation through constraints on r as well as limiting extensions to the standard model such as non vanishing degeneracy. While, WMAP has already

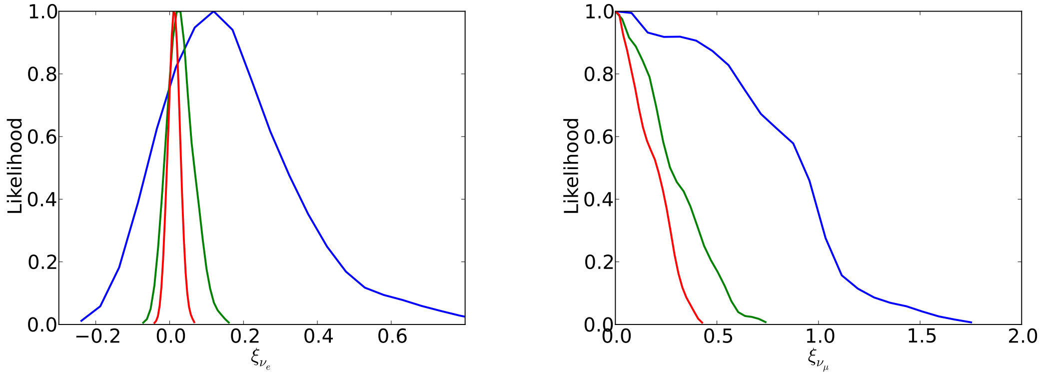

(a) Limits on ξ_{ν_e}

(b) Limits on ξ_{ν_μ}

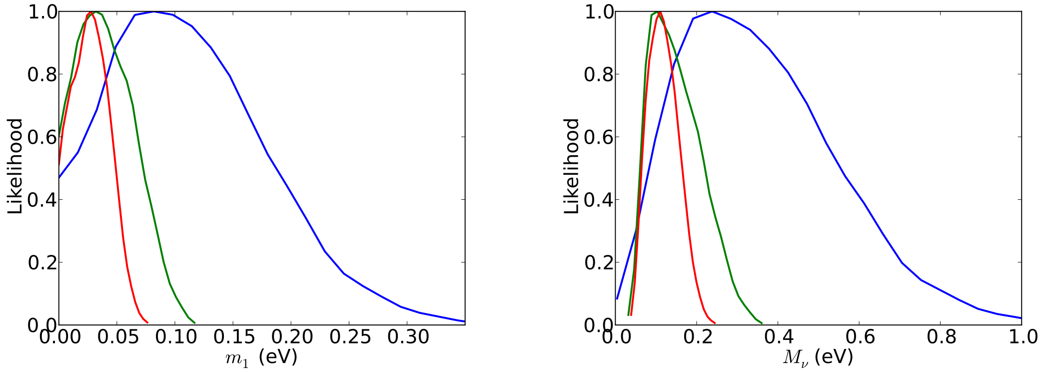

(c) Limits on m_1

(d) Limits on M_ν

Figure 5.3: Likelihoods on different neutrino parameters from the three different experiments. The blue lines is the constraint from POLARBEAR. The green line is the constraint from PLANCK. The red line is the constraint from EPIC.

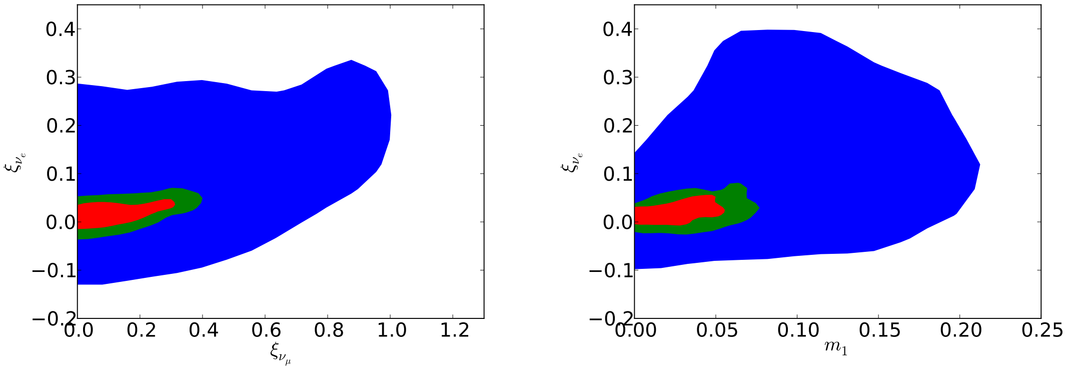

(a) $\xi_{\nu_e} - \xi_{\nu_\mu}$

(b) $\xi_{\nu_e} - m_1$

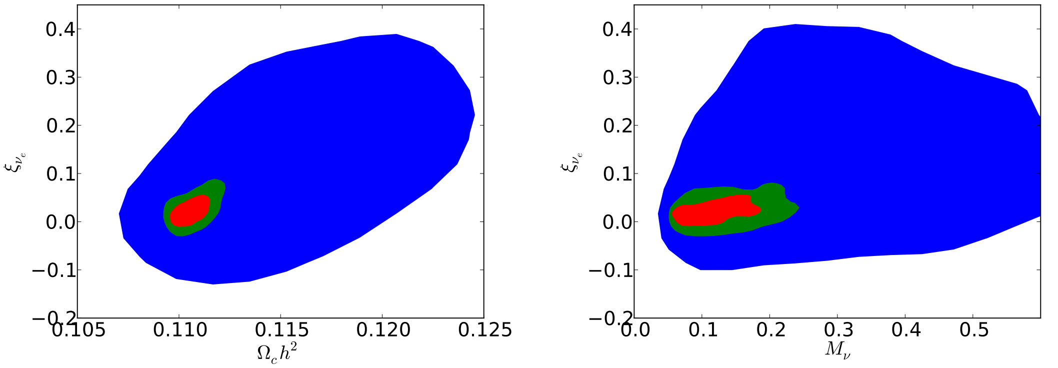

(c) $\xi_{\nu_e} - \Omega_c h^2$

(d) $\xi_{\nu_e} - M_\nu$

Figure 5.4: 2-D likelihoods for different neutrino parameter combinations. The blue contour is the constraint from POLARBEAR. The green contour is the constraint from PLANCK. The red contour is the constraint from EPIC.

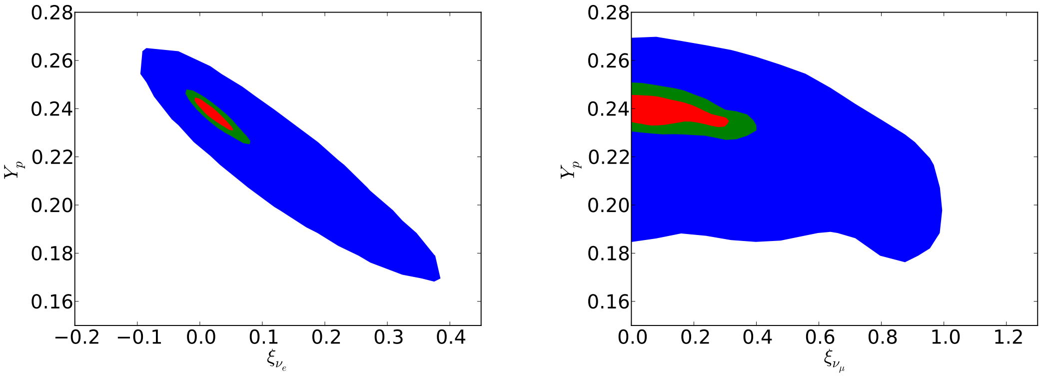

(a) $Y_p - \xi_{\nu_e}$ (b) $Y_p - \xi_{\nu_\mu}$

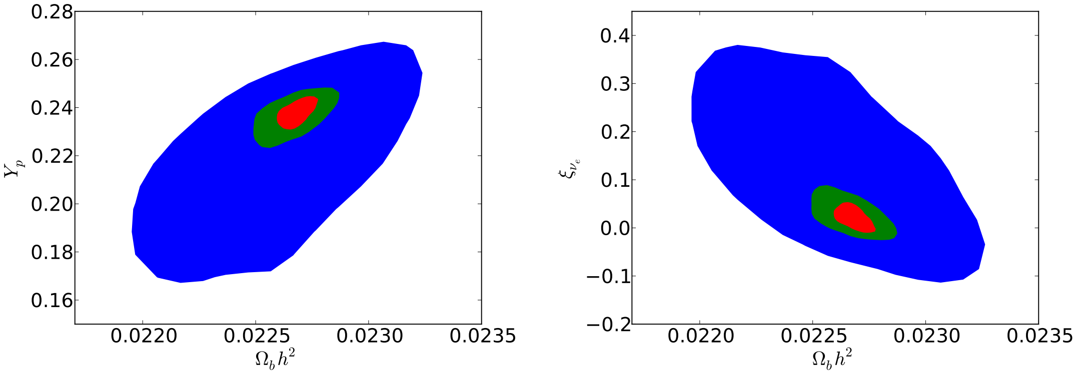

(c) $Y_p - \Omega_b h^2$ (d) $\xi_{\nu_e} - \Omega_b h^2$

Figure 5.5: 2-D likelihoods for the Y_p and the parameters that affect Y_p. The blue contour is the constraint from POLARBEAR. The green contour is the constraint from PLANCK. The red contour is the constraint from EPIC.

constrained the sum of the neutrino masses to < 1 eV, future experiments will be able to better constrain both the neutrino masses and their degeneracy parameters. Neutrinos are not directly detected, but seen through their effects on the CMB and large scale structure.

In this chapter, we looked at how the CMB is affected by the changing the neutrino mass and their degeneracy parameters, and investigated how well future experiments would be able to constrain these neutrino parameters. Our approach is unique in that we allowed each neutrino flavor to have its own independent degeneracy parameter. Normally, the degeneracy parameters for all three neutrinos are assumed to be equal. We have shown that POLARBEAR will be able to lower the constraint of the degeneracy parameters from CMB measurements alone. PLANCK and EPIC will be able to do even better because they observe the full sky. The CMB experiments have the ability to get these constraints due to their improved resolution and sesitivity. The ability to extract lensing information from the CMB data provides an extremely sensitive handle on neutrino masses and their degeneracy parameters.

Chapter 6

POLARBEAR

POLARBEAR is a CMB polarization experiment designed to search for the inflationary gravitational waves through detection of the B-mode power spectrum [92, 93]. It also has a secondary goal of mapping the lensing of the CMB due to large scale structure. This structure of this chapter is as follows. In Section 6.1, I give an overview of the experiment and its current status. In 6.2, I describe several observations we used to calibrate the telescope at Cedar Flat. In 6.3, I give conclusions about our analysis on Cedar Flat data. In 6.4, I describe the future plans for the POLARBEAR experiment.

6.1 Overview

The POLARBEAR receiver resides on the Huan Tran Telescope (HTT) which is located at the James Ax Observatory in the Atacama desert in Chile. The HTT is an off-axis Gregorian-Dragone telescope and has been designed to precisely control of systematic effects. The POLARBEAR focal plane consists of seven wafers with each wafer having 91 pixels (182 TES bolometers), giving a total of 637 pixels (1274 TES bolometers) in the experiment. The photons are coupled to the bolometers through a double slot dipole antenna. Each bolometer will have a sensitivity of NET $\approx 360\mu\mathrm{K}\sqrt{\mathrm{s}}$ and a beam FWHM of $\approx 4'$.

The expected errorbars on measurements of the EE and BB power spectrum for POLARBEAR are shown in Figure 6.1. We show the error bars on the

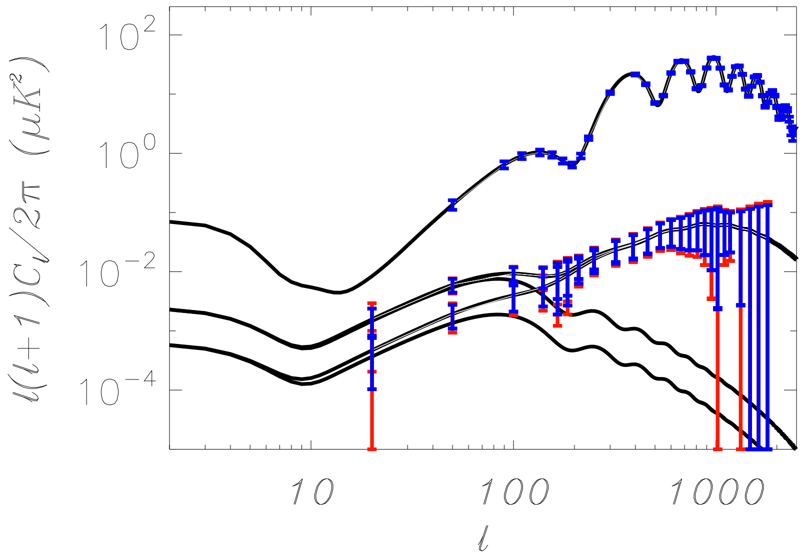

Figure 6.1: A plot of predicted measurements to the EE and BB power spectra for $r = 0.1$ and $r = 0.025$ from POLARBEAR. Also shown is the BB power spectrum due to lensing. The blue error bars are generated from the raw sensitivity of POLARBEAR from 1.5 years of observation. The red error bars are generated when we account for foregrounds. We use FDS model 8 [3] with the assumption of 5% polarizion. We assume there is foreground subtraction and add 10% of the predicted foreground as an extra source of noise.

power spectra from the raw sensitivity of POLARBEAR and from a simulation of foreground subtraction. With POLARBEAR, we can expect to detect $r = 0.025$ at 2σ confidence. As can be seen from the figure, we will also be able to measure the lensed B-modes over a large range over angular scales. In addition, we will be able to make a significant detection of the power spectrum of the lensing potential.

In the summer of 2010, POLARBEAR was deployed to the CARMA site at Cedar Flat in California. The deployment was used as an engineering run to test the performance of the experiment. The choice of location at Cedar Flat was due to the existing infrastructure at the CARMA site and the location which is within driving distance for the collaborators in Berkeley and San Diego. The

Figure 6.2: A aerial photograph of the HTT along with the CARMA telescopes at Cedar Flat in the Inyo Mountains of California. This was taken by Prof. Brian Keating during its 2010 engineering run. The HTT is located inside the black circle.

HTT was constructed at Cedar Flat in the summer of 2009. The receiver was first deployed to the telescope in April 2010 with first light coming on April 18, 2010. We observed with POLARBEAR until August 22, 2010 when it was taken down in preparation for its move to Chile. An aerial photograph of the HTT at Cedar Flat is shown in Figure 6.2. The HTT is located at the center of the image (surrounded by the black circle). The other telescopes seen in the photo are the telescopes that make up the Combined Array for Research in Millimeter-wave Astronomy (CARMA). In Figure 6.3, we see a photgraph of the POLARBEAR receiver as it is being removed from the HTT at the end of the engineering run.

The focal plane consisted of three wafers which were named 8.2.0, 8.2.1, and KT8. We only had enough readout electronics for two wafers as the Cedar Flat deployment was originally only going to have two wafers in the focal plane, so several pixels on wafer 8.2.1 were not connected to any readout electronics. These

Figure 6.3: A photo taken by Prof. Brian Keating of the POLARBEAR receiver as it is being removed from the HTT at the end of the 2010 engineering run.

electronics were instead connected to several pixels on wafer KT8.

The telescope has been reassembled in the Atacama desert in Chile. This location was chosen for its high altitude and dry weather. Ground based telescopes, such as POLARBEAR, must observe through the atmosphere which contaminates the signal. A high altitude and dry weather limits the atmospheric emission that is detected and improves the sensitivity of the experiment compared to a lower altitude and wetter site. The Atacama desert site also provides sky rotation. In order to measure the polarization of the CMB, we must observe the sky using several different orientations of our pixels. This is done automatically when we observe the same point on the sky at different times as the sky rotates. The South Pole, which is one of the only places better than the Atacama desert in terms of altitude and dryness, is at a pole and there is no sky rotation.

6.2 Calibration

In order to make any measurements of the CMB, we must calibrate the telescope. If we do not properly calibrate the telescope, then systematic effects, such as the beam systematics described in Chapters 2 and 3, will contaminate our results. We must also calibrate the telescope in order to make any physical measurements. There are many different calibrations that must occur before we can begin CMB observations. We must focus the telescope. We must have a pointing model so we know where the boresight is pointing at all times. Given the location of the boresight, we must know where each bolometer is pointing on the sky and the polarization orientation of each bolometer. We must also know the shapes of the beam for each pixel. The timestream of a bolometer is recorded in generic ADC counts, and so we must know the relation between an ADC count and change in polarized and unpolarized intensity. In this we will describe the procedure used to make maps of the beams for the different bolometers, which were used to determine the shapes and location of the beams. We will also discuss and show results for an expansion of a beam over Hermite-Gauss polynomials and how we focused the telescope using beam measurements.

6.2.1 Beam Maps

To measure our beams, we make observations of a point-like source. We need to observe an object that is large enough that we can resolve in our beams with a high signal-to-noise and small enough so that maps of the object are maps of our beams. Planets are a good choice to use as a source. At Cedar Flat, we observed the planet Jupiter to make maps of our beams. Jupiter's apparent diameter as seen from Earth is $\approx 45''$, which is smaller than our beams that have a FWHM of $4'$. We therefore can model it as a point source when we map our beams. In order to map Jupiter, we first had the telescope track Jupiter. While tracking Jupiter, we rastered the telescope in elevation while scanning in azimuth. A plot of the raster scan is shown in Figure 6.4. Each raster scan consisted of scanning both up and down in elevation so each offset is scanned over twice and we finished at the same place we started with respect to Jupiter. Several of these raster scans starting at different elevation and azimuth offsets from Jupiter were run back to back in order to map every bolometer in the focal plane. Before and after each raster scan we did a short elevation scan, or "el nod", that is used to determine the relative gain between bolometers. We do not use the data from the el nods when mapping the beams. After each raster scan the bolometers were re-nulled. This is a process that moves the measured signal to zero ADC counts, but does not change the relation between an ADC count and change in temperature. The bolometer timestreams are stored as a 2-byte integer (0 to ± 32767). If we do not re-null, then changing elevation and atmospheric conditions can cause the measured ADC count to overload.

We cannot fit to the beam parameters from the raw timestream. A plot of the raw timestream for a single bolometer is shown in Figure 6.5. This timestream consists of 11 raster scans. The atmosphere can clearly be seen to drift over each raster scan. The large negative signal after each raster scan is an artifact of the re-nulling process. In order to measure of the beams, we must remove this atmospheric signal. To remove the atmosphere we first break the timestream into halfscans. A halfscan is defined as a continuous period where the telescope is scanning at constant velocity in azimuth. Since all the el nods and re-nulling do not occur

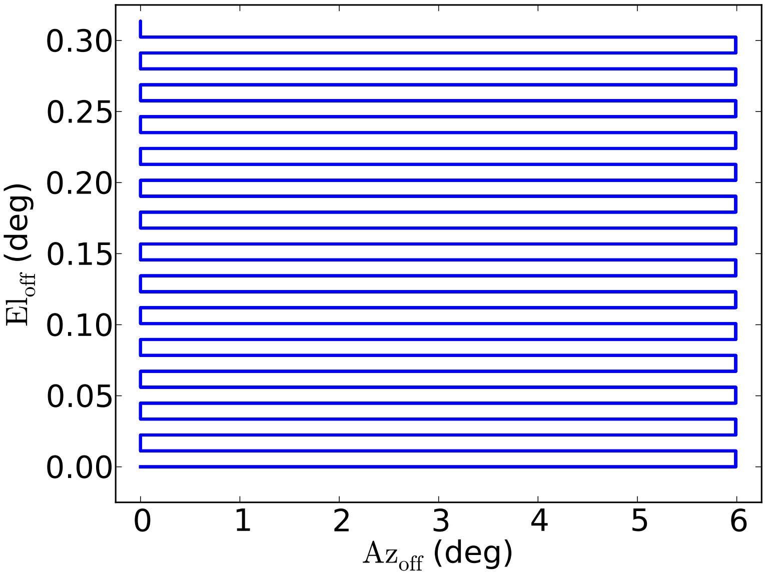

Figure 6.4: A plot of a single raster scan. The start and end of the scan is at the origin.

during a halfscan we can set the signal during those times to be zero to make the filtered timestreams look prettier. We do not fit to points outside of the halfscans so it does not matter that we set the values to zero. We then subtract the best fit 7th order polynomial from each halfscan to remove the atmospheric fluctuations. The planet is masked before we fit to the 7th order polynomial so we do not fit to the large change in signal due to the planet. A plot of the filtered timestream is shown in Figure 6.6. We can then fit the signal during each halfscan and within 15′ of Jupiter to an elliptical gaussian model described by

$$S(x,y) = Ae^{-\frac{x'^2}{2\sigma_{x'}^2} - \frac{y'^2}{2\sigma_{y'}^2}} \tag{6.1}$$

where x' and y' are defined as

$$\begin{pmatrix} x' \\ y' \end{pmatrix} = \begin{pmatrix} \cos\psi & \sin\psi \\ -\sin\psi & \cos\psi \end{pmatrix} \begin{pmatrix} x - x_0 \\ y - y_0 \end{pmatrix} \tag{6.2}$$

and x and y are projections of $\mathrm{az_{off}}$ and $\mathrm{el_{off}}$ to flat space: $x = \mathrm{az_{off}} \cos \mathrm{el_{off}}$ and $y = \mathrm{el_{off}}$. Each bolometer is fit to a model with six free parameters: A, x_0, y_0, $\sigma_{x'}$,

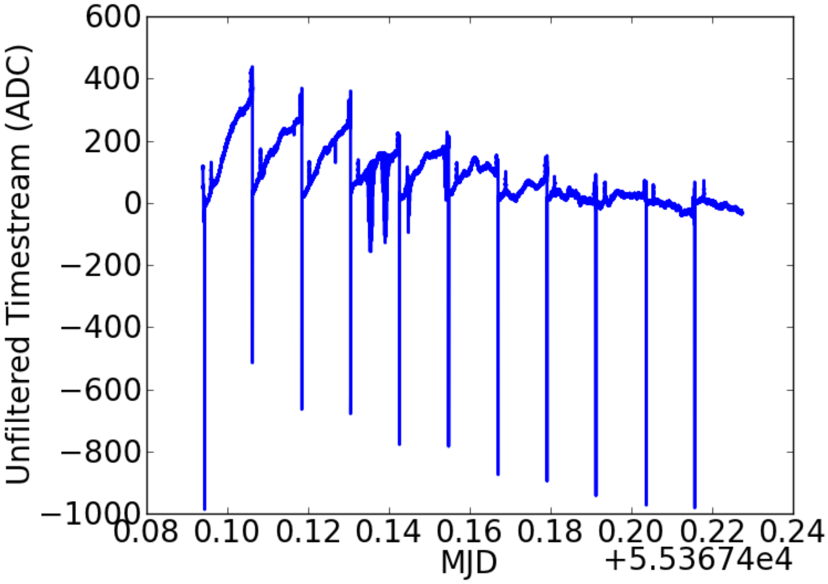

Figure 6.5: A plot of the raw unfiltered timestream for a single bolometer during an observation of Jupiter. The periodic spikes are due to motion of the telescope.

$\sigma_{y'}$, ψ.

We can apply this process to fit to every active bolometer. A map of the focal plane from a Jupiter observation on June 19, 2010 is shown in Figure 6.7. The bottom wafer is wafer 8.2.0. The top wafer is wafer 8.2.1. The two pixels off to the right are from wafer KT8. The electronics that were used to read out the pixels on KT8 would have been used to read the set of pixels in the middle and bottom of 8.2.1. The offsets are the offset that we must apply to the boresight center in order to see Jupiter in that bolometer. This means the figure is a mirror image from what you would see if you looked at the focal plane from the cryostat window. A positive y-offset means the bolometer is below the boresight center.

Using the fitted beam positions we can make a coadded beam map from all the active bolometers in Cedar Flat. This is shown in Figure 6.8. The coadded beam is not a perfect elliptical gaussian. It has a slight triangular shape, plus in a few areas the signal is not decreasing as you get farther away from the center of the beam. This had been predicted for POLARBEAR and the HTT by simulations

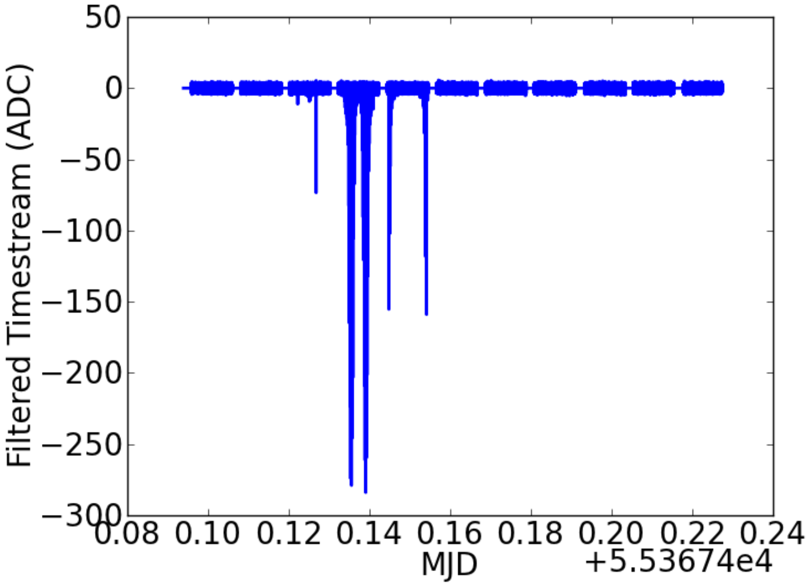

Figure 6.6: A plot of the filtered timestream for a single bolometer during an observation of Jupiter. Every point that is not a part of a halfscan is set to zero.

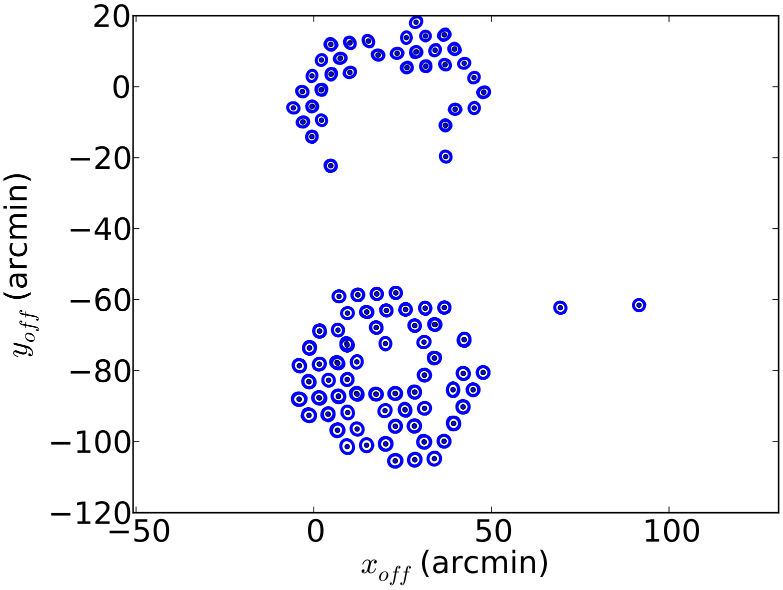

Figure 6.7: A plot of the location on the focal plane for all the active bolometers in the engineering run at Cedar Flat. Plotted are the fitted centers plus an ellipse showing the 1σ width of each beam.

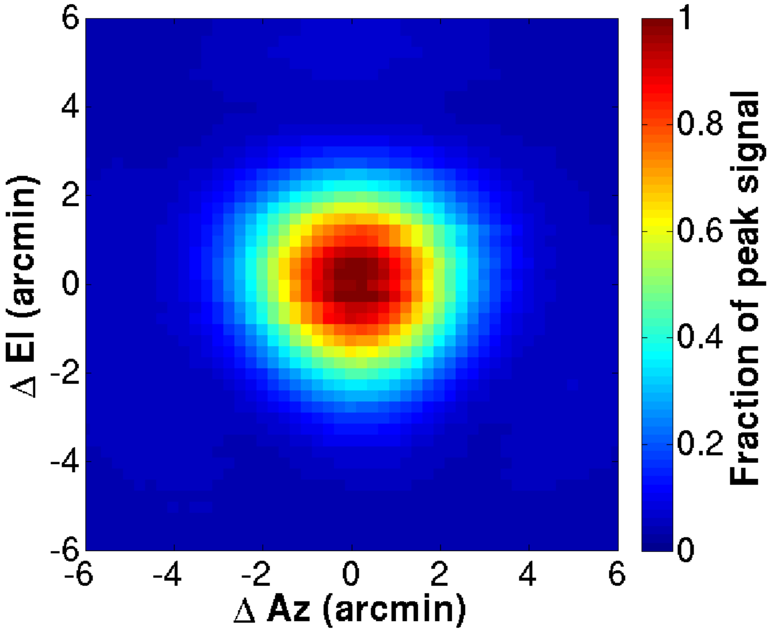

Figure 6.8: A plot of the coadded beam map from all ≈ 170 active bolometers in Cedar Flat.

using Zemax, a program used for the design and analysis of optical systems.

In Chile, we we will have seven wafers insead of three and we will redo the beamfitting. We will observe Jupiter with the whole focal plane and make beam maps multiple times throughout our deployment. This will allow us to determine how the beam positions and shapes change over time.

6.2.2 Beam Expansion

The observed CMB power spectra is a product of the real CMB power spectra and the power spectra of the beam. In order to make accurate predictions about the real CMB power spectra, we must know more about our beams than what we extract in our beam fits. An elliptical gaussian is not the best model for our beams. A plot of the difference between the simulated timestream for the elliptical gaussian fit and the real timestream is shown in Figure 6.9. An elliptical gaussian model does not accurately represent the beam. You can draw

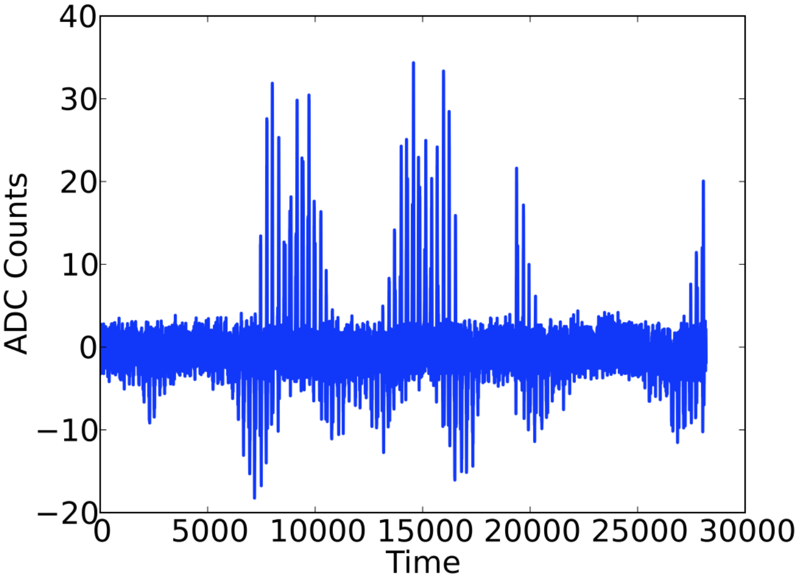

Figure 6.9: A plot of the difference between the real timestream and the simulated timestream from the elliptical beam fit

this conclusion by just looking at the coadded beam map in Figure 6.8.

We can get a better approximation of the beam by expanding it over a complete set of basis functions. We want to choose a set of basis functions such that most of the power will be in the lowest order functions. We will choose to use Hermite-Gauss functions. This was done for PLANCK [97] and we will follow the exact same procedure here. The Hermite-Gauss functions are written as

$$\Phi_{n_1 n_2}(\mathbf{x}) = \frac{H_{n_1}(x'_1)H_{n_2}(x'_2)}{\sqrt{2^{n_1+n_2} n_1! n_2!}} \exp(-\mathbf{x}' \cdot \mathbf{x}'/2) \tag{6.3}$$

where H_n is the Hermite polynomial of order n. This is a 2-dimensional problem and the two indices correspond to two orthogonal directions. The best-fit elliptical gaussian parameters are encoded in the transformation as

$$\mathbf{x}' = \begin{pmatrix} \sigma_x^{-1} & 0 \\ 0 & \sigma_y^{-1} \end{pmatrix} \mathbf{R}^{-1}(\psi)(\mathbf{x} - \mathbf{x_0}). \tag{6.4}$$

This transformation offsets, rotates, and scales the axes so that the best-fit elliptical gaussian is mapped to a set of axes where it is a circular gaussian with $\sigma = 1$. These functions are a good choice as Φ_{00}, the lowest order term, is the best-fit elliptical gaussian. Most of the power in the beam will be in this term in the expansion. Higher order terms have fluctuations on smaller scales. These fluctuations will be of smaller order than the fluctuations in our beam. Therefore, we can cutoff our expansion at $n = n_{\max}$ and we will approximate our beam better than an elliptical gaussian fit. A larger $n_{\max}$ will result in a better approximation.

We can expand the beam as

$$B(\mathbf{x}) = \sum_n s_n \Phi_n(\mathbf{x}). \tag{6.5}$$

where we can re-index the eigenmodes as

$$n = \frac{(n_1 + n_2)^2 + n_1 + 3n_2}{2}. \tag{6.6}$$

With this reindexing, the modes satisfying $n_1 + n_2 = N$ are all mapped to a smaller n than any modes satisfying $n_1 + n_2 = N + 1$. With the normalization defined in Eq. 6.3, the maximum of the ground state is unity, and the orthogonality relation is

$$\int d^2x \Phi_m(\mathbf{x}) \Phi_n(\mathbf{x}) = \pi \sigma_x \sigma_y \delta_{mn}. \tag{6.7}$$

To recover the basis coefficients s_n, we must integrate

$$s_n = \frac{1}{\pi \sigma_x \sigma_y} \int d^2x \Phi_n(\mathbf{x}) B(\mathbf{x}). \tag{6.8}$$

POLARBEAR discretely samples the sky instead of continuously sampling so the integral must be turned into a sum

$$\int d^2x (\ldots) \approx \frac{A}{N} \sum_i (\ldots), \tag{6.9}$$

where A is the area of the sampled area and N is the number of detector samples. When observing the sky, we do not sample the full sky evenly. The orthogonal functions will only be approximately orthogonal when we sum over all samples. If we do not correct for this, then our estimates for the beam coefficients will be biased.

We address the sampling issue by computing an overlap matrix

$$I_{mn} = \frac{1}{\pi \sigma_x \sigma_y} \frac{A}{N} \sum_i \Phi_m(\mathbf{x}_i) \Phi_n(\mathbf{x}_i). \tag{6.10}$$

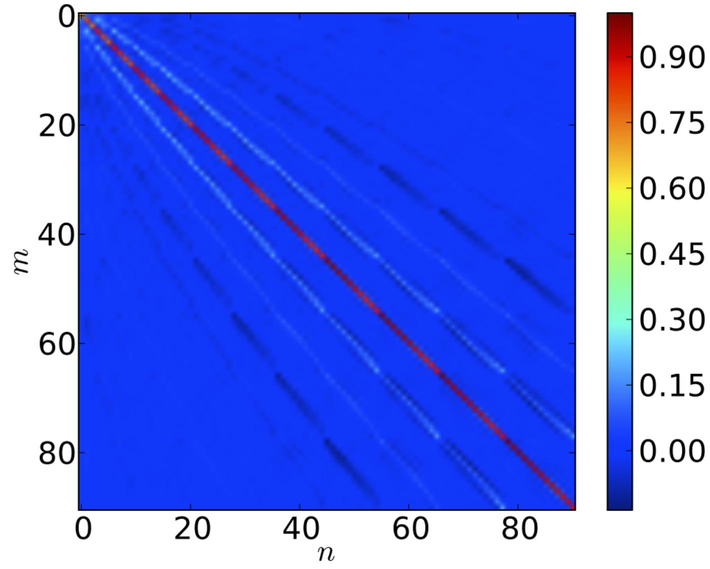

Figure 6.10: A plot of the overlap matrix, I_{mn}, for an observation at Cedar Flat. The color represents the value of I_{mn}. It is normalized to a maximum value of unity. The matrix was calculated for $n_{\max} = 90$, which corresponds to all terms satisfying $n_1 + n_2 \leq 12$.

Using the overlap matrix, we can then calculate an unbiased estimate for the basis coefficient

$$\hat{s}_m = \sum_n I^{-1}_{mn} \frac{1}{\pi \sigma_x \sigma_y} \frac{A}{N} \sum_i \Phi_n(\mathbf{x}_i) d_i, \tag{6.11}$$

where d_i is the timeordered data at position $\mathbf{x}_i$.

When we expand over the basis functions, we must choose a $n_{\max}$ at which we will stop the expansion. We will usually choose to calculate the coefficients for all terms satisfying $n_1 + n_2 \leq N$ for different values of N.

The overlap matrix for an observation of Jupiter from Cedar Flat is shown in Figure 6.10. The diagonal elements are nearly unity, while the off-diagonal elements range between -0.15 and 0.15. If we did not correct for non-uniform sampling, our results would be incorrect.

A plot of s_n for a single bolometer is shown in Figure 6.11. Since the beam is fairly well approximated by an elliptical gaussian, the largest coefficient is s_0. The

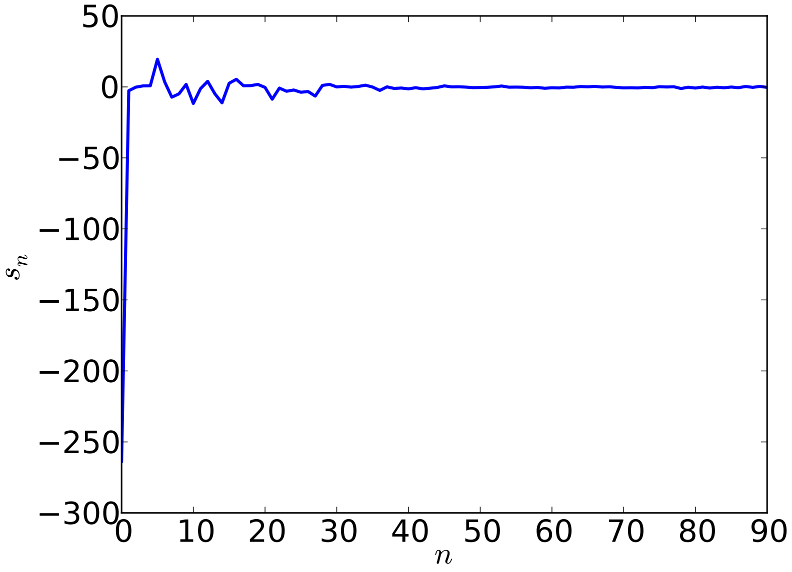

Figure 6.11: A plot of the coefficients, s_n, in the Hermite-Gauss expansion as a function of n. The coefficients were calculated out to a $n_{\mathrm{max}} = 90$, which corresponds to all terms satisfying $n_1 + n_2 \leq 12$.

rest of the terms are close to zero and are used to add corrections to the elliptical gaussian that help us better approximate the beam. A larger n corresponds to smaller scale fluctuations. The coefficients tend towards zero as we will eventually be looking at terms that quantify smaller scale fluctuations that what is in our beam.

A comparison of a simulated timestream for the beam expansion versus the real timestream is shown in Figure 6.12. There are three different simulated timestreams plotted in Figure 6.12a. We plot the real timestream, the simulated timestream from the expansion up to $n_{\mathrm{max}} = 90$, and the simulated timestream from the elliptical gaussian fit. It is impossible to see if the Hermite-Gauss expansion improves the fit, so in Figure 6.12b we plot the difference between the real timestream and the two different simulated timestreams. From the difference timestreams, it is easy to see that the expansion reproduces the real timestream much better than the elliptical gaussian fit. To get a quantitative measurement of

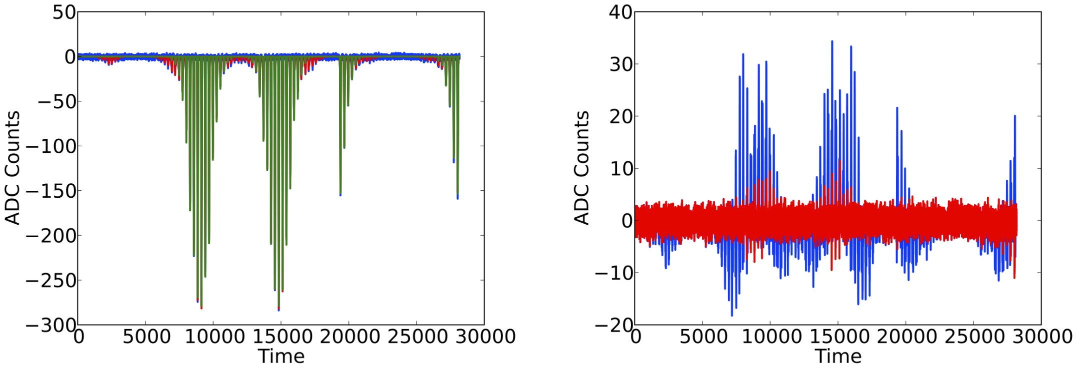

(a) Timestreams

(b) Difference in Timestreams

Figure 6.12: A comparison of the real versus simulated timestreams. a) The blue line is the real timestream. The red line is the simulated timestream from the expansion up to $n_{\max} = 90$. The green line is the simulated timestream from the elliptical gaussian fit. b) The blue line is the difference between the real and the elliptical gaussian fit. The red line is the difference between the real and the expansion up to $n_{\max} = 90$.

this, we can calculate the reduced χ^2 value . A plot of the reduced χ^2 as a function of $n_{\max}$ is shown in Figure 6.13. The elliptical gaussian fit has $\chi^2_{\text{red}} = 8.11$, while expanding up to $n_{\max} = 90$ results in $\chi^2_{\text{red}} = 1.52$, and $n_{\max} = 860$ gives $\chi^2_{\text{red}} = 1.23$. The noise for this calculation is calculated as the standard deviation of the timestream when we are $> 15'$ away from the center of the beam.

Expanding the beam over Hermite-Gauss functions indeed improves the reconstructed timestream. We are able to measure our beam, convert it to ≈ 95 parameters, and reconstruct the beam very well, however our knowledge of the beam is still not perfect. The next step is to determine the bias is the power spectrum due to our imperfect knowledge of the beam caused by limiting the number of basis functions for beam reconstruction. That calculation is ongoing.

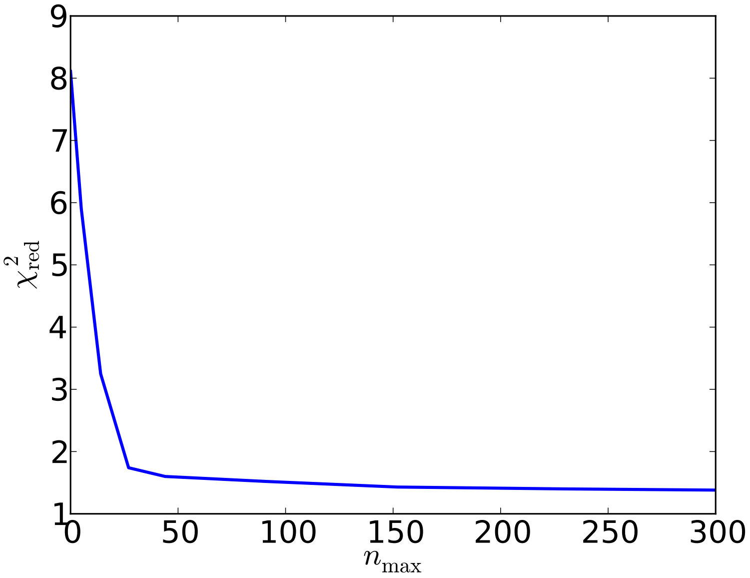

Figure 6.13: A plot of χ^2_{red} as a function of n_{max}. This is calculated from the simulated and real timestreams.

6.2.3 Focusing

Beam fits are used to focus the telescope. If the telescope is out of focus then the beams can be highly elliptical. There are several different ways of focusing the telescope, both in the way of taking data and the modifications to the telescope. In this section, the analysis was done on the ellipticity and beam size of the active bolometers in POLARBEAR, while in order to put the telescope into focus, we moved the location of the receiver. Jupiter observations for focusing the telescope were done on May 5, 6, 12, 19, and 22, 2010.

Using the Jupiter measurements on May 5, 6, and 12, we predicted the how we should move the receiver in order to focus the telescope. A plot of the mean ellipticity as a function of the receiver position in Figure 6.14. The blue line is the quadratic fit to the 3 measurements. The minimum of the ellipticity is predicted to occur at $z = 8.5$ mm. Additional fits were done to the mean of the mean FWHM and the FWHM of the coadded beam maps. The mean FWHM predicted a movement of ≈ 7.7 mm, while the FWHM of the coadded beam maps predicted

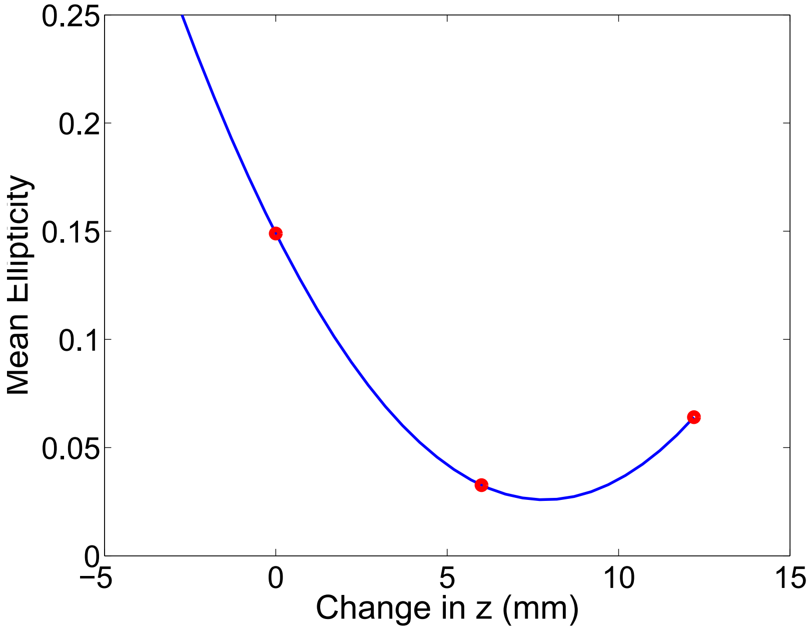

Figure 6.14: The red dots are the mean ellipticity as a function of the receiver position. The data for the 3 positions were taken on May 5, 6, and 12. The blue line is the quadratic fit to the red dots.

a movement of 8 mm. We chose to move 8.5 mm as we were initially considering a move of 9 mm. Because we did not have a pointing model, we noticed a shear between wafers 8.2.0 and 8.2.1 on the May 19 measurements. we eventually moved back to the May 6 position, which is $z = 6.2$ mm, and data was retaken on May 22. The persistance of the shear in the May 22 data, and the fact that a single bolometer had two different positions when it was mapped at different times of the day. The receiver was roughly in the focus position given the optical models so it was left at its May 6 position for the rest of the Cedar Flat observations. For Chile, it is expected that we will determine a pointing model before attempting to focus the telescope. The focusing efforts should therefore be more successful.

6.3 Conclusion

POLARBEAR had a very successful engineering run at Cedar Flat in the Inyo mountains in 2010. We were able to calibrate our telescope and show that it meets performance requirements for Chile. We made measurements of the beams by observing Jupiter. We were able to see begin analysis of our beams and make sure that they meet design expectations. Beam systematics will not limit our detection of r in Chile.

6.4 Future Plans

POLARBEAR and the HTT are currently deployed in Chile for its CMB observations. It will begin observations in late 2011 and observe for 3 years.

In 2014, the cryostat will be replaced by a second receiver that is currently in development. The focal plane in this cryostat will feature planar, sinuous antennas compared to the double slot dipole antennas currently in POLARBEAR. These antennas will be sensitive to multiple frequency bands so we can observe at both 90 GHz and 150 GHz in a single pixel. Each frequency band will have two associated bolometers corresponding to the two orthogonal polarizations giving a total of four bolometers per pixel. This experiment is POLARBEAR-II.

POLARBEAR will eventually be extended to multiple telescopes. Each telescope will be a replica of the HTT and the receivers will be POLARBEAR-II type receivers. Some receivers will hold antennas that are sensitive to 90 and 150 GHz, while some antennas will be sensitive to 150 and 220 GHz. This will give us even more sensitivity to foregrounds and allow foreground removal without having to use data from other experiments. This will be called POLARBEAR-Extended.

Chapter 7

Cosmological Birefringence and BICEP

Background Imaging of Cosmic Extragalactic Polarization (BICEP) is a polarimeter that observed the CMB from the South Pole for three years (2006-2008). The characterization of the telescope and analysis of the first two years of data were initially published in 2009 [10, 98]. Later in 2009, Xia, Li, and Zhang published a paper in which they claim a $2.5 - 3\sigma$ detection of cosmological birefringence from measurements of the TB and EB power spectra in the BICEP data. These two power spectra should be zero in the standard cosmological model [99]. In Section 7.1, we will first give an introduction to the jackknife technique used during our analysis. In Section 7.2, we will look at the claim of detection through power spectra constructed from data in different frequencies. In Section 7.3, we will analyze the jackknife power spectra BICEP uses to test whether it has accounted for systematics. Finally, in Section 7.4, we will analyze results from simulations that take into account different beam systematics. In Section 7.5, we will give some conclusions based on our analysis of the BICEP data.

7.1 Resampling using the Jackknife Technique

While analyzing the BICEP three year data, we employed a statistical resampling technique known as the jackknife. The process was first proposed by

M.H. Quenouille in 1956 [100] and expanded upon by Tukey in [101]. A more general review of the technique can be found in [102, 103, 104]. The jackknife is used to remove biases in measured data. The idea is that our estimator for the cosmological birefringence angle α, $\hat{\alpha}$, is biased to some degree because of systematics leaking into a small number of bins in our power spectra. For estimates of the power spectra with n bins, we say that

$$\hat{\alpha} = \alpha + \frac{c_1}{n} + \frac{c_2}{n^2} + \dots \tag{7.1}$$

where $\hat{\alpha}$ is our estimator for α, the true, underlying cosmological birefringence angle, and c_1, c_2 are constant bias values. By resampling, we can remove these biases.

The process of removing the biases consists of removing a single data point, in our case a single bin from our measured power spectra, and then refitting for α. We do this for all measured bins in our power spectra. The bias is amplified when we fit to fewer data points. We can use the differences in the fits to estimate the bias and the uncertainty in the measurements. The first order jackknife can be used to remove the $1/n$ bias in the dataset, while the second order jackknife, which uses fits when we remove two measured bins, can also remove the $1/n^2$ bias.

We will describe the process for the first and second order jackknife procedure here. If we let $\hat{\alpha}$ be the fit to the cosmological birefringence angle to the full data set, α_{-i} represent the fit if we remove ith bin from the dataset, and α_{-ij} represent the fit if we remove the ith and jth bin from the dataset, then we can then define

$$\begin{aligned}
\alpha_i &= n\hat{\alpha} - (n-1)\alpha_{-i} \\
\alpha_{ij} &= \frac{1}{2}\left[n^2\hat{\alpha} - 2(n-1)^2\alpha_{-i} + (n-2)^2\alpha_{-ij}\right] \\
J(\alpha) &= \frac{1}{n}\sum_i \alpha_i \\
J^{(2)}(\alpha) &= \frac{1}{n(n-1)}\sum_{i\neq j} \alpha_{ij} \\
\sigma_\alpha^2 &= \frac{n-1}{n}\sum_i \left(\alpha_{(-i)} - \hat{\alpha}\right)^2
\end{aligned} \tag{7.2}$$

then $J(\alpha)$, the first order jackknife, is the estimate for α with the $1/n$ bias removed, $J^{(2)}$, the second order jackknife, is the estimate for α with the $1/n$ and $1/n^2$ biases removed, and σ_α^2 is an estimate for the variance on α from the jackknife procedure. The equations for the first and second order jackknifes are taken from [100, 102].

7.2 Power Spectra at Different Frequencies

BICEP observed the sky at primarily two frequencies: 100 GHz and 150 GHz. Two 220 GHz pixels were used as foreground monitors. The published data are a combination of the two lower frequencies, however maps of the sky and power spectra can be extracted from each of these frequencies separately. From these observations in two frequencies, we can produce four sets of power spectra. We can auto-correlate the 100 GHz and 150 GHz with themselves, which we will call the 100 and 150 GHz spectra, respectively. We can also cross-correlate the 100 GHz data with the 150 GHz data in two different ways. For example, in the TB power spectra, we can take the temperature data (T) from 100 GHz, while taking the B-mode polarization data (B) from 150 GHz, or we can take the temperature data from 150 GHz observations and the B-mode polarization data from the 100 GHz observations. We will call these spectra the “cross” and the “alt-cross” or “alt” power spectra. For the simplest model of birefringence claimed by Xia et. al. in [99], we expect to measure the same cosmological birefringence angle in all four frequency combinations and in both the TB and the EB power spectra. Plots of

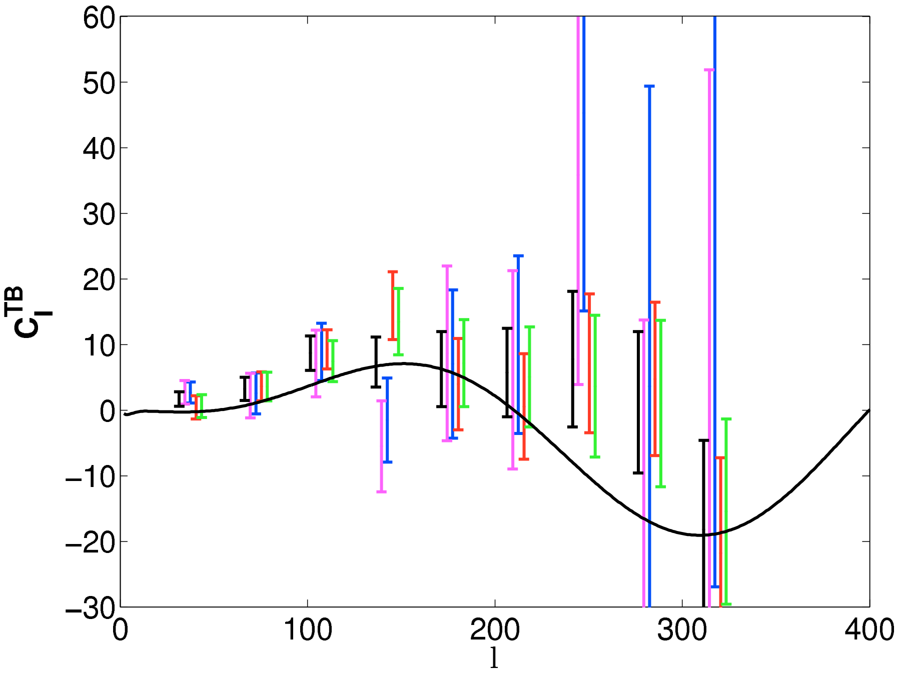

Figure 7.1: Plots of the TB power spectra from all the different datasets. The 100 GHz data is blue. The 150 GHz data is red. The cross data is green. The alt-cross data is magenta. The black data is the combined dataset. The black line is the best fit C_ℓ to the combined dataset.

these spectra can be seen in Figures 7.1 and 7.2.

We looked at the 3-year BICEP data plus results from simulated data. For each frequency combination we compared the χ^2 under the null hypothesis measured in the real data to the simulated data. We calculated a probability-to-exceed (PTE) based on the number of times a simulated data set had a larger χ^2 than the real BICEP data. A smaller PTE means that it is less likely that the null hypothesis, of zero CB angle, is true. A table of the calculated PTEs is shown in Table 7.1. The detections of a non-zero α all come from the TB power spectra where the B is taken from the 150 GHz data. When the B is taken from the 100 GHz data, it is consistent with the null hypothesis. It is likely that there is some systematic affecting the B power spectra at 150 GHz that is causing this detection.

In Table 7.2, we show the results from applying the 1st order jackknife resampling technique to the different power spectra. Unfortunately, the results are

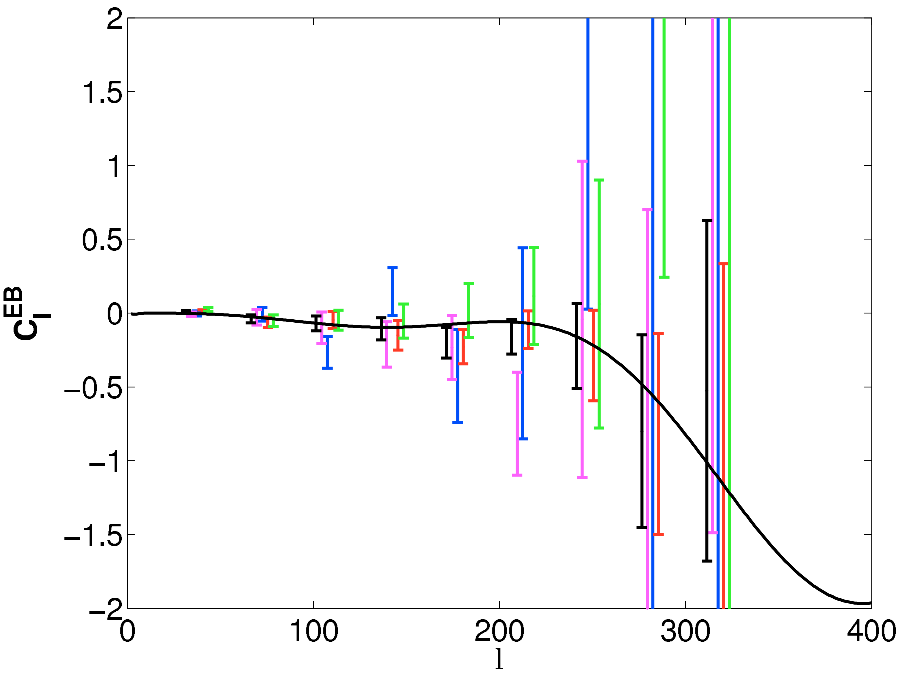

Figure 7.2: Plots of the *EB* power spectra from all the different datasets. The 100 GHz data is blue. The 150 GHz data is red. The cross data is green. The alt-cross data is magenta. The black data is the combined dataset. The black line is the best fit C_ℓ to the combined dataset.

less clear than those from the PTEs. There is a detection of non-zero α in the alt-cross EB power spectra, however there is still reason to believe that the detections are due to systematics as the results between each frequency combination and power spectra are not consistent with each other.

7.3 Experimental Jackknife Power Spectra

A way to test for systematics in the observed data is to split the data into two separate sets that should give the same results and then difference the resulting maps. The power spectra constructed from these maps should all be consistent with zero in all six power spectra, unless there is some systematic contaminating the results. They are null tests. These are the experimental "jackknife" power spectra. It is a simple derivative of the statistical Quenouille jackknife technique described in Section 7.1 where there are only two data points and we are testing whether the two data points are consistent with each other. If the data are not consistent with each other, then we must not be accounting for some systematic in the analysis.

BICEP generates six different experimental jackknife spectra. "Jackknife 1" is a deck angle jackknife. BICEP has the ability to rotate its cryostat, and hence its focal plane, while keeping the telescope az and el angles fixed. The angle describing the orientation of the focal plane is the deck angle. This jackknife is formed from different orientations of the focal plane. "Jackknife 2" is a scan directions jackknife. When the telescope scans, it moves in both the positive and negative azimuth directions. Maps made from only positive az direction half scans and from only negative az direction half scans are differenced. "Jackknife 3" is generated from comparing the maps made from the first two seasons (2006 and 2007) and the third season (2008) of observations. "Jackknife 4" is a Q/U focal plane jackknife. Half the pixels in the focal plane are rotated by 45° relative to the other pixels. If one half is sensitive to the Q Stokes parameter, then the other half is sensitive to the U Stokes parameter. The maps made with "Q" pixels and the maps made with the "U" pixels are differenced. "Jackkknife 5" is an elevation coverage jackknife. BICEP covers an elevation range of 55° to 60°. It covers this range over two sets of 9 hour blocks of observations, each covering half of the elevation range. Over a single 48 observation cycle, this is done twice. In the first two 9 hour blocks the lower half of the elevation range (55° to 57.5°) is mapped first, while in the second two 9 hour blocks, the upper half of the elevation range (57.5° to 60°) is mapped first. These two sets of two 9 hour blocks, each covering the full elevation range, are differenced to generate the el coverage jackknife. The scan strategy is described in more detail in [98]. "Jackknife 6" is a frequency jackknife. The maps from the two different frequencies (100GHz and 150GHz) are compared and differenced.

The fitted α, 1st order jackknife, 2nd order jackknife, and the signal-to-noise ratio are shown in Table 7.4. The uncertainties shown in this table are σ_α as calculated in Eq. 7.2 and therefore may vary slightly if calculated through the likelihood function. There are only three combinations that result in $S/N > 3$ or $J_2(S/N) > 3$. We chose a signal-to-noise of greater than three as that is around the size of the alleged detection of CB in the BICEP data and corresponds to a 99.8% confidence probability. The three combinations are the deck-angle jackknife alt-cross TB power spectra, the split-season cross TB power spectra, and the split-season alt-cross TB power spectra. Again, detections are only seen in the TB power spectrum. A comparison of the χ^2 under the null hypothesis to simulations is shown in Figure 7.3. A plot of the fitted α for both the real data and simulated data is shown in Figure 7.4. The deck-angle jackknife, alt-cross TB power spectrum is the only one we can consider to "detect" a non-zero α. Its χ^2 is much larger than any of the simulations and it measures an α that is much larger than any of the simulations. It can be considered a failed jackknife. The split-season jackknife, cross TB spectra marginally detects a non-zero α, while the split-season jackknife, alt-cross TB spectra shows no evidence of a non-zero α in either of the figures. The fact that only 3 of the 42 tests showed a $S/N > 3.0$ can be considered a statistical fluctuation. If we do 42 tests, we should expect several of them to fail our jackknifes due to random chance. A histogram of the probability that we would get a larger S/N value just by random chance under the hypothesis that

$\alpha = 0$ is shown in Figure 7.5a. If our results are due to random chance, then every bin in this plot should be the same. There are slightly more measurements with a low probability to exceed (PTE). This does seem to indicate that there is some possiblity of systematics in the data. However, if we calculate the uncertainty in α from the likelihood function instead of calculating it using the statistical jackknife procedure, we get the PTE plot shown in Figure 7.5b. We don't see any excess of jackknife failures given the amount of tests that we do. The statistical jackknife procedure seems to underestimate some of the uncertainties leading to a smaller PTE.

7.4 Systematics Simulations

If we suspect that the detection of CB is due to systematics, it is prudent to run simulations involving these systematics to see if they could generate the level of CB that is seen in the data. As part of the analysis of the two year data, the BICEP team ran several simulations involving relative gain leakage and polarization orientation error [98]. Both of these systematics can generate non-zero TB and EB power spectra. The BICEP team ran several different simulations involving relative gain leakage [98]. In simulation 1, the relative gain leakage was randomly generated from a gaussian distribution with 1% rms. Simulation 2 was the same as the first, except with a 0.5% rms. In simulation 3, the relative gain errors were modeled after observed pair-sum/pair-diff correlation coefficients. Simulation 4 was the same as the third, except the two pixels with the highest relative gain errors were removed from the analysis. Simulation 5 scaled the correlations to the best estimate of the underlying distribution. The reason for doing this was because simulations with no systematic errors showed a large scatter in the correlation coefficients. For the polarization angle leakage simulations, a consistent 1°, 2°, or 3° offset was applied to each bolometer depending on the simulation. These will be simulations 6, 7, and 8, respectively. A summary of all the simulations is shown in Table 7.5. For each simulation, there were ≈ 20 realizations. We calculated the average power spectra and uncertainty on the average power spectra from the

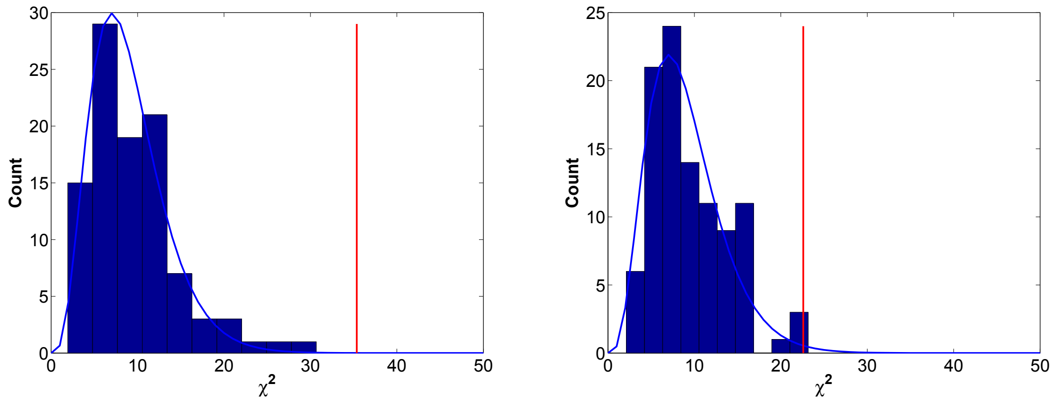

(a) Deck-angle, alt-cross TB

(b) Split-season, cross TB

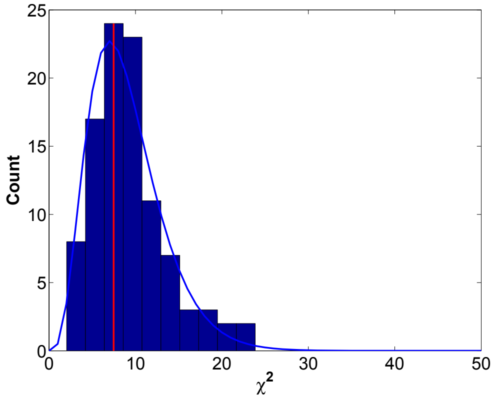

(c) Split-season, alt-cross TB

Figure 7.3: A histogram of χ^2 for the simulated BICEP jackknife data. The red line is the χ^2 for the real BICEP jackknife data. The blue curve is the theoretical χ^2 distribution function given the number of degrees of freedom.

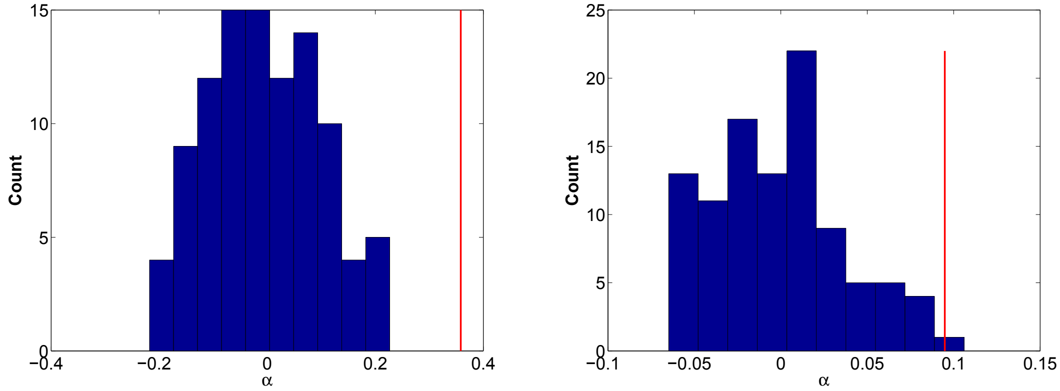

(a) Deck-angle, alt-cross TB

(b) Split-season, cross TB

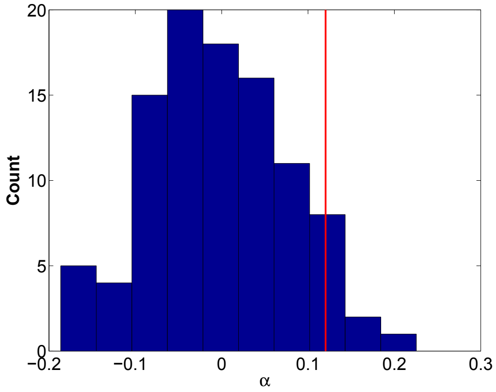

(c) Split-season, alt-cross TB

Figure 7.4: A histogram of the fitted α for the simulated BICEP jackknife data. The red line is the fitted α from the real BICEP jackknife data.

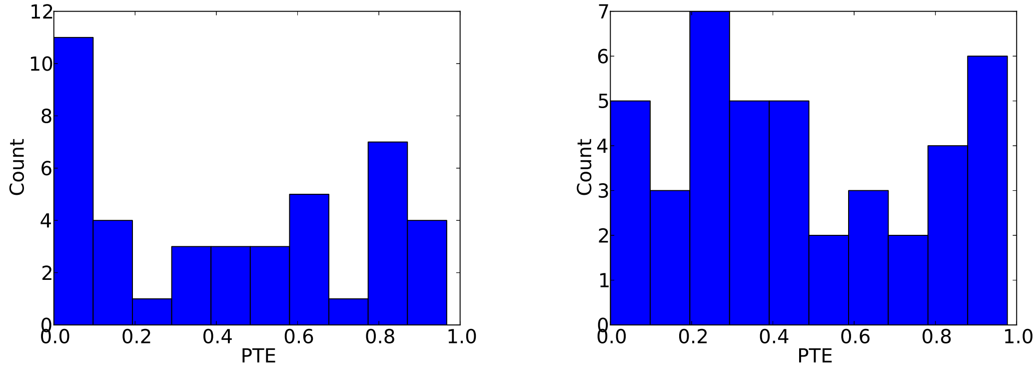

(a) Uncertainty from statistical jackknife (b) Uncertainty from likelihood function

Figure 7.5: A histogram of the PTEs for the measurement of α in each of the jackknife spectra. This is under the hypothesis that $\alpha = 0.0$.

different realizations. Using this average spectra, we fit for α using each of the simulations.

The results from the relative gain leakage simulations are shown in Table 7.6. A histogram of these results is shown in Figure 7.6a. At most, these simulations are able to generate $\alpha = 0.25°$, which is a small fraction of the $\alpha = 2.5°$ seen in the BICEP data. While relative gain leakage may cause some non-zero α, it is not the main contributor to the detection in the BICEP data.

The results from the polarization orientation error simulations are shown in Table 7.7. A histogram of these results is shown in Figure 7.6b. The alt-cross power spectra was not calculated in these simulations. The results from the 100, 150, and cross power spectra give α consistent with what is seen in the BICEP data. We also get the same amount of cosmological birefringence in both the TB and EB data. BICEP saw a change of $\approx 1°$ in the measured polarization orientations over a year [98] so there is a good chance this effect is biasing BICEP's CB α results.

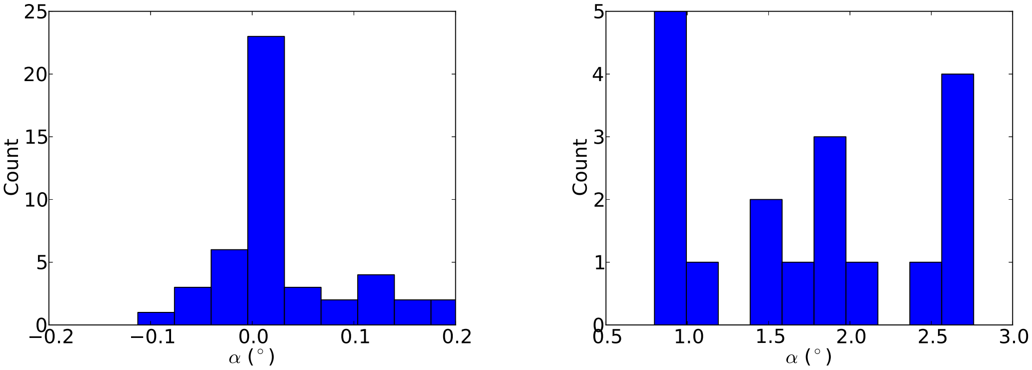

(a) Relative Gain Leakage Simulations (b) Polarization Orientation Error Simulations

Figure 7.6: A histogram of the fitted CB angles, α, for the different simulations

7.5 Conclusions

From analyzing the power spectra generated from the data at different frequencies there is good reason to believe that BICEP did not detect a non-zero α, but it was, in fact, due to systematic effects. The measured α was consistent with zero at 100 GHz but different depending on the frequencies used, which conflicts with the most common and simplest model of CB that the CB angle should be the same in all frequencies. The detection of a non-zero α mainly occurs when we take the B mode data from 150 GHz. The 100 GHz data is consistent with no CB.

The jackknife resampling technique did not help us as much as we had hoped. Several detections of non-zero α were not changed even after applying the first order jackknife correction to the fit. Unfortunately, we cannot just simply remove a single data point and get rid of the detection. If a systematic is affecting the BICEP measurements, then it is affecting more than one, and possibly all, of the bins.

The systematic that is most likely causing the detection of α is polarization angle rotation. This systematic mimics cosmological birefringence. A rotation of the polarization orienatation of a pixel is the exact same as a rotation in the opposite direction of the polarization of the incoming photons. The 1° differential rotation specified in [98] was determined through a measurement of the polarization angles at two different times during BICEP's measurements. They were found to be different by 1° over a timespan of a year, but it is possible the differential rotation was larger and is the cause of the detection of CB in BICEP's data. Even adding in a systematic uncertainty of 1° makes BICEP's measurement a non-detection.

Table 7.1: A table of the PTEs for all the different frequency combinations and different power spectra

frequency	TB	EB	TB+EB
100	0.32	0.36	0.28
150	0.03	0.22	0.03
cross	0.06	0.66	0.15
alt-cross	0.52	0.35	0.45
combined	0.02	0.17	0.03

Table 7.2: A table of the jackknife corrected fits for α.

frequency	TB	EB	TB+EB
100	$-3.31° \pm 2.63°$	$-0.53° \pm 2.33°$	$-1.98° \pm 1.74°$
150	$-4.95° \pm 1.57°$	$-3.07° \pm 1.12°$	$-3.73° \pm 0.92°$
cross	$-5.21° \pm 1.60°$	$-1.04° \pm 1.50°$	$-2.76° \pm 1.10°$
alt-cross	$-0.74° \pm 3.01°$	$-4.60° \pm 2.18°$	$-3.57° \pm 1.73°$
combined	$-4.98° \pm 1.31°$	$-2.39° \pm 0.93°$	$-3.23° \pm 0.76°$

Table 7.3: A table of the calculated bias in α from the jackknife resampling technique.

frequency	TB	EB	TB+EB
100	0.57°	−1.53°	−0.38°
150	−0.10°	−0.07°	−0.07°
cross	0.28°	0.31°	0.02°
alt-cross	−0.78°	−0.05°	−0.04°
combined	−0.19°	0.48°	−0.01°

Table 7.4: The results from fitting to the experimental jackknife spectra. The values for the jackknife spectra are described in Section 7.3.

Jackknife	Freq	Data	α	$J_1(\alpha)$	$J_2(\alpha)$	$\Delta\alpha$	S/N	$J_2(S/N)$
1	100	EB	0.81	1.66	1.65	3.04	0.27	0.54
1	100	TB	0.13	0.11	0.15	0.077	1.76	2.02
1	150	EB	0.36	0.70	0.82	0.83	0.44	0.99
1	150	TB	0.059	0.036	0.004	0.077	0.73	0.05
1	cross	EB	1.73	2.07	2.14	0.89	1.95	2.40
1	cross	TB	−0.052	−0.075	−0.045	0.11	0.48	0.42
1	alt-cross	EB	1.51	1.6	1.64	0.60	2.52	2.73
1	alt-cross	TB	0.36	0.38	0.35	0.064	5.57	5.49
2	100	EB	1.90	1.26	0.48	1.92	0.98	0.25
2	100	TB	−0.036	−0.048	−0.059	0.029	1.23	2.01
2	150	EB	0.10	−0.008	0.053	0.50	0.20	0.11
2	150	TB	0.002	0.011	−0.001	0.049	0.04	0.03
2	cross	EB	1.31	0.48	−0.28	1.54	0.85	0.18
2	cross	TB	0.010	0.016	−0.009	0.045	0.23	0.20
2	alt-cross	EB	0.31	0.67	0.82	1.24	0.25	0.66
2	alt-cross	TB	−0.065	−0.054	−0.074	0.075	0.87	0.98
3	100	EB	0.14	1.04	0.43	2.99	0.05	0.14
3	100	TB	0.066	0.038	0.080	0.089	0.73	0.89
3	150	EB	−0.080	−0.032	−0.052	0.45	0.18	0.12
3	150	TB	−0.019	−0.031	−0.032	0.059	0.33	0.48
3	cross	EB	0.034	−0.017	−0.38	0.46	0.07	0.83
3	cross	TB	0.095	0.13	0.15	0.038	2.52	3.92
3	alt-cross	EB	1.18	1.29	1.51	0.79	1.49	1.90
3	alt-cross	TB	0.12	0.12	0.10	0.034	3.59	3.02
4	100	EB	−0.17	−0.34	−0.92	0.66	0.25	1.38
4	100	TB	−0.054	−0.045	−0.031	0.034	1.59	0.90
4	150	EB	−0.086	0.17	0.20	0.98	0.09	0.21
4	150	TB	−0.023	−0.027	−0.070	0.052	0.43	1.35
4	cross	EB	−0.23	−0.39	−0.13	0.50	0.46	0.25
4	cross	TB	0.044	0.059	0.069	0.026	1.70	2.61
4	alt-cross	EB	−1.66	−2.04	−2.95	1.81	0.91	1.63
4	alt-cross	TB	0.095	0.089	0.10	0.063	1.51	1.59
5	100	EB	1.23	2.58	4.45	2.62	0.47	1.70
5	100	TB	0.066	0.078	0.080	0.034	1.96	2.37
5	150	EB	0.53	0.42	0.46	0.26	2.00	1.74
5	150	TB	−0.056	−0.047	−0.045	0.030	1.86	1.49
5	cross	EB	0.27	−0.43	−1.29	1.39	0.19	0.93
5	cross	TB	0.022	0.026	−0.026	0.039	0.57	0.66
5	alt-cross	EB	1.06	1.16	1.26	0.72	1.47	1.76
5	alt-cross	TB	−0.16	−0.18	−0.22	0.072	2.27	2.99
6		EB	−0.40	−0.36	−0.13	0.69	0.58	0.19
6		TB	−0.18	−0.099	−0.27	0.30	0.59	0.92

Table 7.5: A summary of different simulations run by the BICEP team and the purpose for each simulation.

Simulation	Purpose
1	randomly generated relative gain leakage with 1% rms
2	randomly generated relative gain leakage with 0.5% rms
3	relative gain errors modeled after observations
4	same as 3 except with two pixels removed
5	errors are scaled to the estimate of the underlying distribution
6	1° polarization angle offset
7	2° polarization angle offset
8	3° polarization angle offset

Table 7.6: The fitted α and uncertainty for the different relative gain leakage simulations described in the text.

Sim	Freq	Data	α	$\Delta\alpha$	S/N
1	100	EB	0.030	0.035	0.87
1	100	TB	0.008	0.064	0.12
1	150	EB	0.002	0.032	0.08
1	150	TB	0.0	0.052	0.0
1	cross	EB	-0.021	0.032	0.65
1	cross	TB	-0.048	0.057	0.84
1	alt-cross	EB	7.3×10^{-4}	0.001	0.72
1	alt-cross	TB	3.7×10^{-4}	0.002	0.22
2	100	EB	0.020	0.032	0.63
2	100	TB	0.015	0.053	0.27
2	150	EB	0.027	0.029	0.93
2	150	TB	0.016	0.047	0.34
2	cross	EB	0.005	0.029	0.18
2	cross	TB	-0.031	0.053	0.58
2	alt-cross	EB	2.7×10^{-4}	0.0009	0.29
2	alt-cross	TB	-4.1×10^{-4}	0.0014	0.29
3	100	EB	-0.008	0.027	0.28
3	100	TB	0.050	0.046	1.09
3	150	EB	0.030	0.031	0.98
3	150	TB	0.18	0.049	3.70
3	cross	EB	0.15	0.033	4.71
3	cross	TB	0.14	0.053	2.59
3	alt-cross	EB	-0.0015	0.001	1.5
3	alt-cross	TB	0.0040	0.0014	2.87
4	100	EB	-0.040	0.047	0.85
4	100	TB	-0.056	0.090	0.62
4	150	EB	0.11	0.056	1.98
4	150	TB	0.047	0.11	0.45
4	cross	EB	0.25	0.060	4.14
4	cross	TB	-0.026	0.10	0.25
4	alt-cross	EB	-0.0024	0.0017	1.47
4	alt-cross	TB	-0.0024	0.0026	0.90
5	100	EB	-0.041	0.046	0.89
5	100	TB	-0.11	0.088	1.27
5	150	EB	0.11	0.053	2.06
5	150	TB	0.091	0.088	1.03
5	cross	EB	0.23	0.056	4.13
5	cross	TB	0.077	0.087	0.89
5	alt-cross	EB	-0.0019	0.0016	1.17
5	alt-cross	TB	-0.0016	0.0024	0.66

Table 7.7: The fitted α and uncertainty for the different polarization angle leakage simulations

Sim	Freq	Data	α	$\Delta\alpha$	S/N
6	100	EB	1.02	0.048	21.30
6	100	TB	0.93	0.056	16.69
6	150	EB	0.79	0.041	19.17
6	150	TB	0.91	0.038	23.88
6	cross	EB	0.79	0.049	16.21
6	cross	TB	0.83	0.043	18.96
7	100	EB	1.91	0.057	33.48
7	100	TB	1.85	0.057	32.58
7	150	EB	1.46	0.045	31.90
7	150	TB	1.79	0.040	43.83
7	cross	EB	1.43	0.052	27.19
7	cross	TB	1.70	0.039	43.31
8	100	EB	2.74	0.064	42.73
8	100	TB	2.76	0.056	48.79
8	150	EB	2.39	0.060	39.39
8	150	TB	2.69	0.050	53.32
8	cross	EB	2.02	0.054	36.94
8	cross	TB	2.59	0.045	57.67

Bibliography

[1] W. Hu and M. White. A CMB polarization primer. New A, 2:323–344, October 1997.

[2] M. Shimon, B. Keating, N. Ponthieu, and E. Hivon. Cmb polarization systematics due to beam asymmetry: Impact on inflationary science. Phys. Rev. D, 77(8):083003–+, April 2008.

[3] D. P. Finkbeiner, M. Davis, and D. J. Schlegel. Extrapolation of Galactic Dust Emission at 100 Microns to Cosmic Microwave Background Radiation Frequencies Using FIRAS. ApJ, 524:867–886, October 1999.

[4] D. J. Fixsen and J. C. Mather. The Spectral Results of the Far-Infrared Absolute Spectrophotometer Instrument on COBE. ApJ, 581:817–822, December 2002.

[5] E. Komatsu, K. M. Smith, J. Dunkley, C. L. Bennett, B. Gold, G. Hinshaw, N. Jarosik, D. Larson, M. R. Nolta, L. Page, D. N. Spergel, M. Halpern, R. S. Hill, A. Kogut, M. Limon, S. S. Meyer, N. Odegard, G. S. Tucker, J. L. Weiland, E. Wollack, and E. L. Wright. Seven-year Wilkinson Microwave Anisotropy Probe (WMAP) Observations: Cosmological Interpretation. ApJS, 192:18–+, February 2011.

[6] R. Keisler, C. L. Reichardt, K. A. Aird, B. A. Benson, L. E. Bleem, J. E. Carlstrom, C. L. Chang, H. M. Cho, T. M. Crawford, A. T. Crites, T. de Haan, M. A. Dobbs, J. Dudley, E. M. George, N. W. Halverson, G. P. Holder, W. L. Holzapfel, S. Hoover, Z. Hou, J. D. Hrubes, M. Joy, L. Knox, A. T. Lee, E. M. Leitch, M. Lueker, D. Luong-Van, J. J. McMahon, J. Mehl, S. S. Meyer, M. Millea, J. J. Mohr, T. E. Montroy, T. Natoli, S. Padin, T. Plagge, C. Pryke, J. E. Ruhl, K. K. Schaffer, L. Shaw, E. Shirokoff, H. G. Spieler, Z. Staniszewski, A. A. Stark, K. Story, A. van Engelen, K. Vanderlinde, J. D. Vieira, R. Williamson, and O. Zahn. A Measurement of the Damping Tail of the Cosmic Microwave Background Power Spectrum with the South Pole Telescope. *ArXiv e-prints*, May 2011.

[7] S. Das, T. A. Marriage, P. A. R. Ade, P. Aguirre, M. Amiri, J. W. Appel, L. F. Barrientos, E. S. Battistelli, J. R. Bond, B. Brown, B. Burger, J. Chervenak, M. J. Devlin, S. R. Dicker, W. Bertrand Doriese, J. Dunkley, R. Dünner, T. Essinger-Hileman, R. P. Fisher, J. W. Fowler, A. Hajian, M. Halpern, M. Hasselfield, C. Hernández-Monteagudo, G. C. Hilton, M. Hilton, A. D. Hincks, R. Hlozek, K. M. Huffenberger, D. H. Hughes, J. P. Hughes, L. Infante, K. D. Irwin, J. Baptiste Juin, M. Kaul, J. Klein, A. Kosowsky, J. M. Lau, M. Limon, Y.-T. Lin, R. H. Lupton, D. Marsden, K. Martocci, P. Mauskopf, F. Menanteau, K. Moodley, H. Moseley, C. B. Netterfield, M. D. Niemack, M. R. Nolta, L. A. Page, L. Parker, B. Partridge, B. Reid, N. Sehgal, B. D. Sherwin, J. Sievers, D. N. Spergel, S. T. Staggs, D. S. Swetz, E. R. Switzer, R. Thornton, H. Trac, C. Tucker, R. Warne, E. Wollack, and Y. Zhao. The Atacama Cosmology Telescope: A Measurement of the Cosmic Microwave Background Power Spectrum at 148 and 218 GHz from the 2008 Southern Survey. ApJ, 729:62–+, March 2011.

[8] S. Dodelson. *Modern cosmology.* Modern cosmology / Scott Dodelson. Amsterdam (Netherlands): Academic Press. ISBN 0-12-219141-2, 2003, XIII + 440 p., 2003.

[9] W. Hu and S. Dodelson. Cosmic Microwave Background Anisotropies. ARA&A, 40:171–216, 2002.

[10] H. C. Chiang, P. A. R. Ade, D. Barkats, J. O. Battle, E. M. Bierman, J. J. Bock, C. D. Dowell, L. Duband, E. F. Hivon, W. L. Holzapfel, V. V. Hristov, W. C. Jones, B. G. Keating, J. M. Kovac, C. L. Kuo, A. E. Lange, E. M. Leitch, P. V. Mason, T. Matsumura, H. T. Nguyen, N. Ponthieu, C. Pryke, S. Richter, G. Rocha, C. Sheehy, Y. D. Takahashi, J. E. Tolan, and K. W. Yoon. Measurement of Cosmic Microwave Background Polarization Power Spectra from Two Years of BICEP Data. ApJ, 711:1123–1140, March 2010.

[11] M. L. Brown, P. Ade, J. Bock, M. Bowden, G. Cahill, P. G. Castro, S. Church, T. Culverhouse, R. B. Friedman, K. Ganga, W. K. Gear, S. Gupta, J. Hinderks, J. Kovac, A. E. Lange, E. Leitch, S. J. Melhuish, Y. Memari, J. A. Murphy, A. Orlando, C. O'Sullivan, L. Piccirillo, C. Pryke, N. Rajguru, B. Rusholme, R. Schwarz, A. N. Taylor, K. L. Thompson, A. H. Turner, E. Y. S. Wu, M. Zemcov, and The QUa D collaboration. Improved Measurements of the Temperature and Polarization of the Cosmic Microwave Background from QUaD. ApJ, 705:978–999, November 2009.

[12] QUIET Collaboration, C. Bischoff, A. Brizius, I. Buder, Y. Chinone, K. Cleary, R. N. Dumoulin, A. Kusaka, R. Monsalve, S. K. Næss, L. B. Newburgh, R. Reeves, K. M. Smith, I. K. Wehus, J. A. Zuntz, J. T. L. Zwart, L. Bronfman, R. Bustos, S. E. Church, C. Dickinson, H. K. Eriksen, P. G. Ferreira, T. Gaier, J. O. Gundersen, M. Hasegawa, M. Hazumi,

K. M. Huffenberger, M. E. Jones, P. Kangaslahti, D. J. Kapner, C. R. Lawrence, M. Limon, J. May, J. J. McMahon, A. D. Miller, H. Nguyen, G. W. Nixon, T. J. Pearson, L. Piccirillo, S. J. E. Radford, A. C. S. Readhead, J. L. Richards, D. Samtleben, M. Seiffert, M. C. Shepherd, S. T. Staggs, O. Tajima, K. L. Thompson, K. Vanderlinde, R. Williamson, and B. Winstein. First Season QUIET Observations: Measurements of CMB Polarization Power Spectra at 43 GHz in the Multipole Range 25 $\leq$ ell $\leq$ 475. *ArXiv e-prints*, December 2010.

[13] A. Lewis and A. Challinor. Weak gravitational lensing of the CMB. Phys. Rep., 429:1–65, June 2006.

[14] W. Hu and T. Okamoto. Mass reconstruction with cosmic microwave background polarization. ApJ, 574:566–574, August 2002.

[15] T. Okamoto and W. Hu. Cosmic microwave background lensing reconstruction on the full sky. Phys. Rev. D, 67(8):083002–+, April 2003.

[16] S. M. Carroll, G. B. Field, and R. Jackiw. Limits on a Lorentz- and parity-violating modification of electrodynamics. Phys. Rev. D, 41:1231–1240, February 1990.

[17] C. L. Reichardt, P. A. R. Ade, J. J. Bock, J. R. Bond, J. A. Brevik, C. R. Contaldi, M. D. Daub, J. T. Dempsey, J. H. Goldstein, W. L. Holzapfel, C. L. Kuo, A. E. Lange, M. Lueker, M. Newcomb, J. B. Peterson, J. Ruhl, M. C. Runyan, and Z. Staniszewski. High-Resolution CMB Power Spectrum from the Complete ACBAR Data Set. ApJ, 694:1200–1219, April 2009.

[18] M. Zaldarriaga and U. Seljak. All-sky analysis of polarization in the microwave background. Phys. Rev. D, 55:1830–1840, February 1997.

[19] M. Kamionkowski, A. Kosowsky, and A. Stebbins. A Probe of Primordial Gravity Waves and Vorticity. *Physical Review Letters*, 78:2058–2061, March 1997.

[20] W. Hu, M. M. Hedman, and M. Zaldarriaga. Benchmark parameters for CMB polarization experiments. Phys. Rev. D, 67(4):043004–+, February 2003.

[21] C. Rosset, V. B. Yurchenko, J. Delabrouille, J. Kaplan, Y. Giraud-Héraud, J.-M. Lamarre, and J. A. Murphy. Beam mismatch effects in cosmic microwave background polarization measurements. A&A, 464:405–415, March 2007.

[22] D. O'Dea, A. Challinor, and B. R. Johnson. Systematic errors in cosmic microwave background polarization measurements. MNRAS,, 376,:1767,, apr 2007.

[23] M. Kamionkowski. How to Derotate the Cosmic Microwave Background Polarization. *Physical Review Letters*, 102(11):111302–+, March 2009.

[24] M. Su, A. P. S. Yadav, and M. Zaldarriaga. Impact of instrumental systematic contamination on the lensing mass reconstruction using the CMB polarization. Phys. Rev. D, 79(12):123002–+, June 2009.

[25] A. Lewis, A. Challinor, and A. Lasenby. Efficient Computation of Cosmic Microwave Background Anisotropies in Closed Friedmann-Robertson-Walker Models. ApJ, 538:473–476, August 2000.

[26] Antony Lewis and Sarah Bridle. Cosmological parameters from CMB and other data: a Monte- Carlo approach. Phys. Rev. D, 66:103511, 2002.

[27] M. Kaplinghat, L. Knox, and Y.-S. Song. Determining Neutrino Mass from the Cosmic Microwave Background Alone. *Physical Review Letters*, 91(24):241301–+, December 2003.

[28] J. Lesgourgues, L. Perotto, S. Pastor, and M. Piat. Probing neutrino masses with CMB lensing extraction. Phys. Rev. D, 73(4):045021–+, February 2006.

[29] L. Perotto, J. Lesgourgues, S. Hannestad, H. Tu, and Y. Y Y Wong. Probing cosmological parameters with the CMB: forecasts from Monte Carlo simulations. J. Cosmology Astropart. Phys., 10:13–+, October 2006.

[30] B. G. Keating. An "Ultrasonic Image" of the Embryonic Universe: CMB Polarization Tests of the Inflationary Paradigm. *ArXiv e-prints*, June 2008.

[31] S. Hanany, J. Hubmayr, B. R. Johnson, T. Matsumura, P. Oxley, and M. Thibodeau. Millimeter-wave achromatic half-wave plate. Appl. Opt., 44:4666–4670, August 2005.

[32] B. R. Johnson, J. Collins, M. E. Abroe, P. A. R. Ade, J. Bock, J. Borrill, A. Boscaleri, P. de Bernardis, S. Hanany, A. H. Jaffe, T. Jones, A. T. Lee, L. Levinson, T. Matsumura, B. Rabii, T. Renbarger, P. L. Richards, G. F. Smoot, R. Stompor, H. T. Tran, C. D. Winant, J. H. P. Wu, and J. Zuntz. MAXIPOL: Cosmic Microwave Background Polarimetry Using a Rotating Half-Wave Plate. ApJ, 665:42–54, August 2007.

[33] C. J. MacTavish, P. A. R. Ade, E. S. Battistelli, S. Benton, R. Bihary, J. J. Bock, J. R. Bond, J. Brevik, S. Bryan, C. R. Contaldi, B. P. Crill, O. Doré, L. Fissel, S. R. Golwala, M. Halpern, G. Hilton, W. Holmes, V. V. Hristov, K. Irwin, W. C. Jones, C. L. Kuo, A. E. Lange, C. Lawrie, T. G. Martin, P. Mason, T. E. Montroy, C. B. Netterfield, D. Riley, J. E. Ruhl, M. Runyan, A. Trangsrud, C. Tucker, A. Turner, M. Viero, and D. Wiebe. Spider Optimization: Probing the Systematics of a Large-Scale B-Mode Experiment. ApJ, 689:655–665, December 2008.

[34] M. Zaldarriaga and U. Seljak. Gravitational lensing effect on cosmic microwave background polarization. Phys. Rev. D, 58(2):023003–+, July 1998.

[35] S. M. Carroll. Quintessence and the Rest of the World: Suppressing Long-Range Interactions. *Physical Review Letters*, 81:3067–3070, October 1998.

[36] G.-C. Liu, S. Lee, and K.-W. Ng. Effect on Cosmic Microwave Background Polarization of Coupling of Quintessence to Pseudoscalar Formed from the Electromagnetic Field and its Dual. *Physical Review Letters*, 97(16):161303–+, October 2006.

[37] J.-Q. Xia, H. Li, X. Wang, and X. Zhang. Testing CPT symmetry with CMB measurements. A&A, 483:715–718, June 2008.

[38] E. Komatsu, J. Dunkley, M. R. Nolta, C. L. Bennett, B. Gold, G. Hinshaw, N. Jarosik, D. Larson, M. Limon, L. Page, D. N. Spergel, M. Halpern, R. S. Hill, A. Kogut, S. S. Meyer, G. S. Tucker, J. L. Weiland, E. Wollack, and E. L. Wright. Five-Year Wilkinson Microwave Anisotropy Probe (WMAP) Observations: Cosmological Interpretation. *arXiv:0803.0547 [astro-ph]*, 803,

[39] A. Kosowsky and A. Loeb. Faraday Rotation of Microwave Background Polarization by a Primordial Magnetic Field. ApJ, 469:1–+, September 1996.

[40] D. N. Spergel, R. Bean, O. Doré, M. R. Nolta, C. L. Bennett, J. Dunkley, G. Hinshaw, N. Jarosik, E. Komatsu, L. Page, H. V. Peiris, L. Verde, M. Halpern, R. S. Hill, A. Kogut, M. Limon, S. S. Meyer, N. Odegard, G. S. Tucker, J. L. Weiland, E. Wollack, and E. L. Wright. Three-Year Wilkinson Microwave Anisotropy Probe (WMAP) Observations: Implications for Cosmology. ApJS, 170:377–408, June 2007.

[41] N. J. Miller, M. Shimon, and B. G. Keating. CMB beam systematics: Impact on lensing parameter estimation. Phys. Rev. D, 79(6):063008–+, March 2009.

[42] K. M. Smith, A. Cooray, S. Das, O. Doré, D. Hanson, C. Hirata, M. Kaplinghat, B. Keating, M. LoVerde, N. Miller, G. Rocha, M. Shimon, and O. Zahn. CMBPol Mission Concept Study: Gravitational Lensing. *ArXiv e-prints*, November 2008.

[43] S. M. Carroll and G. B. Field. Is There Evidence for Cosmic Anisotropy in the Polarization of Distant Radio Sources? *Physical Review Letters*, 79:2394–2397, September 1997.

[44] A. Lue, L. Wang, and M. Kamionkowski. Cosmological Signature of New Parity-Violating Interactions. *Physical Review Letters*, 83:1506–1509, August 1999.

[45] S. Alexander and J. Martin. Birefringent gravitational waves and the consistency check of inflation. Phys. Rev. D, 71(6):063526–+, March 2005.

[46] S. H. Alexander, M. E. Peskin, and M. M. Sheikh-Jabbari. Leptogenesis from Gravity Waves in Models of Inflation. *Physical Review Letters*, 96(8):081301–+, February 2006.

[47] B. Feng, M. Li, J.-Q. Xia, X. Chen, and X. Zhang. Searching for CPT Violation with Cosmic Microwave Background Data from WMAP and BOOMERANG. *Physical Review Letters*, 96(22):221302–+, June 2006.

[48] P. Cabella, P. Natoli, and J. Silk. Constraints on CPT violation from Wilkinson Microwave Anisotropy Probe three year polarization data: A wavelet analysis. Phys. Rev. D, 76(12):123014–+, December 2007.

[49] E. Y. S. Wu, P. Ade, J. Bock, M. Bowden, M. L. Brown, G. Cahill, P. G. Castro, S. Church, T. Culverhouse, R. B. Friedman, K. Ganga, W. K. Gear, S. Gupta, J. Hinderks, J. Kovac, A. E. Lange, E. Leitch, S. J. Melhuish, Y. Memari, J. A. Murphy, A. Orlando, L. Piccirillo, C. Pryke, N. Rajguru, B. Rusholme, R. Schwarz, C. O'Sullivan, A. N. Taylor, K. L. Thompson, A. H. Turner, and M. Zemcov. Parity Violation Constraints Using Cosmic Microwave Background Polarization Spectra from 2006 and 2007 Observations by the QUaD Polarimeter. *Physical Review Letters*, 102(16):161302–+, April 2009.

[50] M. M. Basko and A. G. Polnarev. Polarization and anisotropy of the RELICT radiation in an anisotropic universe. MNRAS, 191:207–215, April 1980.

[51] A. G. Polnarev. Polarization and Anisotropy Induced in the Microwave Background by Cosmological Gravitational Waves. *SvA*, 29:607–+, December 1985.

[52] R. Crittenden, R. L. Davis, and P. J. Steinhardt. Polarization of the Microwave Background Due to Primordial Gravitational Waves. ApJ, 417:L13+, November 1993.

[53] R. A. Frewin, A. G. Polnarev, and P. Coles. Gravitational Waves and the Polarization of the Cosmic Microwave Background. MNRAS, 266:L21+, January 1994.

[54] P. Coles, R. A. Frewin, and A. G. Polnarev. CMBR Polarization from Gravitational Waves. In F. Occhionero, editor, *Birth of the Universe and Fundamental Physics*, volume 455 of *Lecture Notes in Physics, Berlin Springer Verlag*, pages 273–+, 1995.

[55] U. Seljak. Measuring Polarization in the Cosmic Microwave Background. ApJ, 482:6–+, June 1997.

[56] U. Seljak and M. Zaldarriaga. Signature of Gravity Waves in the Polarization of the Microwave Background. *Physical Review Letters*, 78:2054–2057, March 1997.

[57] M. Kamionkowski and A. Kosowsky. Detectability of inflationary gravitational waves with microwave background polarization. Phys. Rev. D, 57:685–691, January 1998.

[58] D. Baskaran, L. P. Grishchuk, and A. G. Polnarev. Imprints of relic gravitational waves in cosmic microwave background radiation. Phys. Rev. D, 74(8):083008–+, October 2006.

[59] B. G. Keating, A. G. Polnarev, N. J. Miller, and D. Baskaran. The Polarization of the Cosmic Microwave Background due to Primordial Gravitational Waves. *International Journal of Modern Physics A*, 21:2459–2479, 2006.

[60] A. C. Taylor, A. Challinor, D. Goldie, K. Grainge, M. E. Jones, A. N. Lasenby, S. Withington, G. Yassin, W. K. Gear, L. Piccirillo, P. Ade, P. D. Mauskopf, B. Maffei, and G. Pisano. CLOVER - A new instrument for measuring the B-mode polarization of the CMB. *arXiv:astro-ph/0407148*, July 2004.

[61] M. Bowden et al. Scientific optimization of a ground-based cmb polarization experiment. MNRAS, 349:321–335, March 2004.

[62] K. W. Yoon et al. The Robinson Gravitational Wave Background Telescope (BICEP): a bolometric large angular scale CMB polarimeter. In *Millimeter and Submillimeter Detectors and Instrumentation for Astronomy III. Edited by Zmuidzinas, Jonas; Holland, Wayne S.; Withington, Stafford; Duncan, William D.. Proceedings of the SPIE, Volume 6275, pp. 62751K (2006).*, volume 6275 of *Presented at the Society of Photo-Optical Instrumentation Engineers (SPIE) Conference*, July 2006.

[63] D. N. Spergel and M. Zaldarriaga. Cosmic Microwave Background Polarization as a Direct Test of Inflation. *Phys. Rev. Letters*, 79:2180–2183, September 1997.

[64] H. V. Peiris, E. Komatsu, L. Verde, D. N. Spergel, C. L. Bennett, M. Halpern, G. Hinshaw, N. Jarosik, A. Kogut, M. Limon, S. S. Meyer, L. Page, G. S. Tucker, E. Wollack, and E. L. Wright. First-Year Wilkinson Microwave Anisotropy Probe (WMAP) Observations: Implications For Inflation. Astrophysical Journal Supplement Series, 148:213–231, September 2003.

[65] R. G. Crittenden, D. Coulson, and N. G. Turok. Temperature-polarization correlations from tensor fluctuations. Phys. Rev. D, 52:5402–+, November 1995.

[66] L. P. Grishchuk. Discovering Relic Gravitational Waves in Cosmic Microwave Background Radiation. *arXiv:0707.3319 [astro-ph]*, 707, July 2007.

[67] D. N. Spergel, R. Bean, O. Doré, M. R. Nolta, C. L. Bennett, J. Dunkley, G. Hinshaw, N. Jarosik, E. Komatsu, L. Page, H. V. Peiris, L. Verde, M. Halpern, R. S. Hill, A. Kogut, M. Limon, S. S. Meyer, N. Odegard, G. S. Tucker, J. L. Weiland, E. Wollack, and E. L. Wright. Three-Year Wilkinson Microwave Anisotropy Probe (WMAP) Observations: Implications for Cosmology. ApJS, 170:377–408, June 2007.

[68] Meir Shimon, Brian Keating, Nicolas Ponthieu, and Eric Hivon. Cmb polarization systematics due to beam asymmetry: Impact on inflationary science. *arXiv:0709.1513 [astro-ph]*, 2007.

[69] A. Challinor and G. Chon. Error analysis of quadratic power spectrum estimates for cosmic microwave background polarization: sampling covariance. MNRAS, 360:509–532, June 2005.

[70] T. L. Smith, M. Kamionkowski, and A. Cooray. Direct detection of the inflationary gravitational-wave background. Phys. Rev. D, 73(2):023504–+, January 2006.

[71] A. Lewis, A. Challinor, and A. Lasenby. Efficient Computation of Cosmic Microwave Background Anisotropies in Closed Friedmann-Robertson-Walker Models. ApJ, 538:473–476, August 2000.

[72] M. Viel, J. Weller, and M. G. Haehnelt. Constraints on the primordial power spectrum from high-resolution Lyman α forest spectra and WMAP. MNRAS, 355:L23–L28, December 2004.

[73] M. Kaplinghat. Applications of high resolution high sensitivity observations of the cmb. *New Astronomy Review*, 47:893–900, December 2003.

[74] M. Tegmark and G. Efstathiou. A method for subtracting foregrounds from multifrequency CMB sky maps**. MNRAS, 281:1297–1314, August 1996.

[75] F. R. Bouchet, S. Prunet, and S. K. Sethi. Multifrequency Wiener filtering of cosmic microwave background data with polarization. MNRAS, 302:663–676, February 1999.

[76] S. V. Vaseghi. *Advanced Digital Signal Processing and Noise Reduction*. John Wiley & Sons, 2006.

[77] F. Wilcoxon. Individual comparisons by ranking methods. *Biometrics Bulletin*, 1(6):80–83, 1945.

[78] E. L. Lehmann. *Nonparametric Statistical Methods Based on Ranks.* McGraw-Hill, 1975.

[79] J. Dunkley, E. Komatsu, M. R. Nolta, D. N. Spergel, D. Larson, G. Hinshaw, L. Page, C. L. Bennett, B. Gold, N. Jarosik, J. L. Weiland, M. Halpern, R. S. Hill, A. Kogut, M. Limon, S. S. Meyer, G. S. Tucker, E. Wollack, and E. L. Wright. Five-Year Wilkinson Microwave Anisotropy Probe (WMAP) Observations: Likelihoods and Parameters from the WMAP data. *arXiv:0803.0586 [astro-ph]*, 803, March 2008.

[80] M. Kamionkowski and A. Kosowsky. Detectability of inflationary gravitational waves with microwave background polarization. Phys. Rev. D, 57:685–691, January 1998.

[81] QUaD collaboration: C. Pryke, P. Ade, J. Bock, M. Bowden, M. L. Brown, G. Cahill, P. G. Castro, S. Church, T. Culverhouse, R. Friedman, K. Ganga, W. K. Gear, S. Gupta, J. Hinderks, J. Kovac, A. E. Lange, E. Leitch, S. J. Melhuish, Y. Memari, J. A. Murphy, A. Orlando, R. Schwarz, C. O'Sullivan, L. Piccirillo, N. Rajguru, B. Rusholme, A. N. Taylor, K. L. Thompson, A. H. Turner, E. Y. S. Wu, and M. Zemcov. Second and third season QUaD CMB temperature and polarization power spectra. *arXiv:0805.1944 [astro-ph]*, 805, May 2008.

[82] S. Galli, M. Martinelli, A. Melchiorri, L. Pagano, B. D. Sherwin, and D. N. Spergel. Constraining fundamental physics with future CMB experiments. Phys. Rev. D, 82(12):123504–+, December 2010.

[83] C. Giunti and C.W. Kim. *Fundamentals of Neutrino Physics and Astrophysics.* Oxford University Press, USA, 2007.

[84] G. M. Fuller and C. T. Kishimoto. Quantum Coherence of Relic Neutrinos. *Physical Review Letters*, 102(20):201303–+, May 2009.

[85] S. H. Hansen, G. Mangano, A. Melchiorri, G. Miele, and O. Pisanti. Constraining neutrino physics with big bang nucleosynthesis and cosmic microwave background radiation. Phys. Rev. D, 65(2):023511–+, January 2002.

[86] J. P. Kneller, R. J. Scherrer, G. Steigman, and T. P. Walker. How does the cosmic microwave background plus big bang nucleosynthesis constrain new physics? Phys. Rev. D, 64(12):123506–+, December 2001.

[87] V. Barger, J. P. Kneller, P. Langacker, D. Marfatia, and G. Steigman. Hiding relativistic degrees of freedom in the early universe. *Physics Letters B*, 569:123–128, September 2003.

[88] K. Abazajian, N. F. Bell, G. M. Fuller, and Y. Y. Y. Wong. Cosmological lepton asymmetry, primordial nucleosynthesis and sterile neutrinos. Phys. Rev. D, 72(6):063004–+, September 2005.

[89] J. Lesgourgues and S. Pastor. Cosmological implications of a relic neutrino asymmetry. Phys. Rev. D, 60(10):103521–+, November 1999.

[90] J. Hamann, J. Lesgourgues, and G. Mangano. Using big bang nucleosynthesis in cosmological parameter extraction from the cosmic microwave background: a forecast for PLANCK. J. Cosmology Astropart. Phys., 3:4–+, March 2008.

[91] L. A. Popa and A. Vasile. WMAP five-year constraints on lepton asymmetry and radiation energy density: implications for Planck. J. Cosmology Astropart. Phys., 6:28–+, June 2008.

[92] The Polarbear Collaboration, J. Errard, P. A. R. Ade, A. Anthony, K. Arnold, F. Aubin, D. Boettger, J. Borrill, C. Cantalupo, M. A. Dobbs, D. Flanigan, A. Ghribi, N. Halverson, M. Hazumi, W. L. Holzapfel, J. Howard, P. Hyland, A. Jaffe, B. Keating, T. Kisner, Z. Kermish, A. T. Lee, E. Linder, M. Lungu, T. Matsumura, N. Miller, X. Meng, M. Myers, H. Nishino, R. O'Brient, D. O'Dea, C. Reichardt, I. Schanning, A. Shimizu, C. Shimmin, M. Shimon, H. Spieler, B. Steinbach, R. Stompor, A. Suzuki, T. Tomaru, H. T. Tran, C. Tucker, E. Quealy, P. L. Richards, and O. Zahn. The new generation CMB B-mode polarization experiment: POLARBEAR. *ArXiv e-prints*, November 2010.

[93] B. Keating, S. Moyerman, D. Boettger, J. Edwards, G. Fuller, F. Matsuda, N. Miller, H. Paar, G. Rebeiz, I. Schanning, M. Shimon, N. Stebor, K. Arnold, D. Flanigan, W. Holzapfel, J. Howard, Z. Kermish, A. Lee, M. Lungu, M. Myers, H. Nishino, R. O'Brient, E. Quealy, C. Reichardt, P. Richards, C. Shimmin, B. Steinbach, A. Suzuki, O. Zahn, J. Borrill, C. Cantalupo, E. Kisner, E. Linder, M. Sholl, H. Spieler, A. Anthony, N. Halverson, J. Errard, G. Fabbian, M. Le Jeune, R. Stompor, A. Jaffe, D. O'Dea, Y. Chinone, M. Hasegawa, M. Hazumi, T. Matsumura, H. Morii, A. Shimizu, T. Tomaru, P. Hyland, M. Dobbs, P. Ade, W. Grainger, and C. Tucker. Ultra High Energy Cosmology with POLARBEAR. *ArXiv e-prints*, October 2011.

[94] The Planck Collaboration. The Scientific Programme of Planck. *ArXiv Astrophysics e-prints*, April 2006.

[95] J. Bock, A. Cooray, S. Hanany, B. Keating, A. Lee, T. Matsumura, M. Milligan, N. Ponthieu, T. Renbarger, and H. Tran. The Experimental Probe of Inflationary Cosmology (EPIC): A Mission Concept Study for NASA's Einstein Inflation Probe. *ArXiv e-prints*, May 2008.

[96] J. Bock, A. Aljabri, A. Amblard, D. Baumann, M. Betoule, T. Chui, L. Colombo, A. Cooray, D. Crumb, P. Day, C. Dickinson, D. Dowell, M. Dragovan, S. Golwala, K. Gorski, S. Hanany, W. Holmes, K. Irwin, B. Johnson, B. Keating, C.-L. Kuo, A. Lee, A. Lange, C. Lawrence, S. Meyer, N. Miller, H. Nguyen, E. Pierpaoli, N. Ponthieu, J.-L. Puget, J. Raab, P. Richards, C. Satter, M. Seiffert, M. Shimon, H. Tran, B. Williams, and J. Zmuidzinas. Study of the Experimental Probe of Inflationary Cosmology (EPIC)-Intemediate Mission for NASA's Einstein Inflation Probe. *ArXiv e-prints*, June 2009.

[97] K. M. Huffenberger, B. P. Crill, A. E. Lange, K. M. Górski, and C. R. Lawrence. Measuring Planck beams with planets. A&A, 510:A58+, February 2010.

[98] Y. D. Takahashi, P. A. R. Ade, D. Barkats, J. O. Battle, E. M. Bierman, J. J. Bock, H. C. Chiang, C. D. Dowell, L. Duband, E. F. Hivon, W. L. Holzapfel, V. V. Hristov, W. C. Jones, B. G. Keating, J. M. Kovac, C. L. Kuo, A. E. Lange, E. M. Leitch, P. V. Mason, T. Matsumura, H. T. Nguyen, N. Ponthieu, C. Pryke, S. Richter, G. Rocha, and K. W. Yoon. Characterization of the BICEP Telescope for High-precision Cosmic Microwave Background Polarimetry. ApJ, 711:1141–1156, March 2010.

[99] J.-Q. Xia, H. Li, and X. Zhang. Probing CPT violation with CMB polarization measurements. *Physics Letters B*, 687:129–132, April 2010.

[100] M. H. Quenouille. Notes on bias in estimation. *Biometrika*, 43:353–360, 1956.

[101] J. W. Tukey. Bias and confidence in not quite large samples. *Annals of Mathematical Statistics*, 29:614, 1958.

[102] Rupert G. Miller. The jackknife-a review. *Biometrika*, 61(1):1–15, 1974.

[103] B. Efron. *The Jackknife, the Bootstrap and other resampling plans.* Society for Industrial Mathematics, 1982.

[104] J. Shao and D. Tu. *The Jackknife and Bootstrap.* Springer, 1995.